Fall 2012

Passive and muscle-based predictive computer models of seated and supine humans in whole-body vibration

Yang Wang
University of Iowa

PASSIVE AND MUSCLE-BASED PREDICTIVE COMPUTER MODELS OF SEATED AND SUPINE HUMANS IN WHOLE-BODY VIBRATION

by

Yang Wang

An Abstract

Of a thesis submitted in partial fulfillment
of the requirements for the Doctor of
Philosophy degree in Civil and
Environmental Engineering
in the Graduate College of
The University of Iowa

December 2012

Thesis Supervisor: Associate Professor Salam Rahmatalla

ABSTRACT

Studies in human response to whole-body vibration, such those encountered in heavy machinery and ground and aerial transportation, have highlighted the critical role of the head-neck posture of seated human occupants and the role of the transport system of a supine human on the severity of the transmitted vibration to the human body.

Novel passive and muscle-based models are introduced in this work to predict the biodynamical response of the human under whole-body vibration in seated and supine postures.

Planar and three-dimensional models representing the human head-neck system under different seated postures and fore-aft and multiple-axis whole-body vibration are first introduced. In these models, the head-neck system is represented by rigid links connected via spring-damper components representing the soft-tissue and connecting elements between the bones. Additional muscle components are added to some models. The muscle components comprise additional mass, spring, and damper elements arranged in a special order to capture the effect of changes in the displacement, velocity, acceleration, and jerk. The results show that the proposed models are able to predict the displacement and acceleration of the head under different vibration files, with the muscle-based models showing better performance than the passive models.

The second set of models is introduced in this work to investigate the effect of the underlying transport system conditions on the response of supine humans under vertical and multiple-axis whole-body vibration. In these models, the supine-human body is represented by three rigid links representing the head, torso/arms, and legs. The links are connected via rotational and translational joints, and therefore, it is expected that the models can capture the coupling effects between adjacent segments. The joints comprise translational and rotational spring-damper components that represent the soft tissue and the connecting elements between the segments. The contact surfaces between the supine

human and the underlying transport system were modeled using spring-damper elements. Two underlying transport systems were considered, including a rigid support and a long spinal board attached to a military litter. The results showed that the proposed models were able to predict the effect of the transport systems on the human response under different vibration conditions.

Abstract Approved: _____
Thesis Supervisor

_____
Title and Department

_____
Date

PASSIVE AND MUSCLE-BASED PREDICTIVE COMPUTER MODELS OF SEATED AND SUPINE HUMANS IN WHOLE-BODY VIBRATION

by

Yang Wang

A thesis submitted in partial fulfillment
of the requirements for the Doctor of
Philosophy degree in Civil and
Environmental Engineering
in the Graduate College of
The University of Iowa

December 2012

Thesis Supervisor: Associate Professor Salam Rahmatalla

Graduate College
The University of Iowa
Iowa City, Iowa

CERTIFICATE OF APPROVAL

_____

PH.D. THESIS

_____

This is to certify that the Ph.D. thesis of

Yang Wang

has been approved by the Examining Committee
for the thesis requirement for the Doctor of Philosophy
degree in Civil and Environmental Engineering at the
December 2012 graduation.

Thesis Committee: _____
Salam Rahmatalla, Thesis Supervisor

_____
Jia Lu

_____
Jasbir Arora

_____
Asghar Bhatti

_____
David Wilder

ACKNOWLEDGMENTS

I would like to thank all those who helped me during my Ph.D. study at The University of Iowa. First of all, I would love to express my deepest gratitude to my advisor, Dr. Rahmatalla, who inspired, encouraged, and supported me financially and academically.

I also thank the members of my graduate committee—Dr. Jasbir Arora, Dr. Asghar Bhatti, Dr. David Wilder, and Dr. Jia Lu—for their guidance, encouragement, and suggestions.

I want to express my gratitude to people at the Center for Computer-Aided Design (CCAD), especially Jonathan DeShaw, John Meusch, and Liu Ye. Without them, I could not have run the experiments and built my database.

Additionally, I acknowledge my parents, Benshu Yang and Aiguo Wang. They encourage me whenever I have troubles in my studies or life and give me valuable advice.

Finally, I would like to give my thanks to my husband, Scott Woods. He understands what I want to do and supports me in my life.

ABSTRACT

Studies of human response to whole-body vibration, such those encountered in heavy machinery and ground and aerial transportation, have highlighted the critical role of the head-neck posture of seated human occupants and the role of the transport system of a supine human on the severity of the transmitted vibration to the human body.

Novel passive and muscle-based models are introduced in this work to predict the biodynamical response of the human under whole-body vibration in seated and supine postures.

Planar and three-dimensional models representing the human head-neck system under different seated postures and fore-aft and multiple-axis whole-body vibration are first introduced. In these models, the head-neck system is represented by rigid links connected via spring-damper components representing the soft-tissue and connecting elements between the bones. Additional muscle components are added to some models. The muscle components comprise additional mass, spring, and damper elements arranged in a special order to capture the effect of changes in the displacement, velocity, acceleration, and jerk. The results show that the proposed models are able to predict the displacement and acceleration of the head under different vibration files, with the muscle-based models showing better performance than the passive models.

The second set of models is introduced in this work to investigate the effect of the underlying transport system conditions on the response of supine humans under vertical and multiple-axis whole-body vibration. In these models, the supine human body is represented by three rigid links representing the head, torso/arms, and legs. The links are connected via rotational and translational joints, and therefore, it is expected that the models can capture the coupling effects between adjacent segments. The joints comprise translational and rotational spring-damper components that represent the soft tissue and the connecting elements between the segments. The contact surfaces between the supine

human and the underlying transport system were modeled using spring-damper elements. Two underlying transport systems were considered, including a rigid support and a long spinal board attached to a military litter. The results showed that the proposed models were able to predict the effect of the transport systems on the human response under different vibration conditions.

TABLE OF CONTENTS

LIST OF TABLES

LIST OF FIGURES

LIST OF ABBREVIATIONS

2 D	Two-dimensional
3 D	Three-dimensional
ATV	All-terrain vehicle
CSD	Cross-spectral density
DH	Denavit-Hartenberg method
DOF	Degree of freedom
DUT	Device under test
FFT	Fast Fourier Transport
HNS	Head-neck system
IRB	Institutional review board
MIMO	Multi-input and multi-output system
RMS	Root mean square
PSD	Power spectal density
SISO	Single-input and single-output system
STRN	Sternum
WBV	Whole-body vibration

CHAPTER I

INTRODUCTION

1.1 Motivation

Transmitted vibrations to the human body from the surrounding environments, such as those encountered in heavy machinery or ground and aerial transportation, can cause considerable discomfort, reduction in safety and performance, and possibly long-term injuries. Studies in whole-body vibration (WBV) have shown that human posture, muscle activity, and the way the human interacts with the surrounding equipment play a major role in how much and the manner in which vibration is transmitted to and through the human body.

Experiments have provided considerable information and insight on human response to vibration; however, experiments are costly and limited. Predictive computational human models, on the other hand, have proven to be very effective tools in investigating human biomechanics under vibration and in assisting safety planning and design modification. Yet, the current status of knowledge is lacking biomechanical models that can predict the effect of the head-neck posture of seated occupants and models that can predict the effect of the transport condition of supine occupants under WBV.

The goal of this work is to develop human biodynamic models that can predict human response under WBV, specifically those considering head-neck postures of seated occupants and those considering supine humans under different transport conditions. Another goal of this thesis is to introduce a new muscle model that can be integrated with the current human models to produce more realistic responses.

This thesis is organized in six chapters and appendixes. Following a brief introduction in Chapter One, planar human head-neck models for seated positions under fore-aft WBV are introduced in Chapter Two with emphasis on postures. In Chapter

Two, one- and two-degree-of-freedom (DOF) passive and muscle-based models are introduced, and their results are discussed and compared with data from experiments. Three-dimensional (3D) head-neck models are presented in Chapter Three, including passive and muscle-based models. The proposed 3D models are introduced to simulate out-of-plane postures such as lateral flexion and lateral rotation; they are also capable of predicting human response to real-life multiple-axis WBV. In Chapter Four, the focus moves from seated positions to supine positions and a planar human supine model is introduced. The proposed model is tested under two transport conditions: a rigid case and a long spinal board attached to a military litter. In order to capture the human response under multiple-axis WBV, a 3D supine model is introduced in Chapter Five. The thesis ends with a conclusion chapter (Chapter Six) and vision for future work.

1.2 Literature Review

Studies showed that exposure to WBV such as those encountered in heavy construction, farming, and ground and aerial transportations can cause discomfort, affect safety and performance, and possibly lead to injuries. According to the literature (Amirouche, 1987a), more than twelve millions workers in the United States are affected by vibration. Therefore, it is necessary to understand how vibration is transmitted to and through the human body so we can find ways to minimize it. One way to achieve that is to implant sensors inside the human body to collect information about its biomechanical responses, a technique that can't be done due to ethical reasons. Another way to do that is to use biomechanical models that simulate human response to vibration. In this case, it becomes possible to use simple models to predict human motion at the macro-scale level (gross motion), followed by detailed finite element models that can test the effect of vibration at the micro-scale levels (tissue stresses, for example). The focus of this thesis is on the development of human models that predict motion in response to WBV at the macro-scale level with emphasis on seated and supine positions.

The following sections of this chapter present a literature review in the area of human response to WBV in seated and supine positions with a focus on human modeling and the role of posture.

1.2.1 Seated Position

Studies on human response to WBV have identified the neck and trunk areas of seated humans as a major source of discomfort and potential risk for long-term injury (Rehn et al., 2005; Johanning et al., 2006; Eger et al., 2008; Courtney and Cahn, 1999). Experiments have added a considerable amount of knowledge and understanding of the human response to the WBV environment, with most recent studies highlighting the critical role of human postures on the biodynamic response (Kittusamy and Buchholz, 2004; Mansfield and Maeda, 2005; Wang et al., 2006; Smith, 2000; Rahmatalla and DeShaw, 2011a and 2011b; Mandapuram et al., 2011).

In a study on 14 Swedish helicopter pilots with neutral neck positions and neck flexing at 20^0, Thuresson et al. (2005) found that the neck position seemed to have greater influence on the induced load and neck extensor muscle activity levels than the increase in the mass of the head-worn equipment. According to data from mining vehicle operators, operators averaged 89% of the time with their necks rotated more than 40^0, 3% of the time with trunk rotated more than 30^0(Eger, Stevenson et al., 2008). Rehn et al. (2005) showed that ATV drivers frequently use non-neutral rotational positions and that the frequency and duration of non-neutral rotational neck postures with a rotational neck movement exceeding 15^0 were relatively low. The prevalence of serious neck and lower back disorders among locomotive engineers was found to be nearly double that of the sedentary control group without such exposure (Johanning et al., 2006).

In parallel to experimentations, many attempts were conducted to develop computer human models in WBV (Griffin, 1978; Amirouche, 1987b; Amirouche, Xie et al., 1994; Kitazaki and Griffin, 1997; Yoganandan, Kumaresan et al., 1997; Boileau and

Rakheja, 1998; Fritz, 1998; Wei and Griffin, 1998; Pankoke, Hofmann et al., 2001; Seidel and Griffin, 2001; Bazrgari, Shirazi-Adl et al., 2008a; Wang, Bazrgari et al., 2010). Computer-based human models present an inexpensive and safe venue in which to perform unlimited testing, with the goal of predicting injury risk or developing better seat design. But posture was not a key issue in these models. Various biomechanical models have been developed to describe the human motion. In general, there are two types of biomechanical models that simulate human response under WBV; finite element (FE) models and multi-body dynamics models.

Finite element models are mostly introduced to investigate the effect of WBV on the human skeleton and tissues at the micro-scale level, with emphases on stress and force calculations. Finite element models are normally very detailed and can be based on high-resolution images. Still, the human body is a very complex system with many components that have different properties at different resolutions, and therefore it is very hard to model all of the human body components correctly. Cost and computational time are the main disadvantages of FE models in WBV; also, most of these models have a hard time predicting human kinematics in response to WBV, and therefore are driven by previously collected motion data.

Some of the existing FE models are characterized by a very high number of DOFs with a very complex mesh, such as the model presented by Buck and Wolfel (1998). Pankoke et al. (2001) proposed a simplified, linearized model to adapt the human weight, height, and posture based on previous models (Buck, Wolfel et al., 1998). Bazrgari et al. (2008a) presented an FE-based musculoskeletal model for the computation of spinal loads and trunk stability under vertical WBV considering high acceleration magnitudes. The model was used to calculate muscle forces, spinal loads, and trunk stability under erect and flexed lumbar postures.

Multi-body dynamic models are also widely used in modeling human response to WBV. These models can be categorized into two groups. The first group is simplified

mass-spring-damper models. These models treat the human body segments as lumped masses connected via springs and dampers (Boileau and Rakheja, 1998; Liang and Chiang, 2006; Nikolova and Toshev, 2007; Zadpoor and Nikooyan, 2010; Nikooyan and Zadpoor, 2011). Most simplified mass-spring-damper models are linear models, and segments are connected by linear springs and dampers. Coermann (1962) proposed the first multi-body seated model with 1 DOF. Two 2-DOF models are proposed under the vertical sinusoidal signals (Allen, 1978; Wei and Griffin, 1998). Suggs et al. (1969) built the first 3-DOF model. Wan and Schimmels (1995) and Boileau and Rakheja (1998) proposed 4-DOF linear models interconnected by five sets of springs and dampers. Qassem et al. (1994) and Qassem and Othman (1996) proposed 11-DOF models. A few models available considered the nonlinearity of the dynamic response of the human body by using nonlinear spring(s) or damper(s). Muksian and Nash proposed a 2-DOF model (Muksian and Nash, 1976) and one 6-DOF (Muksian and Nash, 1974) with nonlinear damper(s) or spring(s). Patil et al. (1977) proposed a 7-DOF model with all internal forces neglected.

While the mass-spring-damper elements are popular in the area of human response to vibration, most of these models are limited to one direction, mostly vertical (Boileau et al., 1998; Patil et al., 1978; Wan et al., 1995; Muksian and Nash, 1974; Qassem et al., 1994; Qassem and Othman, 1996; Allen; 1978; Wei and Griffin; 1998; Suggs et al., 1969). Another limitation to these models is their incapability to deal with rotational motion and limited to predict the position, velocity, and acceleration at selected points on the lumped masses. Most importantly, the simplified mass-spring-damper model will face significant difficulties modeling human postures.

The second group of multi-body models consists of one or several rigid segments connected by rotational or translational spring-dampers (Amirouche, 1987a; Amirouche, 1987b; Amirouche and Ider, 1988; Fard, Ishihara et al., 2003; Fard, Ishihara et al., 2003; Fard, Ishihara et al., 2004). Multi-body dynamic models assume that the human body

segments are rigid and connected by spring and damper elements at the body joints. Generally, from such models, the angular displacement, angular velocity, and angular acceleration can be predicted, and two-dimensional (2D) and 3D dynamic responses of the human body can be simulated. Cho et al., (2001) proposed a planar 9-DOF model with three rigid bodies with a backrest. Liang et al. (2008) proposed a planar 14-DOF multi-body dynamic model to simulate response to vibration considering different backrest support conditions. In general, most of these models are either limited to planar models or input vibration in a single direction, and postures are not considered.

Besides the FE and multi-body model categorization in WBV, the biodynamic human models can be also classified based on the direction of vibration. Most of the existing human models under vibration are developed to predict motion under vertical direction (Liang et al., 2008; Cho et al., 2001). Researchers (Amirouche 1987; Amirouche, Xie et al. 1994) conducted serial research in modeling human reactions to WBV in vertical direction and optimized the contact coefficients to decrease the body vibration (Allen, 1978; Wei and Griffin, 1998; Suggs et al., 1969 Qassem et al, 1994; Qassem and Othman, 1996; Muksian and Nash, 1976). Patil et al. (1977) proposed a 1-DOF or multi-DOF simplified mass-spring-damper model to simulate the seated whole human body in the vertical direction, and most of the models only considered the pure sinusoidal excitation.

Only a handful of planar human models under fore-aft WBV are presented in the literature. Rahmatalla and Liu (2012) proposed a 1-DOF head-neck model using control theory and optimization schemes. Fard (2003a, 2003b, and 2004) proposed linear planar models with 1 DOF and 2 DOF to predict the human head-neck motion.

A small number of 3D multi-body human models exist in the literature. Fritz (1998) developed a 3D biomechanical model with arms and hands to assess the health risk. Fritz also did a series of studies about WBV towards the forces acting at the lumbar spine and compared his results with those of others (Fritz, 2000a; Fritz, 2000b).

Amirouche (1987b) proposed a 3D whole-body model subjected to the pure sinusoidal signals.

The biodynamic human models can also be characterized as passive and active models. Most current models are passive, where the muscle activity is not considered. Previous studies showed a few active models that consider muscle activity. Some of these models add a feedback using control theory (Peng, Hain et al., 1996; Rahmatalla and Liu, 2012). Peng et al. (1996) presented a control system model with neural feedback controller representing the vestibulocollic and the cervicocollic reflexes (Peng, Hain et al., 1996). Another model used an active damper to represent the muscle activities to simulate the response with different magnitudes input signals(Rahmatalla and Liu, 2012).

While biomechanical models may provide comprehensive information about the system response and its physiological characteristics, simple mechanisms with muscle components may also offer a good approach to characterizing system behavior (Berthoz et al., 1992; Fritz, 1998; Luo and Goldsmith, 1991). In a recent article, Nikooyan and Zadpoor (2011) presented an overview on the advantages and disadvantages of single-body and multiple-body passive and active spring-mass-damper systems in modeling the soft tissue and muscles of the human body.

1.2.2 Supine Human Position

Whole-body vibration has been recognized as a stressor to supine humans during ground and aerial transportation (Vogel, Kohlhaas et al., 1982; Harris and Piersol, 2002; Bouchut, Van Lancker et al., 2011; Cobb, Russo et al., 2012). In the U.S., approximately 20% of deaths and 25% of cases of new spinal cord injuries are exacerbated prior to arrival at the hospital (Thurman, Burnett et al., 1994; DeVivo, 1997; Sekhon and Fehlings, 2001; Bernhard, Gries et al., 2005). It is apparent that pre-hospital transportation is very important for both civilian and military medical terms. Subjective

reports have indicated a variety of complications from vibration such as bleeding (Joshi and RSharma, 2010) and difficulty monitoring patients (Martin, 2003).

The effects and the dynamic response of WBV on human transportation remains relatively under studied. In a series of experimental studies, Huang and Griffin (2008, 2009) investigated the biodynamic response of humans in supine positions under WBV. The authors investigated the peak frequencies at several points on the human body, the effect of postures, and the nonlinearity of the supine human response to WBV. In one of these studies (Huang and Griffin, 2009), the authors used biomechanical measures such as the apparent mass and transmissibility of supine humans to investigate the effect of body location on the nonlinearity (softening) of the relaxed semi-supine, flat supine, and constrained semi-supine postures during vertical WBV. Also, the experimental results showed that resonance frequencies and the primary peak frequencies in the transmissibilities decreased with an increase in vibration magnitude. The authors showed that the nonlinearity was more apparent in the flat supine posture than in the semi-supine postures (Huang and Griffin, 2008). The authors also found that the nonlinearity was apparent in both the horizontal apparent mass and the vertical cross-axis apparent mass (Huang and Griffin, 2008).

Only a few papers were found in the literature that tackled the supine human modeling in response to WBV, mostly in the vertical direction (Vogt, Krause et al., 1973; Vogt, Mertens et al., 1978; Peng, Yang et al., 2009). Vogt et al. (1976) proposed a multi-DOF mass-spring-damper supine human model to reproduce the measured impedance and transmissibility of nine human subjects under sinusoidal vibration with a constant acceleration magnitude. Their model has four masses: the head is represented by a pure mass, and the chest, abdomen, and legs are each represented by a multi-DOF lumped parameters model. The human model was tested with no load and with load applied on each body mass to investigate the nonlinearity of the human response. The study revealed that the thorax, because of its anatomical configuration, reacted differently than the rest

of the body masses. Peng, Yang et al. (2009) proposed a 14-DOF impedance-based mass-spring-damper human-berth coupled dynamic system adopted by ISO 5892-1981, which simulates the human body with three segments representing the head, buttock, and leg. The model was used to predict the dynamic response of the human body on a railway sleeper carriage as a result of the random track vibration.

While the previous models (Vogt, Mertens et al., 1978; Peng, Yang et al., 2009) represent simplified mass-spring-damper supine-human models that can capture, to a certain degree, the relative vertical motion between the uncoupled adjacent masses, both models lack the ability to capture the rotational motions and interaction between the adjacent masses. A coupled-segment multi-body dynamics human model is introduced in this work to simulate the supine human and underlying transport system in response to vertical WBV. The human body is modeled by three segments—the head-neck, torso, and pelvis-legs—connected via joints that have translational and rotational DOF. The underlying transport system and contact surfaces are modeled using spring and damper elements. Optimization schemes based on minimizing the differences between the experiments and predicted transmissibility and phase were used in the frequency domain to characterize the parameters of the human body and the underlying transport system.

CHAPTER II

HEAD-NECK MODELING

IN THE SAGITTAL PLANE

2.1 Introduction

The objective of this chapter is to introduce human head-neck models and to simulate the head-neck system (HNS) and predict its motion in the sagittal plane in response to WBV. The chapter starts with a section that describes the head-neck motion in general and the terminologies used in WBV. Before getting into the modeling part of this work, kinematic head-neck motion is introduced first in Section 2.2. The DH method and inverse kinematic prediction are used in this section. After that, a set of experiments with fore-aft direction input signal is introduced in Section 2.3. The following sections of this chapter introduce human head-neck models. A single-DOF passive model, an inverse pendulum, is introduced in Section 2.4. The passive model comprises the head-neck bones, soft tissue, and connecting elements between the bones and the tissues, but does not consider the role of muscles. A single-DOF muscle-based model is then introduced in Section 2.5. The muscle-based model is similar to the passive model of Section 2.4, but has an additional element that represents the muscles. Finally, more realistic 2-DOF planar passive and muscle-based models are introduced in Section 2.6, where the HNS comprises two rigid links instead of one.

2.2 Head and Neck Kinematics

2.2.1 Human Head and Neck Motion

Figure 1 demonstrates the range of movement for the head-neck region based on a study conducted by the national aeronautics and space administration, man-system integration standards. Figure 1-1 shows a top view of the head-neck rotation around the vertical *z*-axis. The rotation about z-axis is considered lateral rotation. Figure 1-2 shows

the sagittal plane of the head-neck region. The rotation about the horizontal (perpendicular to the sagittal plane) y-axis represents a measure of the head-neck flexion-extension motion. Figure 1-3 shows the head-neck motion about the y-axis, which measures the lateral flexion motion.

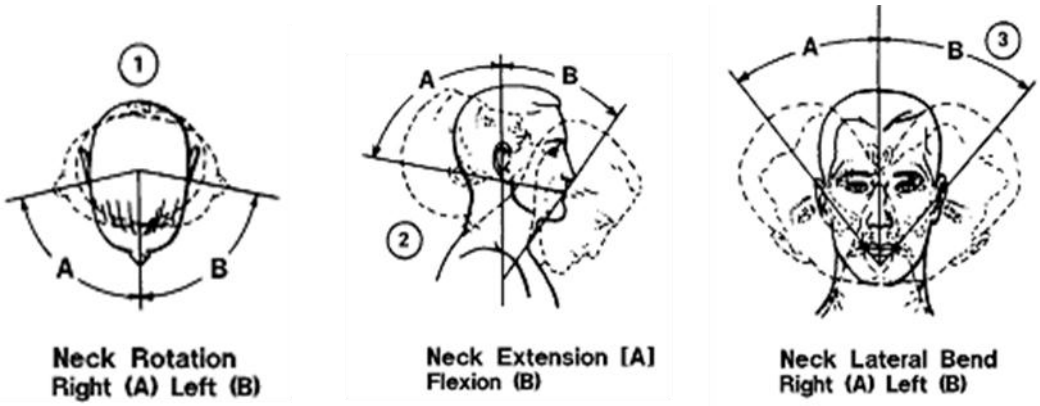

Figure 1: Neck movements. From "Joint Movement Ranges for Males and Females," National Aeronautics and Space Administration, Man-System Integration Standards. Volume 1, Section 3 Figure 3.3.2.3.1. Web April 2012.

2.2.2 Inverse Kinematics

The human body can be thought of as a mechanical system with rigid links connected by joints. The motion of the human segments can be described in the Cartesian space, where the linear displacement, velocity, and acceleration of each point can be measured. However, for the sake of calculating the kinematics and dynamics of the motion, it is sometimes more appropriate to transfer the motion from the Cartesian space to the joint space. The Denavit-Hartenberg (DH) method (Denavit and Hartenberg, 1955) is an eficient way to relate the position of a point in one coordinate system to another coordinate system using transformation matrices.

The DH method is widely used to represent human kinematics (for details, please see (Appendix B: Denavit-Hartenberg Method). The head-neck model includes few links.

Each link is connected by three revolute joints, and each revolute joint is one DOF. Thus, for a model with n links, there are $n \times 3$ DOFs. However, during the experiment, neither the position-based markers nor the accelerometers can directly record angular motions; instead they only find the positions or linear accelerations. In order to calculate the motion in the joint space, inverse kinematics is used in this case. In inverse kinematics, the unknown joint variables (angular displacement, angular velocity, and angular acceleration) are calculated using optimization methods (such as the one in the MATLAB Optimization Toolbox) that minimize the errors between the measured and calculated positions of an end-effector (the last point in a chain of connected links, for example). The objective function in the optimization method is shown as follows:

$$f = \sum_{t=0}^{t=T} (\boldsymbol{x}(\boldsymbol{q}) - \boldsymbol{x}^*(\boldsymbol{q}))^2 = \sum_{t=0}^{t=T} (x(\boldsymbol{q}) - x^*(\boldsymbol{q}))^2 + (y(\boldsymbol{q}) - y^*(\boldsymbol{q}))^2 + (z(\boldsymbol{q}) - z^*(\boldsymbol{q}))^2 \quad (2.\ 1)$$

$\boldsymbol{x}(q) = [x(\boldsymbol{q}), y(\boldsymbol{q}), z(\boldsymbol{q})]^{\mathrm{T}}$ represents the end-effector vectors; details can be seen in Appendix B (Eq. (A.3)). $\boldsymbol{x}^*(\boldsymbol{q}) = [x^*(q), y^*(q), z^*(q)]^{\mathrm{T}}$ represents the end-effector vector based on the experiments. t is the time in Eq. (2. 1). $\boldsymbol{q} = [q_1, \dots, q_N]^{\boldsymbol{T}}$ represents the design variables vector for the optimization algorithm (joint angles). The upper and lower bounds on the design variables are q_i =$[-\pi/2\,, \pi/2]$. $i = 1, \dots, N$. N is the number of DOFs of the system. The convergence tolerance for the optimization is 10e-8.

Anatomically, the cervical spine begins at C_7 and ends at the base of the skull. Seven vertebras make up the cervical spine. However, the proposed head-neck model of this study simplifies this structure to a one-link system with the base at C_7 and the end-effector at the center of the head (C_0). The relationship between the end-effector and the rotational angles (θ_1, θ_2, θ_3) is derived using the DH method. Here θ_1 represents the angle about the y-axis (neck extension and flexion in Figure 1-2), θ_2 represents the angle about

the x-axis (neck lateral in Figure 1-3), and θ_3 represents the angle about the z-axis (neck twist in Figure 1-1). The coordinate of head-neck is shown in Figure 2. C_7 is the place where the input random signal is applied at coordinate $\boldsymbol{x}_0 = [x_0(t), y_0(t), z_0(t)]^T$ and $\boldsymbol{q} = \boldsymbol{\theta} = [\theta_1, \theta_2, \theta_3]^T$.

Table 1: DH table for one-link 3D model.

Joint Number	θ_i	d_i	α_i	a_i
1	θ_3	0	90^o	0
2	$90^o + \theta_1$	0	90^o	0
3	$90^o + \theta_2$	0	90^o	0
4	90^o	L_0	0	0

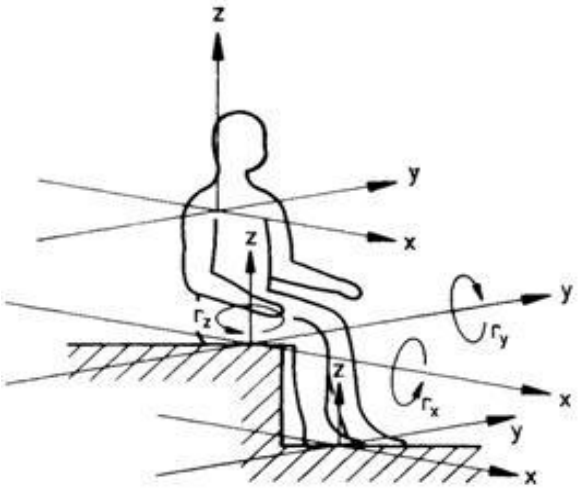

Figure 2: Whole-body motion spatial coordinate system. From "Human response to vibration.", Norsonic. Web. May, 2012. <http://www.norsonic.com/index.php?sideID=7196&ledd1=7187>.

2.3 Experiments

2.3.1 Experimental Setups

The experiments of this work were conducted at the 3D Bio-Motion Research Lab (3DMRL) at the Center for Computer-Aided Design, The University of Iowa. The study was approved by the University of Iowa Institutional Review Board (IRB, ID # 200811705), shown in Appendix D: Informed Consent Document, for human subject studies, and informed consent was obtained for each participant prior to the study.

Figure 3: The 6-DOF platform

The testing equipment consists of a MOOG-FCS motion platform (Figure 3), a rigid seat mounted on the platform (Figure 4), and a Vicon motion capture system based on passive reflective markers. The platform is a 6-DOF (longitudinal, lateral, vertical, roll, pitch, and yaw) hexapod table (Figure 3). The maximal excursion can be as much as 0.57 m or 27 degree. The velocity or angular velocity can be as much as 0.73 m/s or 35 degree/sec, while the maximal acceleration or angular acceleration is 15 m/s^2 or more than 600 degree $/sec^2$. The motion base is capable of carrying a 1500 kg payload. The Vicon motion capture system has twelve 0.3 megapixel Vicon SV cameras with a sampling rate of 200 frames/sec (200Hz sample frequency).

Figure 4: One subject seated on the seat mounted on the platform

A 12-camera Vicon system (infrared SVcam cameras with a resolution of 0.3 megapixels per frame and a peak capture rate of 200 Hz) was used to collect position data of passive reflective markers. Sixteen reflective markers were attached to the subject's skin (Figure 5a-b). The markers on the head were placed just superior and lateral to each eyebrow, as well as on each side of the back of the head. For the neck, three markers were placed on C_7-T_1, three markers were placed on C_4-C_5, one marker was placed on each side at C_1-C_2 as shown in Figure 5a-b, and one marker was placed on each side of the shoulder in Figure 5a-b. Additional markers and accelerometers were placed on the rigid platform to measure the input vibration to the system. One more marker was placed at the surface of the vest as shown in Figure 5c-d. The finite difference method was used to calculate the velocity and acceleration from the position-based markers (Rahmatalla and DeShaw, 2011a). Input vibration was generated using a 6-DOF man-rated vibration platform (Moog-FCS, Ann Arbor, MI, USA).

Subjects were strapped to a rigid seat mounted to the base of the Moog simulation platform. The seat pan was inclined at a 5 degree angle with the horizontal, and the seatback was inclined at a 14 degree angle with the vertical. The seat was covered with a soft, thin rubber to increase general comfort while maintaining seat rigidity. For each subject, the seat height was adjusted appropriately on the subject's back without obstructing the view of the C_7 vertebra for the motion capture cameras. This height allowed the subject's shoulder blades to make complete contact with the backrest. Subjects were strapped snugly to the seatback by use of a neoprene vest with three central straps and two shoulder straps, as shown in Figure 5. This was done in an effort to isolate the head-neck response from dampening effects of the middle and lower back. Quick-release buckles were included for safety, in case of an emergency.

Subjects were exposed to white-noise random fore-aft vibration signals in the sagittal plane with frequency range of 0.5-10 Hz and unweighted vibration magnitude of 1.5 m/s^2 RMS at the rigid-platform level. Each file ran for 30 second. Experiments were conducted where the subjects sat with their backs leaning and strapped to the seatback and their arms on their laps (Figure 5 a-c). The subjects were instructed to relax and take two different postures: neutral and flexion (Figure 5 c-d). The postures were maintained during the experiments by instructing the subjects to look at fixed pictures on the walls of the lab.

2.3.2 Participants

Five healthy male subjects participated in this study. They had height of 180.2 ± 32 cm and weight of 78.5 ± 21 kg, also shown in Table 2. Subjects reported no prior neck, shoulder, or head injuries, nor any neurological conditions. Written informed consent, as approved by the University of Iowa IRB, was obtained prior to testing. Subjects were seated in an uncushioned, rigid seat mounted to a vibration platform. The data from the first four subjects were used in system parameter identification; the data

from the fifth subject were used in the model validation. For the seated position, all the subjects who participated in the experiments had no history of neck or back injuries. Each subject was seated on the rigid seat attached to the MOOG-FCS motion platform. Each subject was exposed to excitation with signal frequencies of 0.5-10 Hz at discrete amplitudes about 1.5 RMS, random vibration signal for 30 seconds.

Table 2: Height and weight of subjects

Basic Information about 5 subjects		
Subject	Height(m)	Weight(Kg)
1	1.79	79.0
2	1.83	99.8
3	1.82	70.0
4	1.8	63.5
5	1.77	80.0

2.3.3 Experimental measurement for single-input single-output (SISO) system

The transfer function between the input and the output vibration signals is determined in this work using the cross-spectral density (CSD) function method (Paddan and Griffin, 1988a, b) in Eq. (2. 2).

$$H_s(f) = \frac{G_{xy}(f)}{G_{xx}(f)} \quad (2.\ 2)$$

where $G_{xy}(f)$ is the CSD of the output acceleration at C7 and the input acceleration at C_0, $G_{xx}(f)$ is the auto-spectral density of the horizontal acceleration and the input C_0

The advantage of using the CSD method is that the function can capture the phase between the input and output. The transfer function, $H_s(f)$ for the seated position, is defined in this work as the complex ratio between the output represented by the angular

acceleration of the head and the input signals represented by the fore-aft linear acceleration applied at C_7.

The model parameters are calculated from the human experimental data using the system identification method, as will be shown later; they cannot be based on the data of one subject but have to be the average of the data of all subjects. In this work, the geometric mean is used instead of the algebraic mean to represent the general dynamic response of the HNS. The geometric mean of the transfer function shown in Eq. (2. 2) reduces the effects of noise corruption and gives an unbiased estimation of the transfer function, which is better than that of the arithmetic mean(Schoukens and Pintelon 1990).

$$H_g = \prod_{k=1}^{n} \sqrt[n]{H_k(f)} \quad n = 4 \tag{2. 3}$$

It is expected that the experimental data will contain some noise; therefore, the data were filtered with a low-pass filter at 16 Hz.

Considering the model in the sagittal plane, only the neutral and flexion postures can be demonstrated in this chapter. The magnitude of the experimental transmissibility and the geometrical transmissibility are shown in Figure 6 (thick gray lines). In this figure, the transmissibility represents the relationship between the input random vibration, applied in the x direction at C_7 ($\ddot{x}_o(t)$) and the output acceleration in the x direction of the end-effector at C_0. Each gray line in Figure 6 represents the magnitude of the transmissibility from one subject; the thick black line represents the mean transmissibility of the first five subjects using Eq. (2.3). According Figure 6, the resonant frequency of the subjects at each posture is slightly different between subjects (inter-subject variability). For the neutral posture, the resonant frequency is around 1.3 Hz; for the flexion posture, the resonance frequency is around 1.8 Hz. For three of the subjects, the second peak frequency around 6.6-8 Hz can be demonstrated in Figure 6. In general, all subjects showed similar motion patterns.

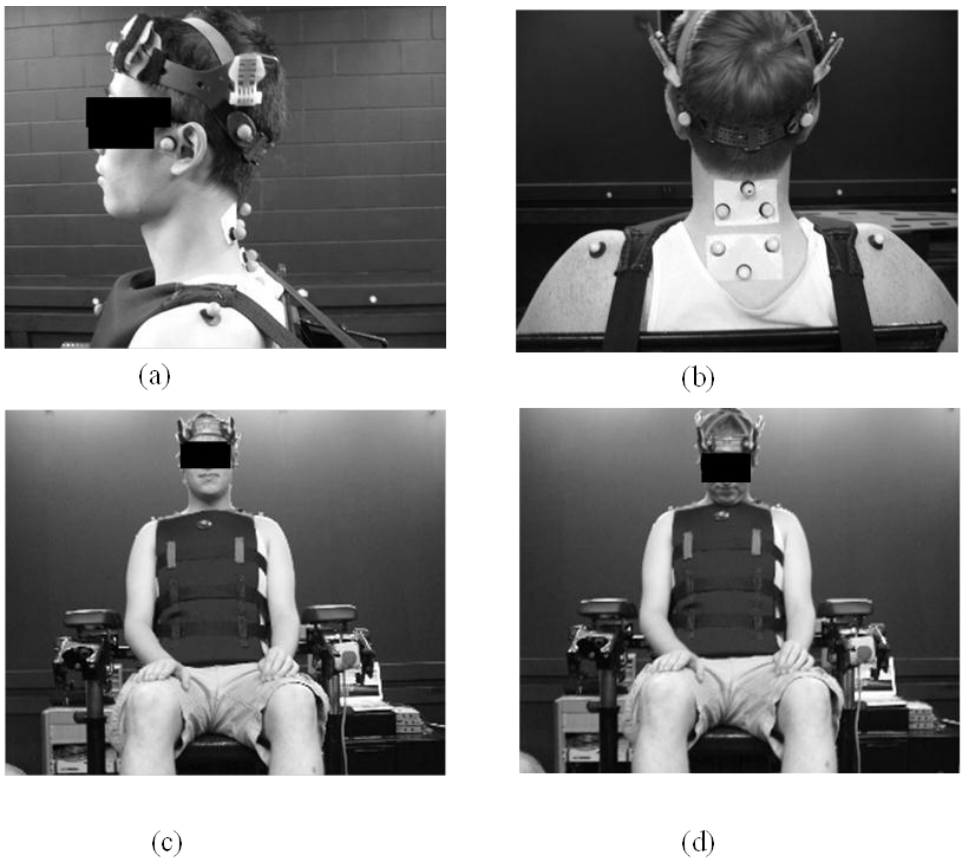

Figure 5: Marker protocol and subject seated postures during testing. (a) side view of marker locations on the head and neck, (b) back view of marker locations on the head and neck, (c) neutral posture, (d) flexion posture.

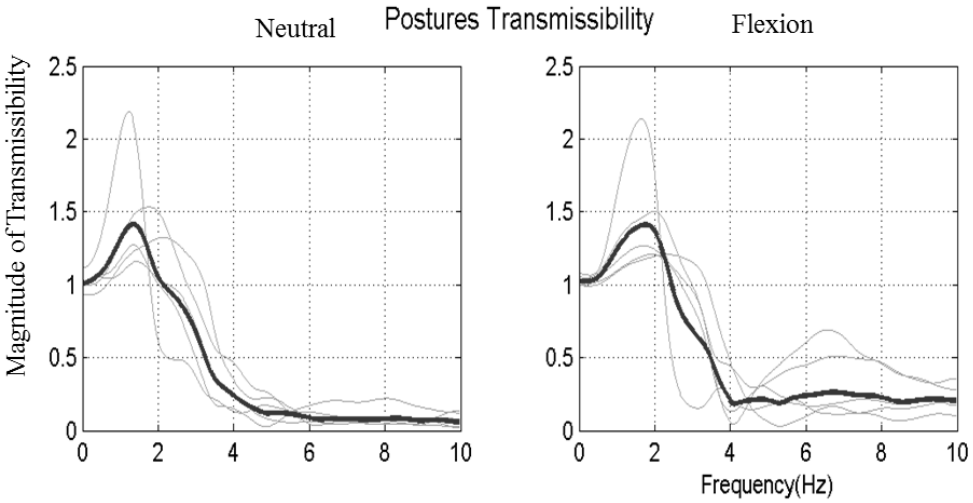

Figure 6: Mean transmissibility magnitude (thick black lines) and five subjects' experimental transmissibility magnitude (gray thin lines).

2.4 Single-degree-of-freedom Passive Model

A simplified single-DOF head-neck model (Figure 7) is first introduced in this chapter to simulate the HNS and to predict the head-neck motion in the sagittal plane under WBV. The proposed model comprises a rigid link, representing the head and neck bones, connected to a rotational joint that represents the seventh cervical vertebra (C_7). A linear torsional spring with a stiffness coefficient k and a linear torsional damper with a damping coefficient c are introduced to model the soft tissue and the connecting elements between the head-neck bones(Winter 2005). The mass of the HNS is simplified by a lumped mass (m) as shown in Figure 7. The head-neck parameters k and c are identified by the frequency domain system identification method (Kollar, 2001) using experimental data from five participants.

2.4.1 Dynamic Equation

For this inverted pendulum single-DOF model, there are a few assumptions. Firstly, the center of the mass of the head is at the center of the head (C_0) with coordinate

$\{x_e, z_e\}$. Secondly, each part of the vibration model is assumed to be slightly vibrated around the equilibrium position. The input single $\ddot{x}_0(t)$ is assumed to be applied at C_7 with coordinate $\{x_0, z_0\}$. The linear dynamic formula is derived by Lagrange's equation.

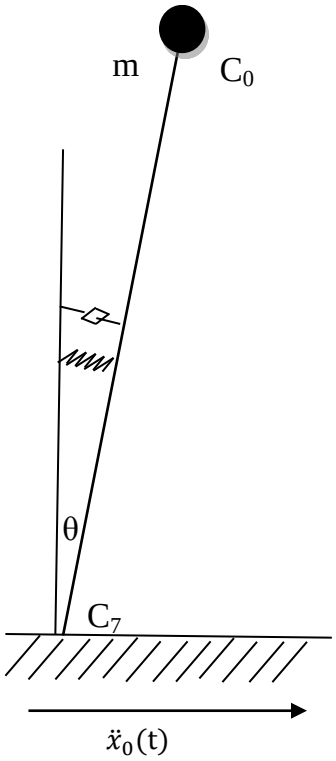

Figure 7: Single-DOF skeletal model

$$Lar = T - V \tag{2. 4}$$

$$\frac{d}{dt}\left(\frac{\partial Lar}{\partial \dot{\theta}}\right) - \frac{\partial Lar}{\partial \theta} + \frac{\partial D}{\partial \dot{\theta}} = 0 \tag{2. 5}$$

$$T = \frac{1}{2}mv^2 + \frac{1}{2}I\dot{\theta}^2 \tag{2. 6}$$

$$\text{Where, } v^2 = \left(\frac{\mathrm{d}x_e}{\mathrm{dt}}\right)^2 + \left(\frac{\mathrm{d}z_e}{\mathrm{dt}}\right)^2 = \dot{x}_e{}^2 + \dot{z}_e{}^2 \tag{2. 7}$$

$$V = mgz_e + \frac{1}{2}k\theta^2 \tag{2. 8}$$

$$D = \frac{1}{2}c\,\dot{\theta}^2 \tag{2. 9}$$

where Lar is the Lagrangian equation, T is the kinetic energy, V is the potential energy, and D is the dissipation function. The dynamic equation Eq. (2.13) can be derived based on Eq. (2. 5). c and k are unknown parameters representing the soft tissue and bone, and l_o is the length of the head-neck from the experiments, $\theta = \theta_0 + \hat{\theta}$, θ_0 is the postural angle, which is assumed to be the equilibrium starting position. For different postures, θ_0 is different (Himmetoglu, Acar et al., 2007). Table 3 demonstrated that the ranges for θ_0 are 22-40 degree for neutral postures with an average of 31 degree, and 44-54 degree for the flexion posture with an average of 50 degree.

$$l_o = l_n + l_h \tag{2. 10}$$

where l_n is the length of neck, l_h is the distance between the upper neck and the center of the head (C_0); m is the mass of the head and neck,

$$m = m_h + m_n \tag{2. 11}$$

where m_h is the mass of head and m_n is the mass of neck, which can be identified from the anthropometric data(Himmetoglu, Acar et al., 2007). According to Dempster and Gaughran (1967) and Winter (1979), the mass of the human head-neck is 8.1% of the total body mass. I is the moment of the inertia of the head-neck,

$$I = I_n + I_h + m_n {l_{nc}}^2 + m_h {l_0}^2 \tag{2. 12}$$

Table 3: Single-DOF initial angles (degree) of five subjects with respect to two different postures with x direction input signal

	Neutral	Flexion
subject1	-30.8366	-54.2591
subject2	-33.9879	-45.2006
subject3	-27.9489	-52.947
subject4	-22.0417	-44.2037
subject5	-40.6571	-51.9272

$$I\ddot{\hat{\theta}} + c\dot{\hat{\theta}} + (k - mgl_o cos\theta_0)\hat{\theta} = ml_0\ddot{x}_0 cos\theta_0 \quad (2.13)$$

From now on, $\hat{\theta}$ will be considered as θ. Thus Eq. (2.13) will become Eq. (2.14).

$$I\ddot{\theta} + c\dot{\theta} + (k - mgl_o cos\theta_0)\theta = ml_0\ddot{x}_0 cos\theta_0 \quad (2.14)$$

Table 2 shows the initial joint angle θ_0 calculated from the experiments based on the single-DOF system. This table shows that even for the same posture, different subjects have different initial angles. Thus, one advantage of this model is that the model considers θ_0 shown in Table 3 as one known parameter in the dynamic Eq.(2.14) and simulates the human response based on θ_0. The detail can see Appendix A

2.4.2 Parameter Identification

The dynamic Eq. (2.14) in the time domain can be transferred to the s-domain using the Laplace transformation with zero initial condition as shown in Eq. (2.15)

$$T_r(s) = \frac{s^2}{\frac{I}{ml_o\cos(\theta_0)}s^2 + \frac{c}{ml_o\cos(\theta_0)}s + \frac{k - mgl_o\cos(\theta_0)}{ml_0\cos(\theta_0)}} e^{-T_d s} \quad (2.15)$$

$T_r(s)$ demonstrates the theoretical relationship between the angular acceleration ($\ddot{\theta}$) and input acceleration signal at C_7($\ddot{x}_0$), where $s = 2\pi fi$ and f is the frequency. There are seven parameters in Eq. (2.15): c, k, T_d, θ_0, m, I and l_o. Among these parameters, θ_0 is the postural angle, which can be calculated, based on the experimental results in Table 3. The mean value of the first four subjects is used here during the identification process. l_o, m, and I can be calculated based on Eq. (2.10), (2.11), and (2.12), respectively. The mean value of the four subjects is used for the system identification as well. T_d is a fixed pure time delay of the HNS, which can be estimated before the system parameter identification (Fard, Ishihara et al., 2004). The value of T_d in this case turns out to be $10 \times e^{-3}$ sec (depending on the current experimental data). There are only two unknown parameters, c and k. Therefore the frequency domain system identification method is used here to identify the damper and spring stiffness coefficients (Kollar, 2001).

The optimization results are illustrated in Table 4 and the passive model process is shown in Figure 8.

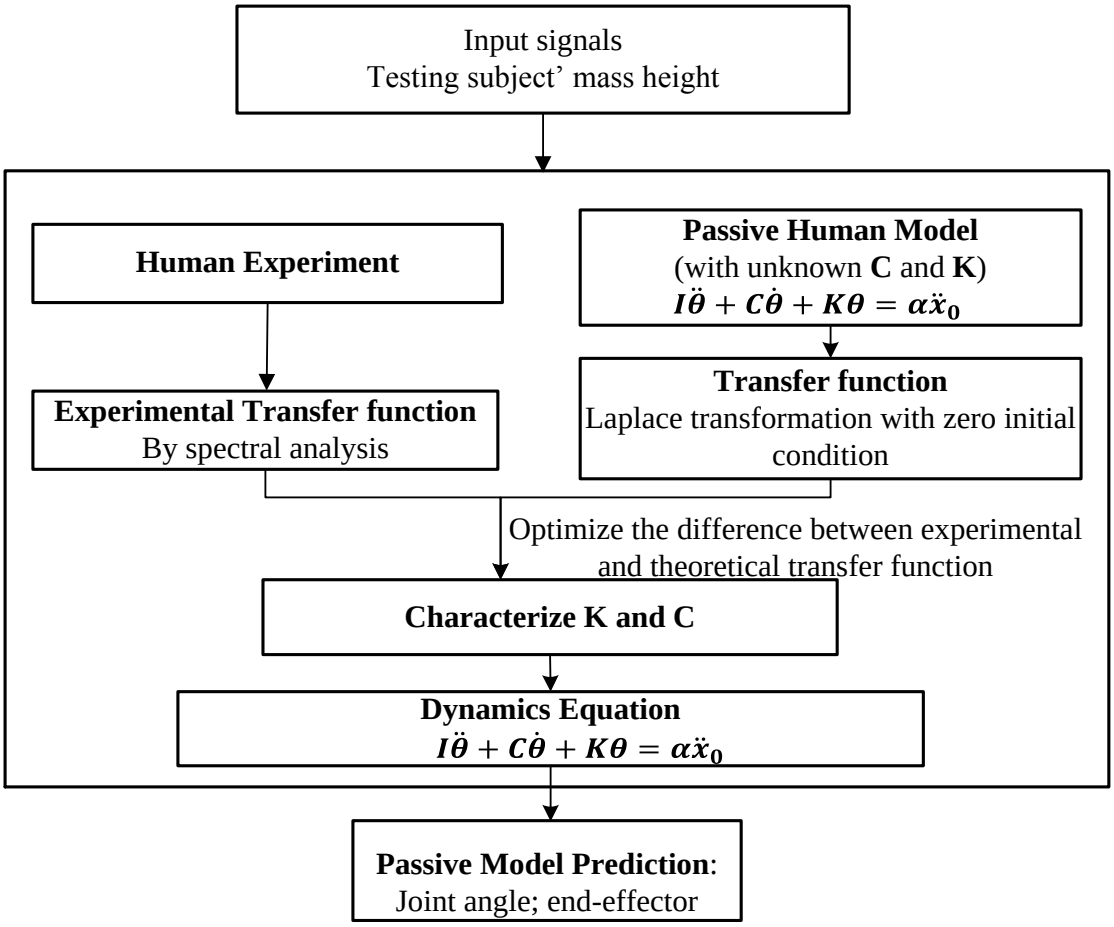

Figure 8: Passive skeletal model and prediction flow chart

Table 4: Optimization results

Damper (Nm/(rad·s))	Stiffness (Nm/rad)	Natural frequency (Hz)
C_b=0.36	K_b=9.14	*fn=2.493*

2.4.3 Results

The purpose of this chapter is to predict the head-neck response under input random fore-aft WBV. In order to evaluate the model prediction capability, a new set of experimental response data, based on a new subject (subject 5), is used to validate the proposed model. It is worth mentioning here that the parameters θ_0, m, I, and l_o are all based on the measurement of the new subject (subject 5), instead of the mean values of the four subjects used in the database.

The results of the prediction based on subject 5 are illustrated in Figure 9-10. The black thick solid lines represent the passive model prediction of subject 5, and the gray dashed lines represent the experimental testing of subject 5.

The results in the time domain are shown in Figure 9 and Figure 10. It looks like the model can reasonably predict the angular acceleration and angle in the time domain for both postures under investigation. For the frequency domain, the power spectal density (PSD) of the acceleration of the passive model and experiments are illustrated in Figure 9. In general, the proposed passive model with the identified parameters are able to predict all trends and peaks at low frequencies. However, at high freuqencies, especially after 8 Hz, the model generates some errors.

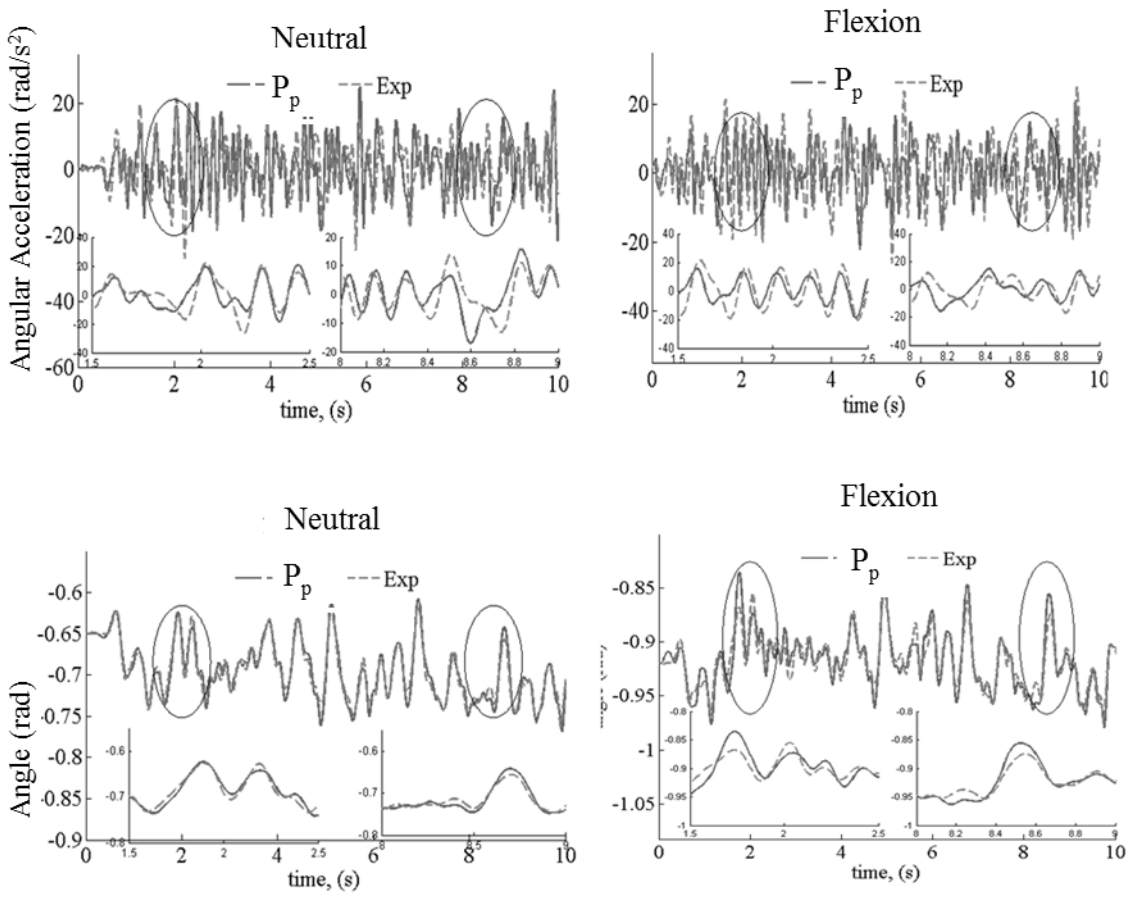

Figure 9: Joint angle and angular acceleration of the experimental (Exp) and skeletal passive models (P_P) in the time domain. The black circles in the figures are zoomed-in areas.

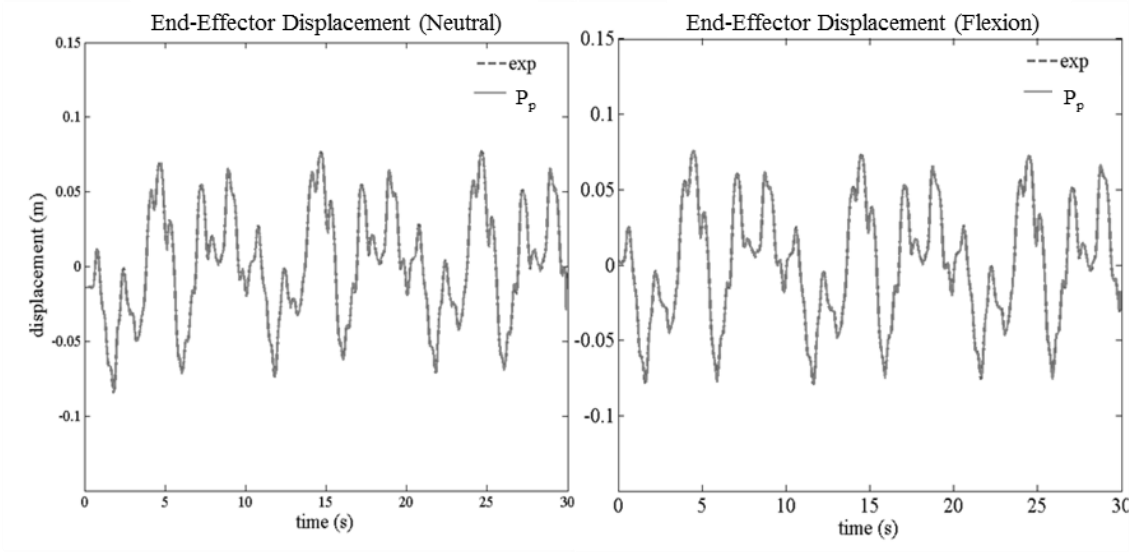

Figure 10: Displacement of end-effector in neutral and down postures.

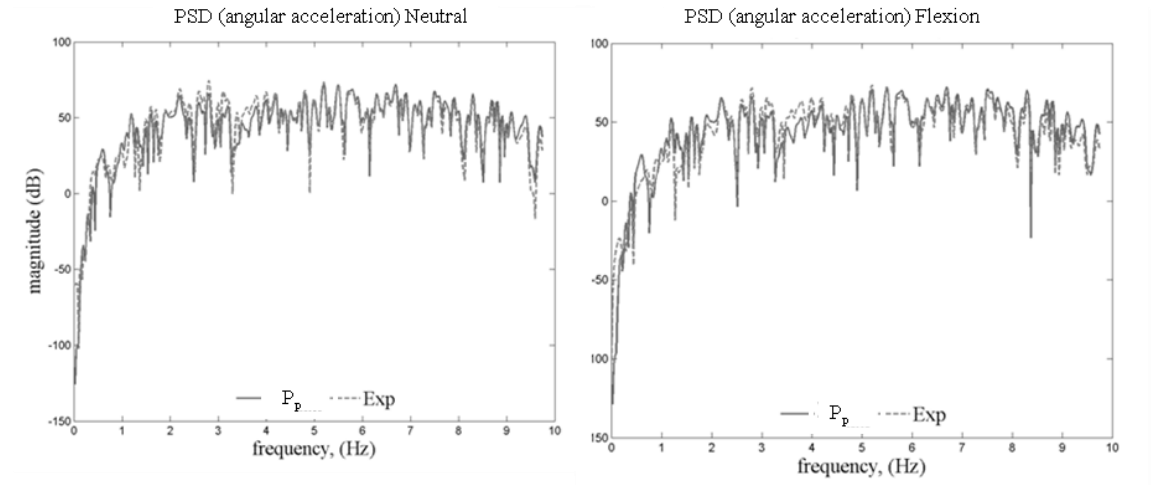

Figure 11: Angular acceleration PSD of the experiment and simulated results with respect to neutral and down postures.

2.5 Single-degree-of-freedom Muscle-based Model

The model proposed in Section 2.4 is a passive model. According to Figure 8, the passive model includes a mass, damper, and spring. The damper and the spring represent

the tissues and the connecting elements with the bones. It is expected that the addition of a muscle component would improve the human system response.

2.5.1 Muscle Component

For the skeletal muscles, which are responsible for body movement, the activation forces are normally proportional to the position, velocity, and external disturbances (Winter, 1979; Winter, 2005). In WBV, this process becomes more complicated as random motions enter the human body. In this case, it is expected that humans will involuntarily activate their muscles to minimize the relative motion between their body segments and maintain their preferred postures.

Previous studies showed that muscle activation is sensitive to the acceleration. In a study (Rahmatalla, Smith et al., 2010) on five seated subjects under fore-aft WBV with a supported-back condition, the neck and back muscles demonstrated activities at frequencies where large motion occurred. Another study (Rahmatalla and DeShaw, 2011b) showed that both the subjective reported discomfort and the biodynamic response (seat-to-head transmissibility) of 10 subjects were affected by the changes in the angular acceleration of the subject joints, indicating that the subjects can sense and respond to the acceleration. A study by Marras and Mirka (1990) also showed that the muscle activities are sensitive to the asymmetric trunk angular acceleration.

The hypothesis behind the proposed muscle component of this work is that in WBV, the muscle behaves like a motion-resistive component that generates resistive forces to the external vibration-motion in proportion to the input displacement, velocity, acceleration, and jerk. The proposed muscle component in principle is similar to Hill's model and to that proposed by Winter (1979, 2005); however, the force-actuating component is modeled as shown in Figure 14a. In the angular representation of this model (Chapman, 1983) shown in Figure 14 (b), the resistive force of the muscle is a function of the angular displacement, angular velocity, angular acceleration, and angular

jerk. The mass in this component represents the effective mass of the muscle and the connective tissues, which are affected by the acceleration of the muscle (Winter, 1979 and 2005).

There are three types of muscles: skeletal, heart, and smooth. Skeletal muscle makes up a major part of the human body. The motion of the human body is mostly achieved by skeletal muscle.

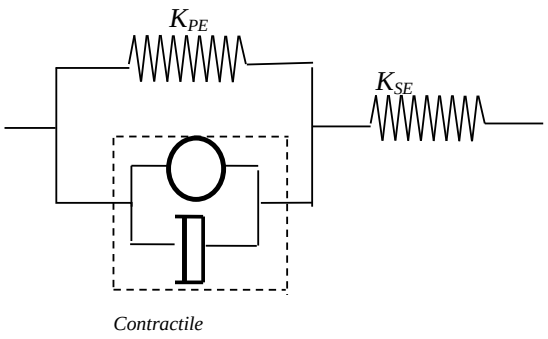

Figure 12: Hill's model (Winter, 1979)

The proposed muscle component is a modification to Chapman's model, which itself is a modification of Hill's model(Hill, 1938; Hill, 1953). Figure 11 is a predominant muscle model used widely in the biomechanical field, especially for simulating the multiple joint systems. In the model, the muscle has two components, the contractile component (CC) and the series elastic component (SEC), as shown in Figure 11. Many models have been derived from Hill's model by adding one more parallel elastic (PE) component. Thus, the proposed muscle component can be shown in Figure 13. The equation derivate is shown in Eqs. (2.16-2.22).

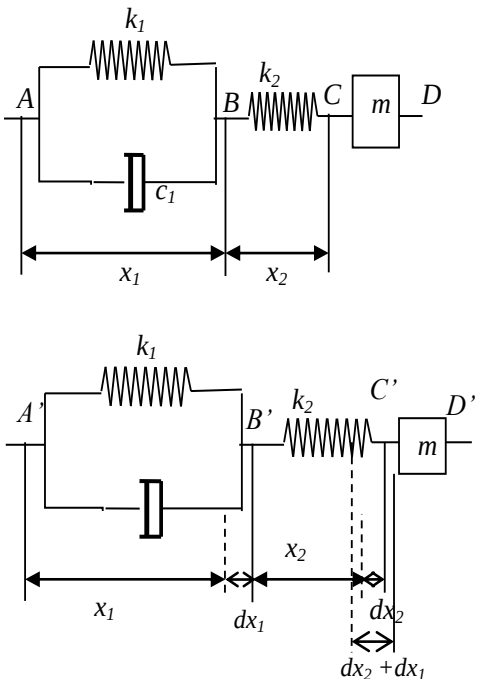

Figure 13: Muscle component

$$F_{AB} = c_{\mathrm{m}}\dot{x}_1 + k_{\mathrm{a}}x_1 \tag{2. 16}$$

$$x = x_1 + x_2 \tag{2. 17}$$

$$F_{BC} = k_{\mathrm{b}}x_2 \tag{2. 18}$$

$$F_{CD} = M_m(\ddot{x}_1+\ddot{x}_2) = M_m\ddot{x} \tag{2. 19}$$

$$F = F_{AB} = F_{BC} = F_{CD} \tag{2. 20}$$

Where the force CC contractile component is represented as F_{AB} and shown in Figure 13 A'B' section; the force of SEC is represented as F_{BC} and shown in Figure 13 B'C' section. And m is the mass of muscle, F_{CD} is the force by the muscle mass.

Thus, based on Eqs. (2.16) and (2.28):

$$x_1 = x - \frac{M_m}{k_{\mathrm{b}}}\ddot{x} \tag{2. 21}$$

$$\dot{\mathrm{x}}_1 = \dot{\mathrm{x}} - \frac{\mathrm{M_m}}{k_{\mathrm{b}}}\dddot{\mathrm{x}} \tag{2. 22}$$

Interpolating Eq. (2.21) and Eq. (2.22), Eq. (2.16) can be illustrated as:

$$F_M = c_m\left(\dot{x} - \frac{M_m}{k_b}\dddot{x}\right) + k_1\left(x - \frac{M_m}{k_b}\ddot{x}\right) = -c_m\frac{M_m}{k_b}\dddot{x} - k_1\frac{M_m}{k_b}\ddot{x} + c_m\dot{x} + k_a x =$$
$$c_m(-P\dddot{x} + \dot{x}) + k_a(-P\ddot{x} + x), \text{ where } P = \frac{M_m}{k_b} \quad (2.\ 23)$$

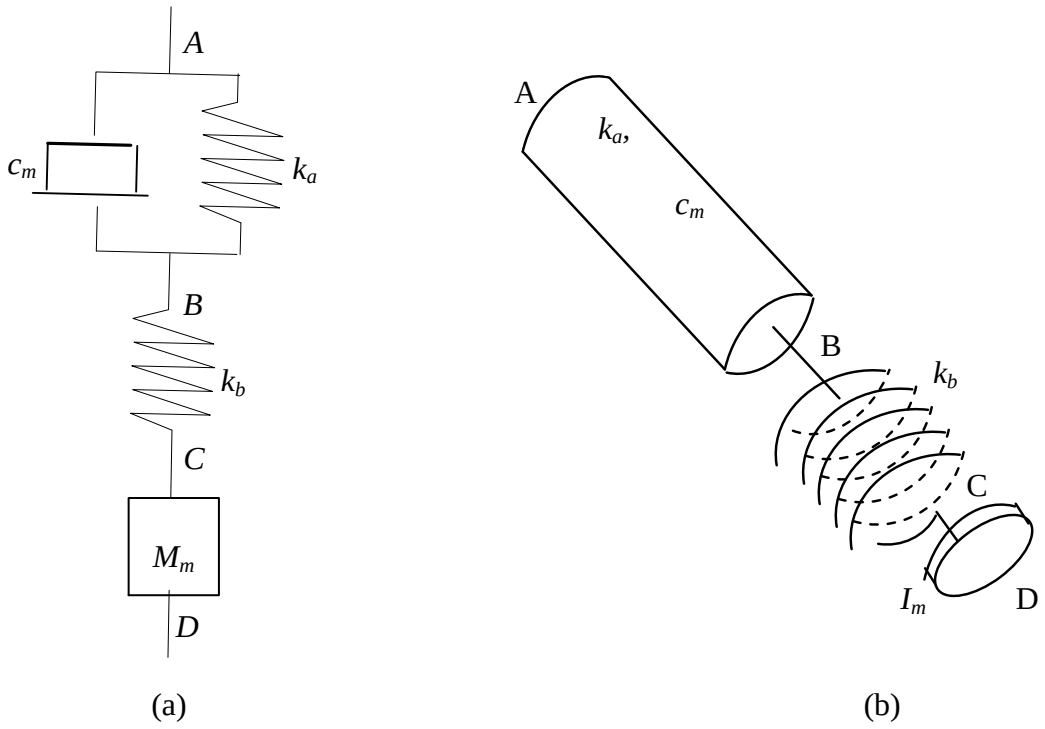

Figure 14: The proposed muscle model. (a) In the linear form, AB comprises a spring (k_a) and damper (c_m), BC comprises a spring, and CD comprises a lumped mass. (b) In the rotational form, AB comprises a rotational spring (k_a) and rotational damper (c_m), BC comprises a rotational spring, and CD comprises a lumped mass with inertia I_m.

When describing Hill's model in angular terms, the model is represented by a torque and angle (Chapman, 1983). Similar to Figure14a, the rotational muscle component is illustrated as Figure14b. AB is similar to the contractile element of Hill's model, but it is made by a rotational dashpot and an elastic rotational spring. BC represents the series elastic component, a linear rotational spring, representing the effect of the tendon, and CD is the inertia of muscle. This model demonstrates the torque of the muscle due to the angular displacement, angular velocity, angular acceleration, and

angular jerk. Unlike Chapman's model, the CC component is made by a spring and a dashpot. The moment produced by muscle is denoted as M_M. The muscle force conponents can be shown as follows.

The muscle model in the linear form is shown in Figure14a. Similarly, when the muscle model is in the rotational form shown in Figure14b, the resulting equation of the muscle moment can be demonstrated in Eq. (2.24). The angle of AB (CC) is θ_1, the angle of BC is θ_2, and the angle of CD is $\theta = \theta_1 + \theta_2$. Thus, $\theta_1 = \theta - \theta_2$, and then $\theta_1 = \theta - (I_m/k_\mathrm{b})\ddot{\theta}$, $\dot{\theta}_1 = \dot{\theta} - (I_m/k_\mathrm{b})\dddot{\theta}$.

$$M_M = c_m\left(\dot{\theta} - \frac{I_m}{k_b}\ddot{\theta}\right) + k_a\left(\theta - \frac{I_m}{k_b}\ddot{\theta}\right) = -C_m\frac{I_m}{k_b}\dddot{\theta} - k_a\frac{I_m}{k_b}\ddot{\theta} + c_m\dot{\theta} + k_a\theta = C_m(-P\dddot{\theta} + \dot{\theta}) + k_a(-P\ddot{\theta} + \theta), \text{ where } P = \frac{I_m}{k_\mathrm{b}} \quad (2.24)$$

Based on the dynamic Eq. (2.14), the dynamic muscle-based model equation can be written as follows:

$$I\ddot{\theta} + c\dot{\theta} + (k - mgl_o cos\theta_0)\theta = ml_0\ddot{x}_0 cos\theta_0 - M_M \quad (2.25)$$

The muscle-based model is based on the passive skeletal model with an extra muscle component that captures the extra muscle response. The parameters of muscle, including c_m, $k_{a,}$and P, were calculated based on optimizing the differences between the passive model and experimental measurement. These differences are the muscle component. The results of transmissibility, which demonstrates the relationshiop between input signal($\ddot{x}_0$) and output accerlation at end-effector in the x direcion($\ddot{x}_\mathrm{e}$), are shown as follows. As shown in Figure 16, the passive skeletal model(P_p) and muscle-based model (M_M) are both pretty good before 4Hz for both postures. However, after 4Hz, the passive skeletal model is not a very stable model, while the muscle-based model is more stable and closer to the experimental measurement (Exp).

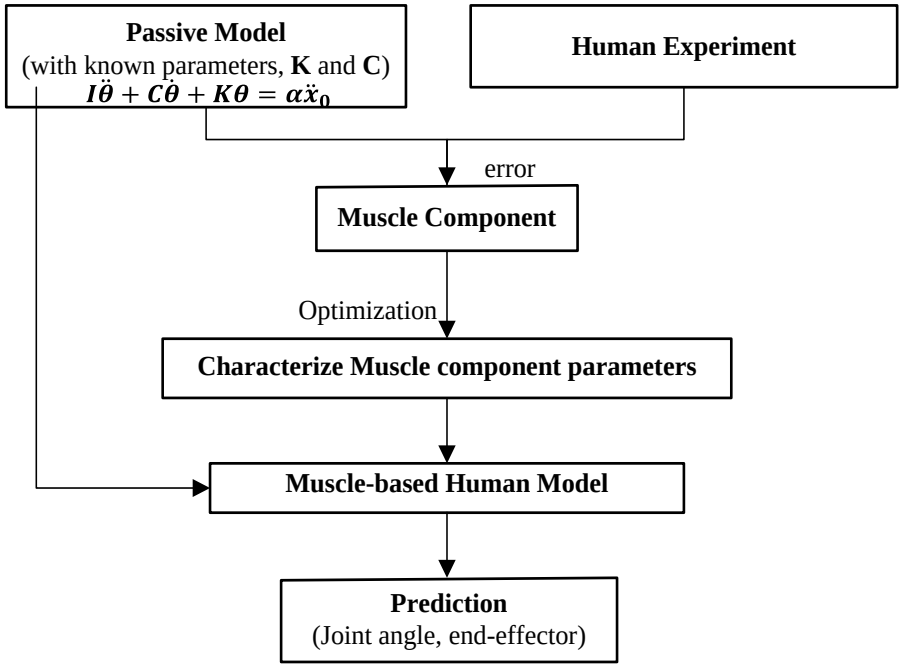

Figure 15: Muscle-based model and prediction flow chart.

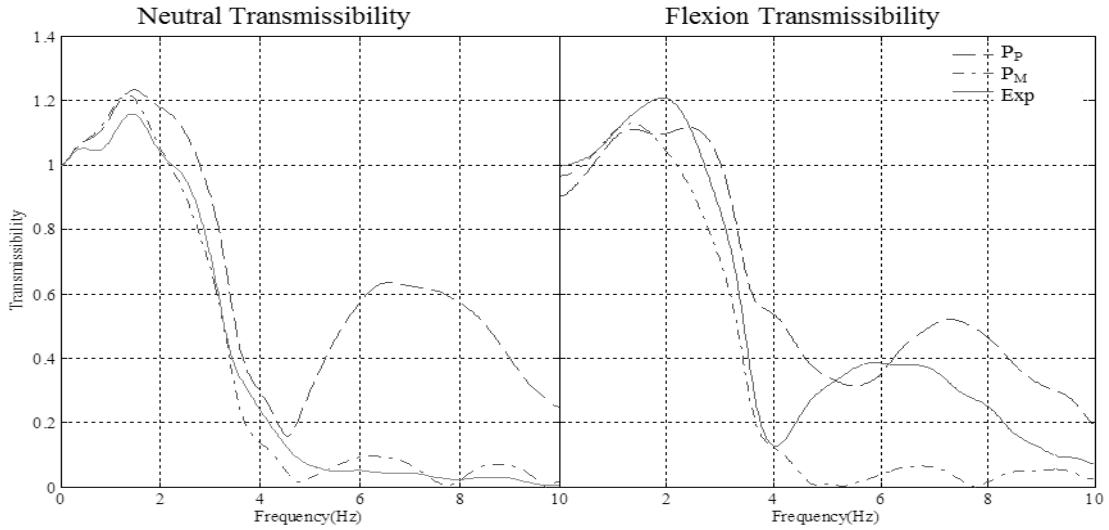

Figure 16: Transmissibility of neutral and flexion and postures. The transmissibility is between input acceleration signal $\ddot{x}_0$ and output acceleration at end-effector in x direction ($\ddot{x}_e$).

2.5.2 Excitations at Different Magnitudes

Studies in WBV (Nawayseh and Griffin, 2005b; Hinz, Menzel et al., 2010; Wang, Bazrgari et al., 2010) have demonstrated a nonlinear behavior of the human response under increasing vibration magnitudes. The nonlinearity is characterized by a softening response with increased magnitude of vibration, meaning that the peak frequencies of the human body become smaller with increasing vibration magnitudes. This change in human characteristics may also affect human perception to discomfort and injury risk(Mansfield and Griffin, 2000).

A series of experiments has been conducted by several researchers(Hinz, Seidel et al., 2002; Nawayseh and Griffin, 2005a; Nawayseh and Griffin, 2005b; Wang, Bazrgari et al., 2010), with the goal of investigating and finding an explanation for the nonlinearity of the upper body in response to different vibration magnitudes(Hinz, Seidel et al., 2002; Nawayseh and Griffin, 2005a; Nawayseh and Griffin, 2005b; Wang, Bazrgari et al., 2010). The latter studies showed that the response of the human body to vertical and fore-aft directions is sensitive to the vibration magnitudes and therefore demonstrates nonlinearity in the response. Roberson and Griffin (1989) showed that a doubling of the vibration magnitude did not result in a doubling of the EMG activity. They related this behavior to a softening system in the muscle forces. They concluded that the peak frequencies and the non-linearity in the response may be caused by a complex combination of sources that could include the dynamic response of the tissue beneath the ischial tuberosities, the bending or buckling response of the spine, and the active response of the muscles. Thus, passive human models that are based on optimization at one vibration magnitude may be inappropriate for capturing the responses of humans at different vibration magnitudes.

While the non-linearity of the human biodynamic and the softening behaviors have been investigated experimentally by several researchers, the work has still mainly focused on the spine area of the human body (Huang and Griffin, 2009;Mansfield and

Griffin, 2000). To the author's knowledge, there is only one study that investigates the nonlinearity of the cervical spine response under different vibration magnitudes (Rahmatalla and Liu, 2012). In addition to affecting the capability of the human model to predict human response at different vibration magnitudes, the nonlinearity in human response and the softening behavior play a significant role on the design of vibration suppression systems in seats. With different vibration magnitudes, the critical harmful frequencies will be shifted, which may decrease the effectiveness of the seats' suspension systems if the latter is designed to target certain frequencies based on one vibration magnitude. Therefore, the development of computer human models that can capture the softening characteristic of the human body response under different vibration magnitudes will enable the improvement of spinal and cervical models as well as the design of seats with better performance.

The objective of this work is to investigate the capability of the proposed passive and muscle-based head-neck model in capturing the nonlinearity under the fore-aft WBV of different magnitudes. In order to test these behaviors, a new set of experiments was carried out. Random input fore-aft vibration files containing five different magnitudes—0.55 m/s^2 RMS (Mag 1), 0.99 m/s^2 RMS (Mag 2), 1.44 m/s^2 RMS (Mag 3), 1.73 m/s^2 RMS (Mag 4), 2.15 m/s^2 RMS (Mag 5)—were used. Five subjects participated in the experiments. The details of the physical parameters of the subjects are illustrated in Table 5. Input vibration files of Mag 4 with data from Subjects 1, 2, 4, and 5 were randomly chosen to build the database for the system identification. The data from Subject 3 were used to test the validity of the proposed HNS to capture the softening behaviors under vibration magnitudes of Mag 1, Mag 2, Mag 3, and Mag 5.

Transmissibility of experimental results is shown in Figure 18 (solid line), which shows behaviors similar to those found in previous work(Hinz, Seidel et al., 2002; Nawayseh and Griffin, 2005a; Nawayseh and Griffin, 2005b). Our experimental results also show the reduction of the transmissibility with rising magnitude excitation.

Table 5: Basic information about subjects

Basic Information about Five Subjects		
Subject	Height (m)	Weight (Kg)
1	1.89	90.7
2	1.77	71.0
3	1.72	65.6
4	1.78	86.3
5	1.78	62.3
Average	1.788	75.182

The resulting acceleration in the x direction is shown in Figure 17. The figure on the left shows the time domain results with respect to Mag 1, Mag 2, Mag 3, Mag 4, and Mag 5, with the figures on the right showing zoom-in snapshots at a time range of 1-3 seconds. In this figure, most of the time, the muscle-based model is closer to the experimental results, and the passive model tends to have bigger motion.

Figure 18 shows the transmissibility results with respect to five different magnitudes. The left figure shows the experimental results compared with the muscle-based model. The figure on the right is the passive skeletal model compared with the experimental results. Figure 18 shows the reduction in the transmissibility magnitudes and the shift in the resonance frequencies with increasing vibration magnitudes. The muscle-based model is more stable than passive model when it comes to frequency after 5Hz.

Figure 19 shows the comparison between the passive and muscle-based models. The left figure shows the magnitude of the transmissibilities. As we can see in the figure, both models are able to simulate the magnitude. The muscle-based model is more accurate than the passive model (all the black bars are closer to the dots bars). When it comes to the capture the peak frequency, as shown in Figure 19 (left), the passive model is slightly better for capturing the peak frequency at Mag 1 and Mag 4. The muscle-based

model is better for capturing the peak frequency at Mag 3 and Mag 5 than the passive model. It is hard to tell about Mag 3.

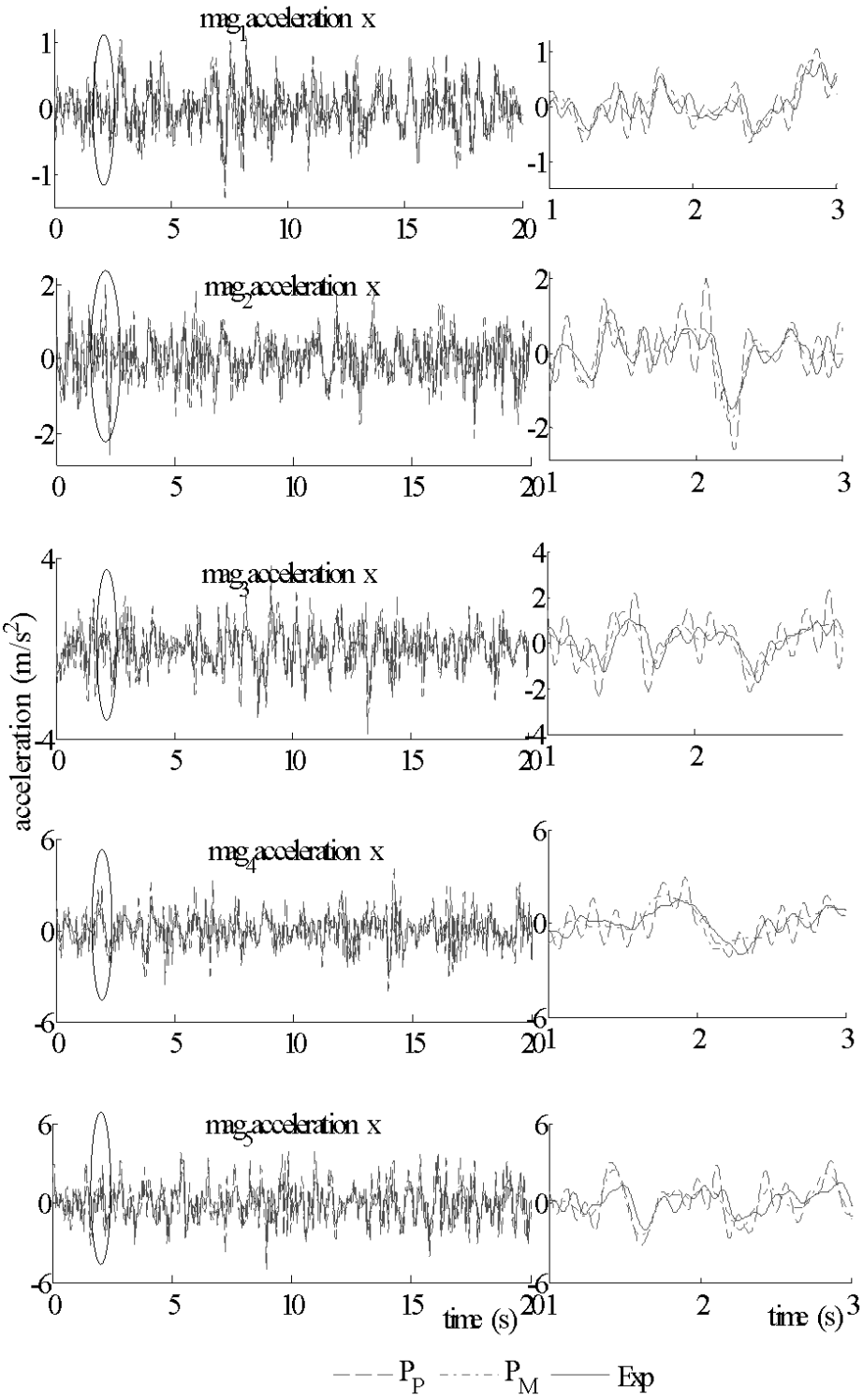

Figure 17: x direction acceleration with five different magnitudes. The gray dashed line is the passive skeletal model; the brown dashed-dotted line is the muscle-based model; and the pink solid line is the experimental testing.

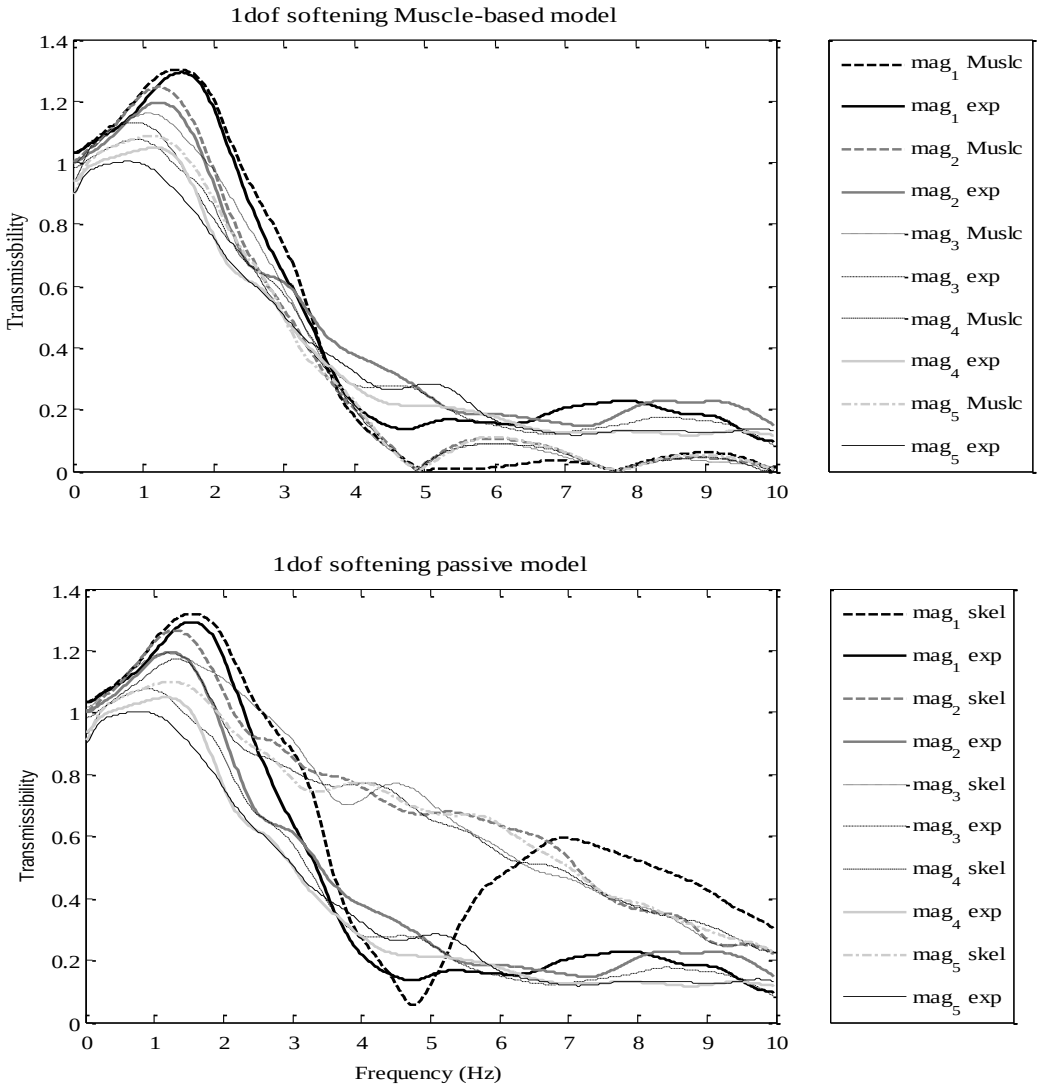

Figure 18: Transmissibility of different magnitudes. The picture on the top shows results of muscle-based model and experiments; the picture on the bottom shows the results of the skeletal model and experiments.

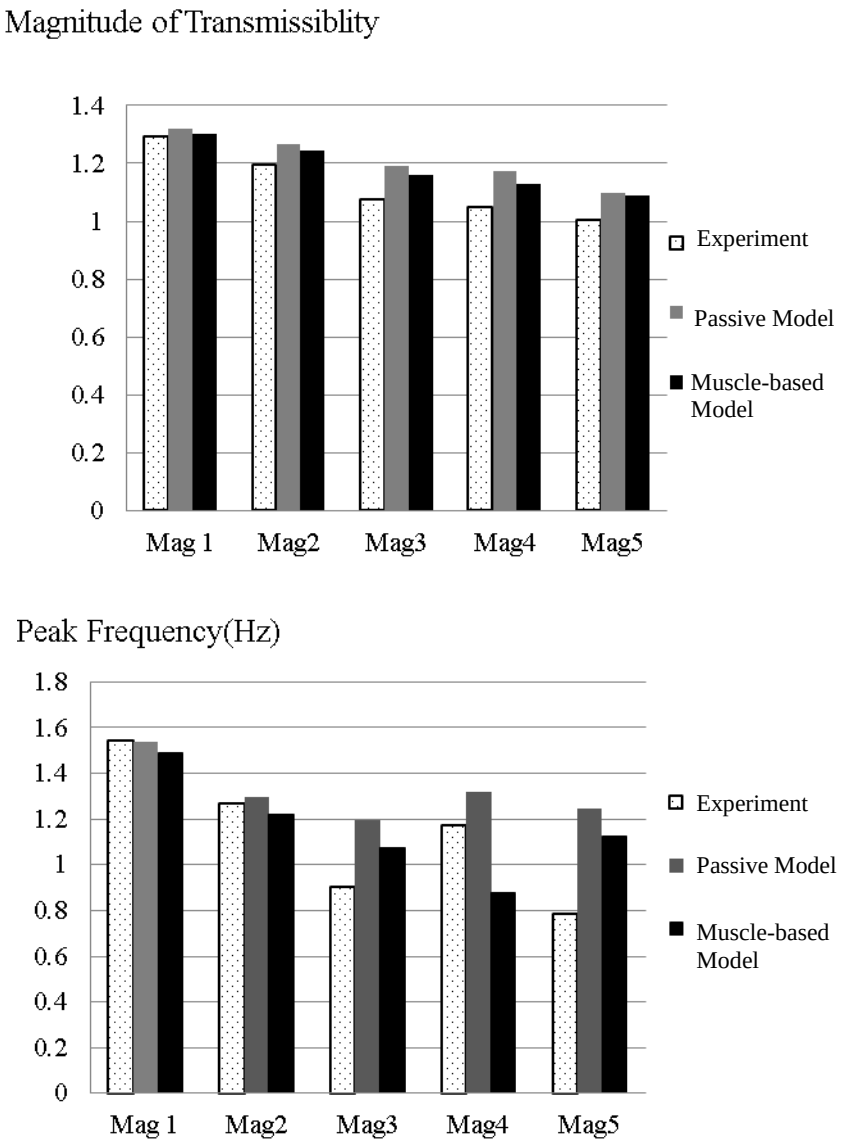

Figure 19: Transmissibility reduction and softening. Maximum transmissibility is on the top; peak frequency is on the bottom.

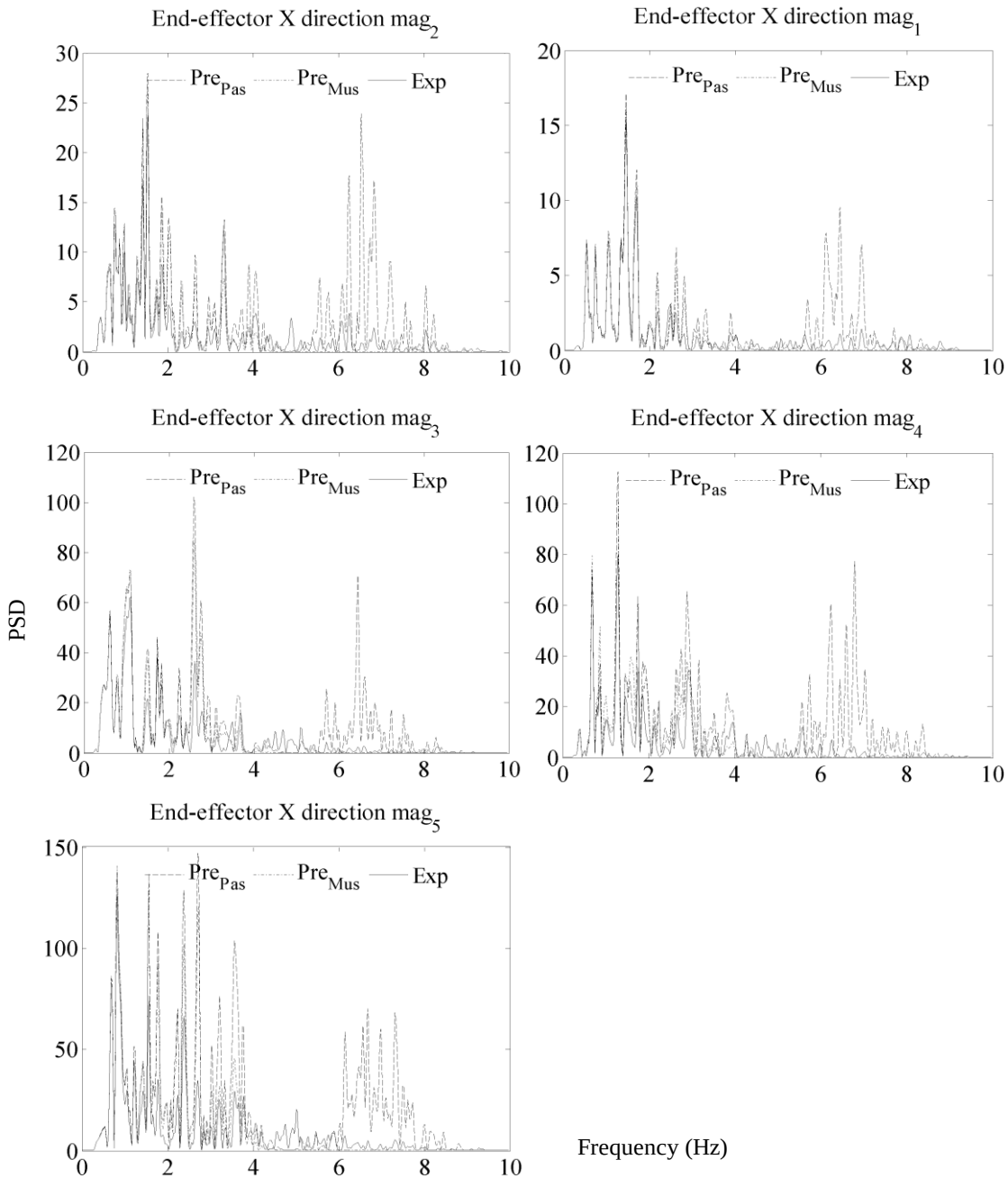

Figure 20: End-effect PSD with different magnitudes. In the figure, the dashed line is the passive model (Pre_{Pas}), the dotted-dashed line is the muscle-based model (Pre_{Mus}), and the solid line is the experiment data (Exp)

2.6 Two-degree-of-freedom Passive Model

In Section 2.5 and Section 2.4, single-DOF inverse pendulum models were introduced (Figure 7). A single DOF, while very useful, is simplistic and may not capture the response of the individual segments that comprise the HNS. Thus, a multi-DOF system is proposed in this section, which can be generalized to more DOFs in the future. Similar to a single-DOF model, a double inverted pendulum with two DOFs was proposed in this section as shown in Figure 21. It is assumed that the human HNS has two links. The first link represents the neck from C_7-C_1, whose mass is m_1, and the second link represents the head, C_0, whose mass is m_1. Accordingly, a two-lumped mass represents the mass of the neck and head. For the first link, the center of mass is at the center of the neck, which is assumed to be in the middle of Link 1.

2.6.1 Dynamic Equation

According to Lagrange's equation (Eq. (2. 5)), the multi-DOF head and neck dynamic equation is shown in Eqs. (2.26) – (2.28).

$$\mathrm{T} = \frac{1}{2}m_1{v_1}^2 + \frac{1}{2}m_2{v_2}^2 + \frac{1}{2}I_1{\dot{\theta}_1}^2 + \frac{1}{2}I_2{\dot{\theta}_2}^2 \tag{2. 26}$$

$$V = m_2 g z_e + m_1 g z_1 + \frac{1}{2}k_1{\theta_1}^2 + \frac{1}{2}k_2{\theta_2}^2 \tag{2. 27}$$

$$\mathrm{D} = \frac{1}{2}c_1\,{\dot{\theta}_1}^2 + \frac{1}{2}c_2\,{\dot{\theta}_2}^2 \tag{2. 28}$$

where ${v_2}^2 = (\frac{\mathrm{d}x_e}{\mathrm{dt}})^2 + (\frac{\mathrm{d}z_e}{\mathrm{dt}})^2 = {\dot{x}_\mathrm{e}}^2 + {\dot{z}_e}^2$; ${v_1}^2 = (\frac{dx_1}{dt})^2 + (\frac{dz_1}{dt})^2 = {\dot{x}_1}^2 + {\dot{z}_1}^2$ and $\boldsymbol{\theta} = \{\theta_1\ \theta_2\}^{\boldsymbol{T}}$. I_1 and I_2 are the inertia of neck and head, respectively.

The coordinate of joint between neck and head is $(x_1'\quad z_1')$, shown in Eq. (2.29); the coordinate of the center of neck $(x_1\quad z_1)$ is illustrated in Eq. (2.30); and the coordinate of the end-effector is C_0 $(x_e\quad z_e)$, illustrated in Eq. (2.30).

$$\begin{cases} x_1' = x_0 + \sin(\theta_1 + \theta_{10})L_1 \\ z_1' = \cos(\theta_1 + \theta_{10})L_1 \end{cases} \tag{2. 29}$$

$$\begin{cases} x_1 = x_0 + \sin(\theta_1 + \theta_{10}) l_1 \\ z_1 = \cos(\theta_1 + \theta_{10}) l_1 \end{cases} \quad (2.\ 30)$$

$$\begin{cases} x_e = \sin(\theta_1 + \theta_{10}) L_1 + \sin(\theta_2 + \theta_{20}) L_2 + x_0 \\ z_e = \cos(\theta_1 + \theta_{10}) L_1 + \cos(\theta_2 + \theta_{20}) L_2 \end{cases} \quad (2.\ 31)$$

where L_i, i=1 and 2 is the total length of each. l_i is the distance between the joint and the mass center in each link. In this case, it is assumed that the center of the second link, head is also the center of mass, thus $L_2 = l_2$.

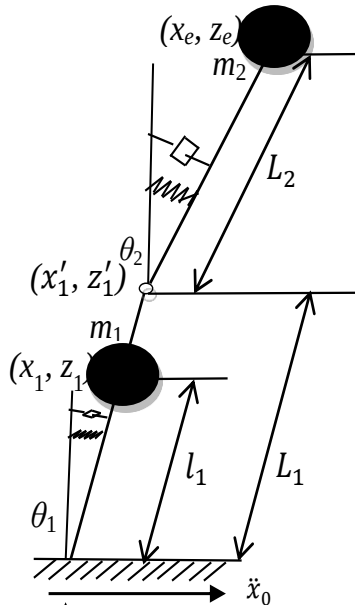

Figure 21: Two-DOF model.

The dynamic equation is shown in Eq. (2.32). In this equation, for a 2-DOF system, $\boldsymbol{I}$ is inertia matrix in Eq. (2.33), $\boldsymbol{C}$ is damping matrix shown in Eq. (2.45), and $\boldsymbol{K}$ is the stiffness matrix illustrated in Eq. (2.34). $\boldsymbol{I}$, $\boldsymbol{C}$, and $\boldsymbol{K}$ are 2 x 2 matrices. $\boldsymbol{\alpha}$ is a constant n-element vector, shown in Eq. (2.36). Consider a two-DOF model; $\boldsymbol{I}$, $\boldsymbol{C}$, $\boldsymbol{K}$, and $\boldsymbol{\alpha}$ can be calculated using Lagrange's equation. $\boldsymbol{\theta} = [\theta_1, \theta_2]^{\boldsymbol{T}}$

$$\boldsymbol{I\ddot{\theta} + C\dot{\theta} + K\theta = \alpha\ddot{x}_0} \quad (2.\ 32)$$

$$\boldsymbol{I} = \begin{bmatrix} \frac{m_1 {L_1}^2}{4} + I_1 + I_2 + {L_1}^2 m_2 & L_1 L_2 m_2 cos(\theta_{10} - \theta_{20}) \\ L_1 L_2 m_2 cos(\theta_{10} - \theta_{20}) & m_2 {L_2}^2 + I_2 \end{bmatrix} \quad (2.\ 33)$$

$$\boldsymbol{K} = \begin{bmatrix} -\frac{1}{2} g L_1 m_1 cos\theta_{10} - g L_1 m_2 cos\theta_{10} + k_1 + k_2 & -k_2 \\ -k_2 & k_2 - g L_2 m_2 cos\theta_{20} \end{bmatrix} \quad (2.\ 34)$$

$$\boldsymbol{C} = \begin{bmatrix} c_1 + c_2 & -c_2 \\ -c_2 & c_2 \end{bmatrix} \quad (2.\ 35)$$

$$\boldsymbol{\alpha} = \begin{bmatrix} -\cos(\theta_{10}) l_1 m_1 - \cos(\theta_{10}) L_1 m_2 \\ -\cos(\theta_{20}) L_2 m_2 \end{bmatrix} \quad (2.\ 36)$$

where $\theta_{10}$and θ_{20} are initial static equilibrium postural angles for the neutral and flexion postures. The details are illustrated in Table 6.

Table 6: Two-DOF initial angles (deg) of five subjects with respect to two different postures.

	θ_{10}(degree)		θ_{20} (degree)	
	Neutral	Flexion	Neutral	Flexion
subject1	-43.35	-62.46	4.21	-6.80
subject2	-43.02	-52.49	1.43	-2.88
subject3	-36.97	-58.79	1.90	-7.31
subject4	-32.77	-51.90	4.58	-4.52
subject5	-54.48	-64.29	0.02	-5.21
Average	-42.12	-57.99	2.43	-5.34

2.6.2 Parameter Identification

By transferring the dynamic equation, Eq. (2.32), into the s domain, the transfer function of the system, $\boldsymbol{T_r}(s)$, is obtained. Here the transfer functions $T_1(s)$ and $T_2(s)$ represent the relationship between the input acceleration signal $\ddot{x}_0$ and output acceleration signal $\ddot{\theta}_1$ and $\ddot{\theta}_2$.

$$\boldsymbol{T_r}(s) = (\boldsymbol{I s^2} + \boldsymbol{C} s + \boldsymbol{K})^{-1} \boldsymbol{\alpha s^2} \quad (2.\ 37)$$

where $\boldsymbol{T_r}(\mathrm{s}) = \{T_{r_1}(s), T_{r_2}(s)\}^{\mathrm{T}}$.

In order to fit the theoretical transfer function in Eq. (2.37) to the experimental measurement, the optimization method by Callafon and Van den Hof (1996) and Kollar (2001) is used. In Eqs. (2.33)-(2.37), all the lengths, including l_1, L_1 and L_2, and the mass of each link (m_1 and m_2) can be estimated based on the participant's anthropometry (Dempster and Gaughran, 1967; Winter, 1979; de Leva, 1996). L_1, L_2 can be measured from experiment data. Inertia (I_1 and I_2) can be calculated based on previous research(de Leva, 1996; Himmetoglu, Acar et al., 2007).

$$f^{obj} = \sum_{i=1}^{2} \sum_{f} \left\{ \frac{|T_{r_i}(f)| - |T_{ri}^*(f)|}{\| |T_{r_i}(f)| - |T_{ri}^*(f)| \|} \right\}^2 + \sum_{i=1}^{2} \sum_{f} \left\{ \frac{Pha\left(T_{r_i}(f)\right) - Pha\left(T_{ri}^*(f)\right)}{\left\| Pha\left(T_{r_i}(f)\right) - Pha\left(T_{ri}^*(f)\right) \right\|} \right\}^2 \quad (2.38)$$

The design variables of the optimization problem are the unknown parameters $\mathbf{x}^r$, $\mathbf{x^r} = \{x_1, x_2, x_3, x_4\}^T = \{k_1, k_2, c_1, c_2\}^T$. The objective function is f^{obj}; Eq. (2.38) represents the normalized differences between the predicted and experimental transfer function magnitude and phase, where $T_{ri}^*(f)$ represents the experimental transfer function and $T_{r_i}(f)$ represents the theoretical transfer function in Eq. (2.37). $|.|$ represents the magnitude of transfer function, and $Pha(.)$ represents the phase of the transfer function.

The upper bounds limits on the design variables are considered as $\mathbf{UB^T}$: $\mathbf{UB^T} = \{1000, 1000, 100, 100\}$. The lower bounds limits are considered as $\mathbf{LB^T}$: $\mathbf{LB^T} = \{0.001, 0.001, 0.001, 0.001\}$. The starting points for the design variables are denoted as $\mathbf{x_0}^T$, $\mathbf{x_0}^T = \{1, 1, 1, 1\}^T$. The frequency (f) in Eq. (2. 38) is considered from 0 Hz to 10 Hz. The optimization results are illustrated in Table 7.

2.6.3 Two-degree-of-freedom Muscle-based Model

The muscle-based model for two DOF is the same as the single-DOF muscle model (see Section 2.5). The dynamic equation is demonstrated as follows:

$$\boldsymbol{I\ddot{\theta} + C\dot{\theta} + K\theta = \alpha\ddot{x}_0 - M_M} \quad (2.39)$$

where $\boldsymbol{M_M} = \{M_{M1}, M_{M2}\}^{\boldsymbol{T}}$

$$M_{Mi} = c_{mi}\left(\dot{\theta}_i - \frac{I_{mi}}{k_{bi}}\ddot{\theta}_i\right) + k_{ai}\left(\theta_i - \frac{I_{mi}}{k_{b_i}}\ddot{\theta}_i\right) = C_{mi}(-P_i\ddot{\theta}_i + \dot{\theta}_i) + k_{ai}(-P_i\ddot{\theta}_i + \theta_i)$$

where $P_i = \frac{I_{mi}}{k_{\mathrm{b}}i}$ and i=1, 2 represents number of the joints. The parameters of muscle components are calculated by optimization. $\boldsymbol{M_M}$ can be calculated based on passive skeletal model and experimental results. Then optimization is used to calculate the parameters of $\boldsymbol{M_M}$, including c_{m1}, k_{a1}, P_1, c_{m2}, k_{a2}, and P_2.

Table 7: Optimization results for model with two DOF in the sagittal plane.

Damper (Nm/(rad·s))	Stiffness (Nm/rad)	Damper (Nm/(rad·s))	Stiffness (Nm/rad)
c_1=2.303879	k_1=65.81563	c_2=0.0927099	k_2=37.047440

2.6.4 Results

The results of the two-DOF model are shown in Figures 22-24. When it comes to the time domain, in general, the muscle-based model is better than the passive skeletal model.

Figure 22Figure 22 shows the angular acceleration results in the time domain for the first 4 seconds. For the first link, the magnitude of motion of the angular acceleration is greater than the experimental testing. On the other hand, the angular acceleration of the passive model is smaller than that of the experiment for both postures. When it comes to the second link, the passive and muscle-based models show reasonable prediction, but the results of the muscle-based model are slightly better than those of the passive model.

Figure 23 shows the results of the angular displacement in the time domain for both postures for the first 4 seconds. For both models, the first link, close to joint C7, showed better predictions than the second link. The muscle-based model showed slightly better results than the passive model. However, when it comes to the second joints, the muscle-based model showed much better prediction than the passive model. These

behaviors are consistent with the experimental testing, where the human head-neck showed more sensitivity to the second link, especially when it came to different postures. Concerning the x direction movement of the end-effector, both models show very good motion prediction, as shown in Figure 24.

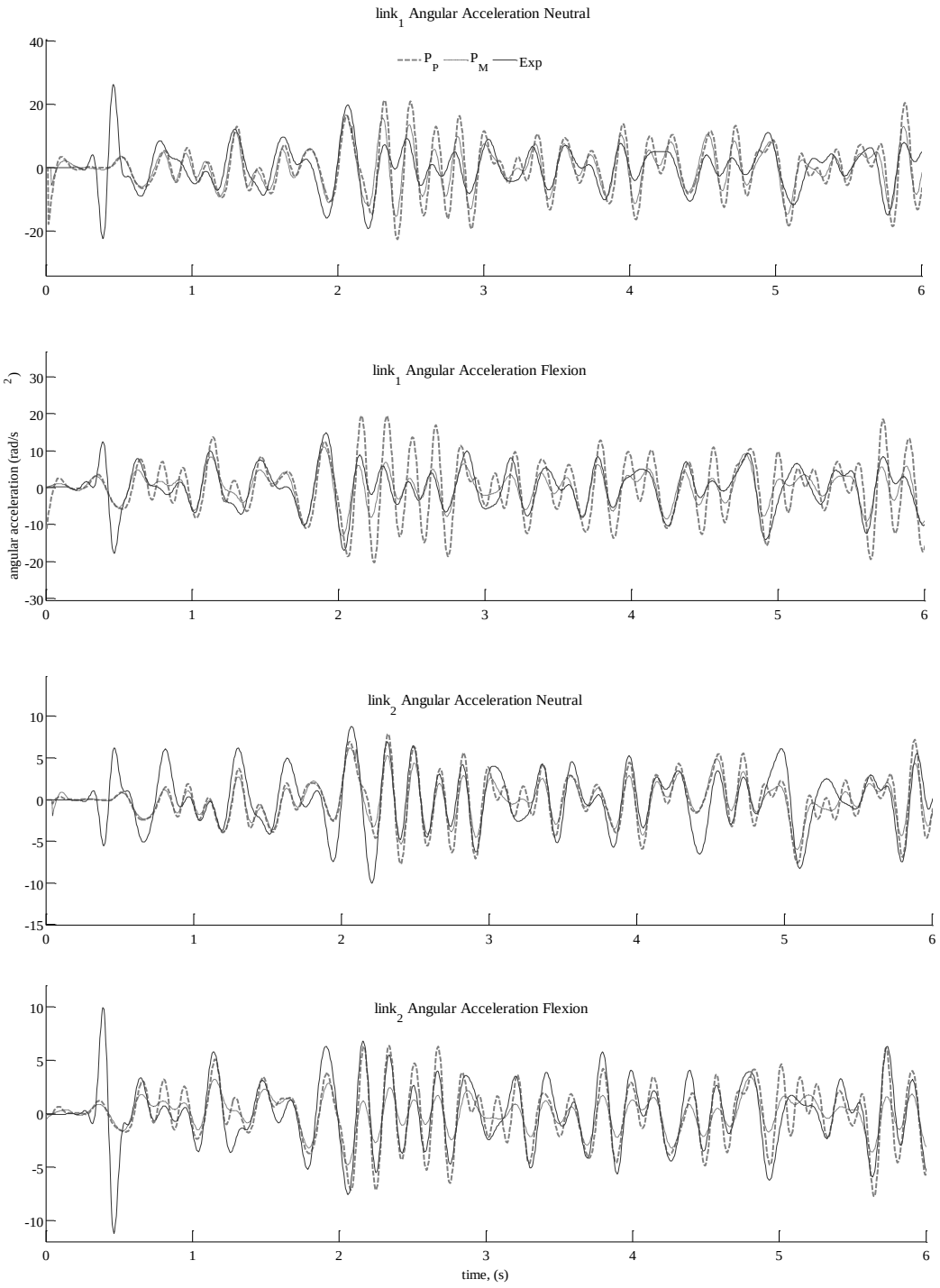

Figure 22: Angular accelerations with respect to neutral and flexion postures; The P_p is the skeletal passive model (gray dashed line), P_M is the muscle model (black dotted line), and Exp (continuous black line).

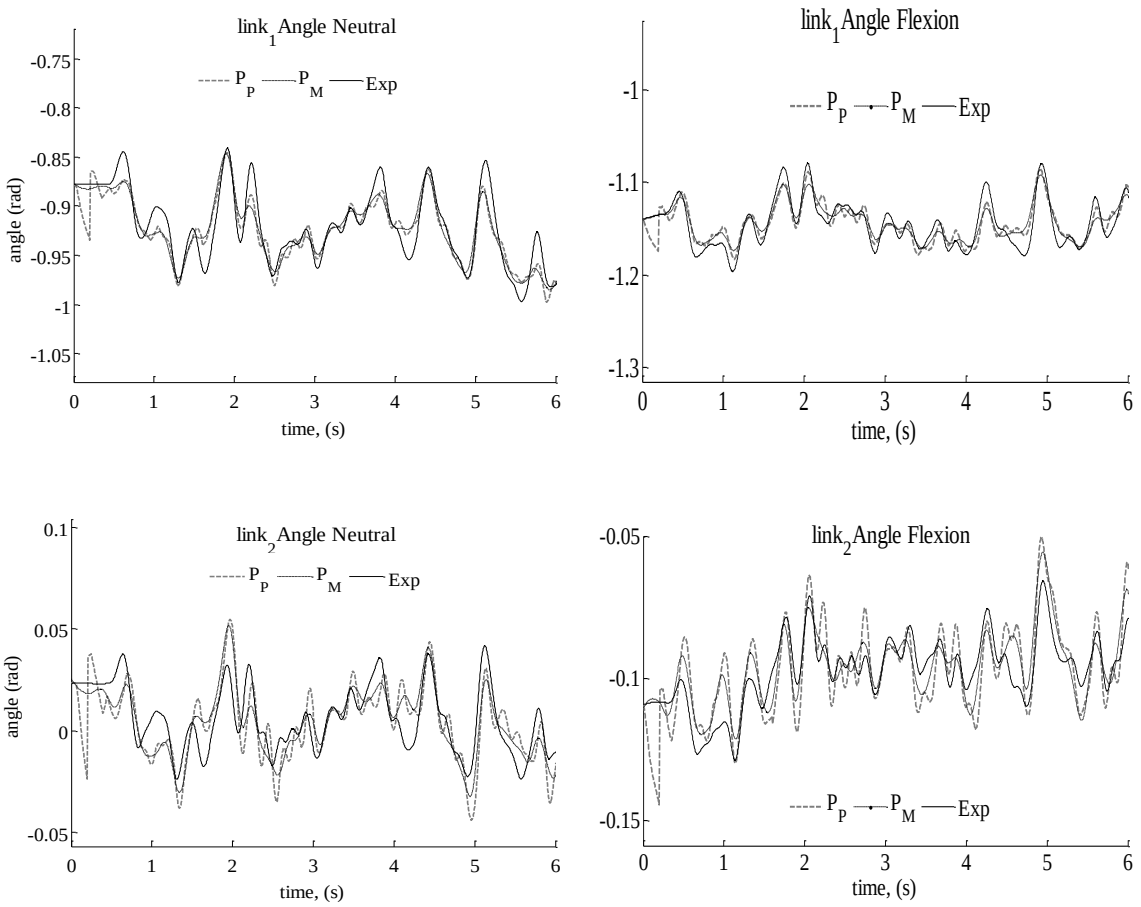

Figure 23: Angle with respect to neutral and flexion postures; P_P is the passive skeletal model (dashed line), P_M is the muscle-based model (dotted line), and Exp (continuous gray line).

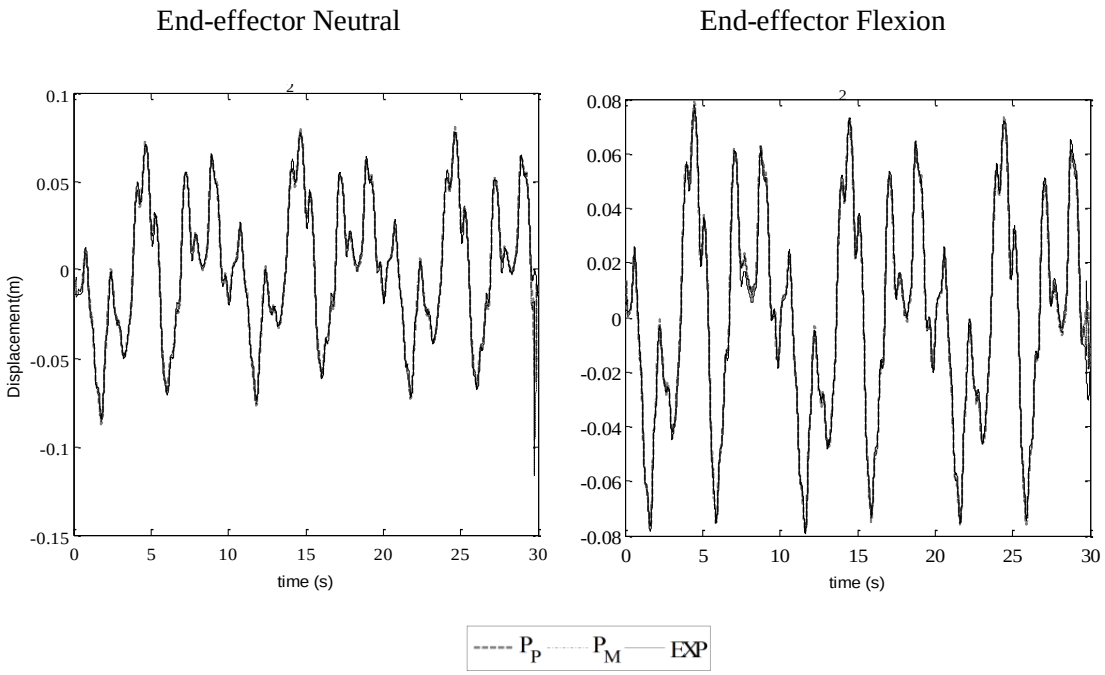

Figure 24: End-effector displacement in the x direction in the time domain

2.7 Discussion

When comparing the identified parameters of the proposed human head-neck model with the literature, it appears that they are relatively similar. The research of Fard, Ishihara et al. (2004) indicated that K_b=8-14 Nm/rad and C_b=0.29-0.53 Nms/rad, which is identical to the results of this work with (K_b =9.14 Nm/rad and C_b=0.36 Nms/rad).

The data used in the parameter identification of the model were based on data from the geometrical mean of individuals who have different anthropometries. Therefore, for subject-specific response, it is expected that the model will generate some errors as a result of these differences in the anthropometrical data.

Also, in this work, the passive and muscle-based models were based on a linearized mode of the equation of motion; therefore, it is expected that the model will generate some errors for large angular displacement. In the current work, the maximum

angle for each direction was less than 6 degree, except for one subject with an angle around 11 degree.

Finally, the proposed head-neck models are planar models, which can only simulate two postures: neutral and flexion. However, when it comes to other postures and motion, such as lateral bending or lateral rotation around the z-axis, the proposed models in this chapter will not able to simulate such postures. Thus, generalized 3D models are needed and will be discussed in the next chapter.

CHAPTER III

THREE-DIMENSIONAL HUMAN NECK AND HEAD SYSTEM MODELING AND SIMULATION

3.1 Introduction

The objective of this work is to develop human head-neck models with the capability of predicting the head-neck biodynamic response under fore-aft and combined-axis WBV when the person takes different head-neck postures. Experimental data were acquired from human subjects and were used in the frequency domain to characterize the stiffness and damping properties of the head-neck region.

This chapter is organized into five sections as follows. After the introduction, Section 3.2 presents the methodology. In this section, the experiments are introduced, including the participants, the experimental conditions, and the biodynamic measures. After the methodology, the head-neck models and the passive and muscle-based models are introduced in Section 3.3. The models are the 3D passive model and the muscle-based model. The passive model is a one-link model with 3 DOFs. For the muscle-based model, additional muscle components are added to the passive model to simulate the muscle activities. The results of the two models compared with experimental testing are demonstrated in Section 3.4. Section 3.5 is the conclusion and discussion section.

3.2 Methodology

3.2.1 Participants

Six healthy male subjects participated in this study. They had height of 178.8 ± 10 cm and weight of 75.18 ± 12.9 kg, as shown in Table 8. Subjects reported no prior neck, shoulder, or head injuries, nor any neurological conditions. Written informed consent, as approved by the University of Iowa IRB, was obtained prior to testing. Subjects were seated in an uncushioned, rigid seat mounted to a vibration platform. The data from the

first four subjects were used in system parameter identification; the data from the fifth and sixth subjects were used in the model validation.

Table 8: DH table for 3D head-neck vibration.

Basic Information about 5 subjects (3D)		
Subject	Height(m)	Weight(Kg)
1	1.89	90.7
2	1.77	71.0
3	1.72	65.6
4	1.78	86.3
5	1.78	62.3
average	1.788	75.182

3.2.2 Experiments

A 12-camera Vicon system (infrared SVcam cameras with a resolution of 0.3 megapixels per frame and a peak capture rate of 200 Hz) was used to collect position data of passive reflective markers. Sixteen reflective markers were attached to the subject's skin (Figure 5a-b). The markers on the head were placed just superior and lateral to each eyebrow, as well as on each side of the back of the head. For the neck, three markers were placed on C_7-T_1, three markers were placed on C_4-C_5, and one marker was placed on each side at C_1-C_2. Additional markers and accelerometers were placed on the rigid platform to measure the input vibration to the system. The finite difference method was used to calculate the velocity and acceleration from the position-based markers (Rahmatalla and DeShaw, 2011a). Input vibration was generated using a six-DOF man-rated vibration platform (Moog-FCS, Ann Arbor, MI, USA). Experiments were conducted where the subjects sat with their backs leaning and strapped to the seatback and their arms on their laps (Figure 26a-c). Subjects were exposed to white-noise random fore-aft and multiple-axis vibration signals with frequency range of 0.5-10 Hz and unweighted vibration magnitude of 1.0 m/s^2 RMS at the rigid-platform level. Each file

ran for 30 seconds. The subjects were instructed to relax and take four different postures: neutral, flexion, lateral flexion, and lateral rotation (Figure 26c-f). The postures were maintained during the experiments by instructing the subjects to look at fixed pictures on the walls of the lab.

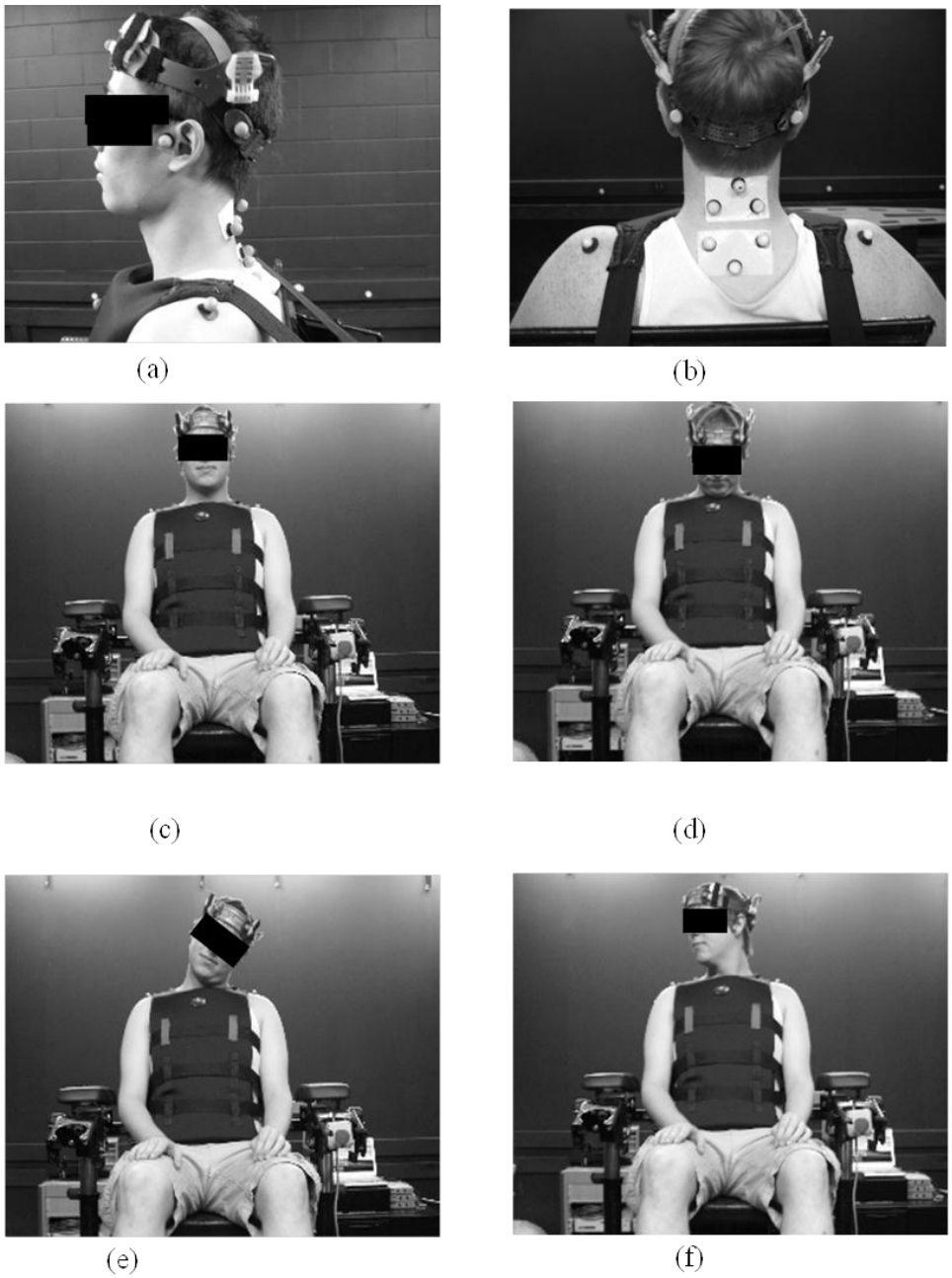

Figure 25: Marker protocol and subject seated-postures during testing. (a) side view of marker locations on the head and neck, (b) back view of marker locations on the head and neck, (c) neutral posture, (d) flexion posture, (e) lateral flexion posture, (f) later

3.2.3 Biodynamic Measures

The head-neck transfer function for a participant $\mathbf{H}(f)$ is defined in this work as the complex ratio between the output angular acceleration of the head-neck and the input horizontal acceleration measured at C_7. To calculate $\mathbf{H}(f)$ for a population, the geometric mean of the transfer function (Eq. (3.1)) is used instead of the arithmetic mean to describe the general dynamic response of the head-neck. The geometric mean (H_g) reduces the effects of the noise corruption and gives an unbiased estimation of the transfer function more effectively than does the arithmetic mean (Schoukens and Pintelon, 1990).

$$H_{ij}^{g}(f) = \prod_{k=1}^{n} \sqrt[n]{\left[H_{ij}(f)\right]_k} \tag{3. 1}$$

where *k* is a counter and *n* is the number of subjects.

For a multi-input and multi-output (MIMO) system, the transfer function $H_{ij}(f)$ is defined as the ratio between the input cross-spectra $G_{X_iX_j}$ and the input/output cross-spectra $G_{X_iY_j}$, where X_i and X_j are the input acceleration in the directions *i* =1, 2, 3 and *j* = 1, 2, 3 and Y_j is the output angular acceleration.

$$\mathbf{H}(f) = \begin{bmatrix} G_{X_1X_1} & G_{X_1X_2} & G_{X_1X_3} \\ G_{X_2X_1} & G_{X_2X_2} & G_{X_2X_3} \\ G_{X_3X_1} & G_{X_3X_2} & G_{X_3X_3} \end{bmatrix}^{-1} \begin{bmatrix} G_{X_1Y_1} & G_{X_1Y_2} & G_{X_1Y_3} \\ G_{X_2Y_1} & G_{X_2Y_2} & G_{X_2Y_3} \\ G_{X_3Y_1} & G_{X_3Y_2} & G_{X_3Y_3]} \end{bmatrix} \tag{3. 2}$$

$$\mathbf{H}(f) = \begin{bmatrix} H_{11} & H_{12} & H_{13} \\ H_{21} & H_{22} & H_{23} \\ H_{31} & H_{32} & H_{33} \end{bmatrix} \tag{3. 3}$$

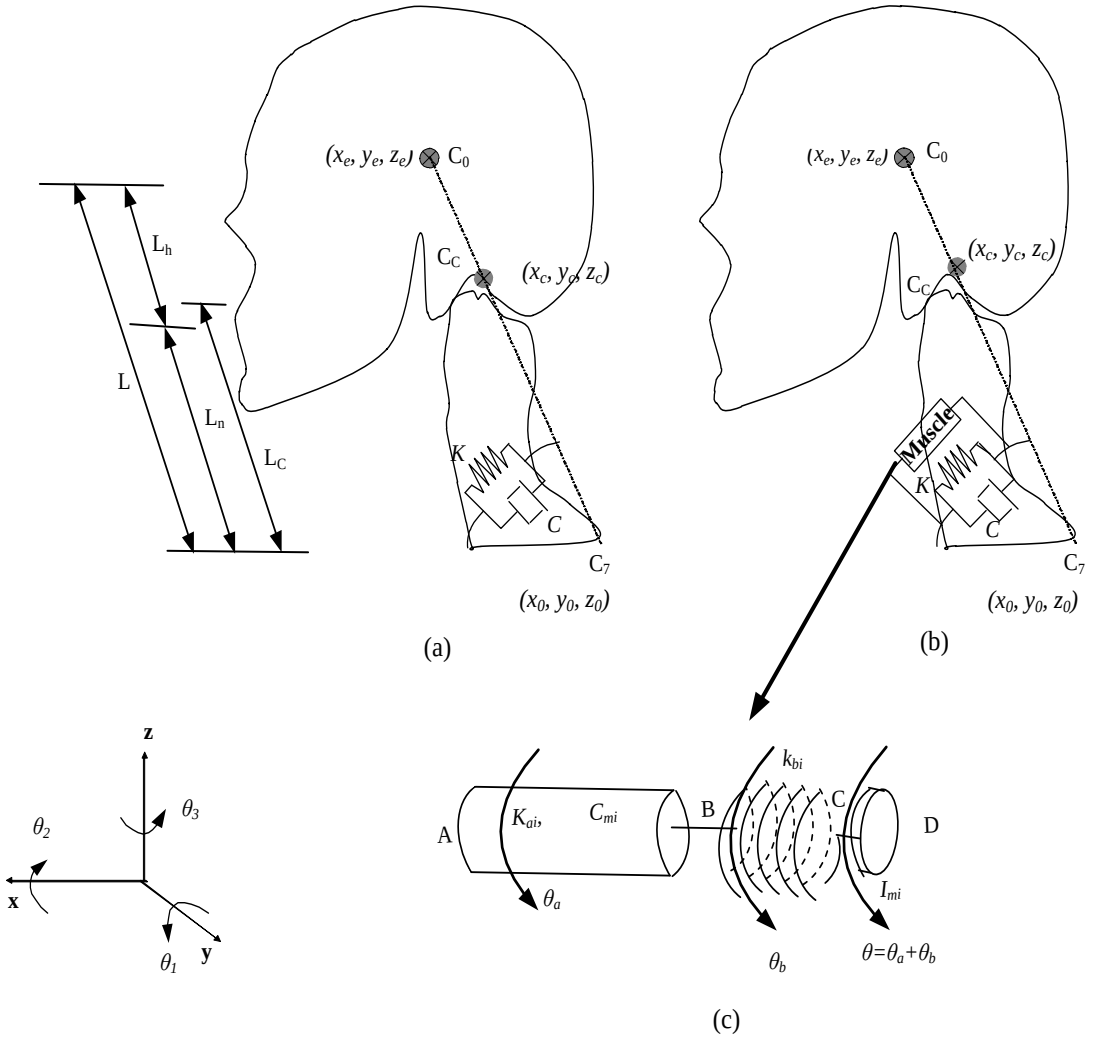

Figure 26: Components of passive and muscle-based models. In the coordinate system, z represents the vertical direction, x represents fore-aft direction, and y represents lateral direction; $\theta_1, \theta_2,$ and θ_3 represent flexion, lateral flexion, and lateral rotation respectively; (a) passive model comprising a spring K and damper C elements. C0 is location of center of head, CC is location of center of head-neck, and C7 is location of head-neck joint. L_n is length of neck, L_h is length of head, L is total length of head-neck, and L_c is length between CC and C7; (b) muscle-based model comprising passive elements K and C and a muscle component; (c) elements of muscle component, AB simulating contractile part of muscle represented by a stiffness element K_{ai} and a damping element C_{ai}, in which $i = 1,2,$ and 3 representing angular resistance of muscle in the $\theta_1, \theta_2,$ and θ_3 directions, BD simulating passive tissue-like component of muscle represented by a stiffness element K_{bi} and a damping element C_{bi}, in which $i = 1,2,$ and 3 representing angular resistance of muscle in the $\theta_1, \theta_2,$ and θ_3 directions, and CD simulating inertia component of muscle represented by I_{mi}.

3.3 Head-Neck Models

Two head-neck models are proposed in this study. The first is a passive model (Figure 26a), which comprises a rigid-link dynamic system with the connective tissue represented by springs and dampers (Winter, 2005). The second is a muscle-based model, which is similar to the passive model but has additional muscle components as shown in Figure 26b. The passive model will be demonstrated in detail in Section 3.3.1, and the muscle-based model will be presented in Section 3.3.2.

3.3.1 Passive Model

The proposed head-neck passive model is an inverted pendulum (Figure 26a, representing the area between the center of the head (C_0) and C_7. The joint at C_7 has three rotational DOF, including the flexion/extension angle about the y-axis (θ_1), the lateral abduction/adduction angle about the x-axis (θ_2), and the lateral rotation angle about the vertical z-axis (θ_3). The rotational angles (θ_1, θ_2, θ_3) are calculated from the translational motion using the DH method (Denavit and Hartenberg, 1955), and the DH table is shown in Table 8. The input random linear acceleration signal is applied at C_7 at coordinate $\mathbf{x}_0 = (x_0(t), y_0(t), z_0(t))^T$. C_0 is located at coordinates $\mathbf{x}_e = (x_e(t), y_e(t), z_e(t))^T$. The center of the head-neck C_C is located at $(x_c(t), y_c(t), z_c(t))^T$. Linear rotational damper elements with damping coefficients c_{ij} ($i = 1, 2,$ and 3) and linear rotational spring elements with spring factors k_{ij} ($I = 1, 2,$ and 3) representing the passive resistance of the connective tissues are attached to the joint at C_7. $\boldsymbol{C}$ shown in Eq. (3. 4) and $\boldsymbol{K}$ shown in Eq. (3. 5) are full matrices; i.e., the out-of-diagonal components in $\boldsymbol{C}$ and $\boldsymbol{K}$ are not zero (Panjabi et al., 1976).

$$\mathbf{C} = \begin{bmatrix} c_{11} & c_{12} & c_{13} \\ c_{12} & c_{22} & c_{23} \\ c_{13} & c_{23} & c_{33} \end{bmatrix} \tag{3. 4}$$

$$\mathbf{K} = \begin{bmatrix} k_{11} & k_{12} & k_{13} \\ k_{12} & k_{22} & k_{23} \\ k_{13} & k_{23} & k_{33} \end{bmatrix} \tag{3. 5}$$

L_n in Figure26a is the length of the neck, L_h is the length of the head, $L_c = (m_n \times L_n + m_h \times L_h)/m$, and L is the length between C_0 and C_7. The mass of the head-neck is $m = m_h + m_n$, where m_h is the mass of the head and m_n is the mass of the neck. The mass of the head-neck of each participant is estimated based on the participant's anthropometry (Winter, 1979, 2005; Dempster and Gaughran, 1967; de Leva 1996). For the neck, the moment of inertia is estimated base on the inertia of seven cervical vertebrae, $I_{11} = \sum_{j=1}^{7} i_{x,j} + m_j {\rho_{x,j}}^2$, $I_{22} = \sum_{j=1}^{7} i_{y,j} + m_j {\rho_{y,j}}^2$ and $I_{33} = \sum_{j=1}^{7} i_{z,j}$, where $i_{x,j}$ $i_{y,j}$ $i_{z,j}$ are the inertia of the j^{th} cervical vertebrae (Himmetoglu et al., 2007) and $\rho_{x,j}$ and $\rho_{y,j}$is the distance from the center of the vertebrae to C_7 in the x and y direction and can be adjusted based on the literature (Himmetoglu et al, 2007; Dempster and Gaughran, 1967). For the second segment, head, I_{ii} (*i=1,2,* and *3*) can be adjusted directly based on previous research (Himmetoglu., et al, 2007; Winter, 1979, 2005; Dempster and Gaughran,1967).

The dynamic equation for the passive model is derived by Lagrange's equation as shown in Eq. (3.6) and Eq. (3.7).

$$\frac{d}{dt}\left(\frac{\partial L}{\partial \dot{\Phi}}\right) - \frac{\partial L}{\partial \Phi} + \frac{\partial D}{\partial \dot{\Phi}} = 0 \tag{3. 6}$$

$$Lar = T - V \tag{3. 7}$$

where *Lar* is the Lagrangian equation.

$$T = \frac{1}{2} m \vec{\boldsymbol{v}}(t) \cdot \vec{\boldsymbol{v}}(t) + \frac{1}{2} \dot{\boldsymbol{\theta}}(t)^T \mathbf{I} \dot{\boldsymbol{\theta}}(t) \tag{3. 8}$$

T is the kinetic energy (Eq. (3.14)) $\vec{\boldsymbol{v}}(t) = [v_x(t), v_y(t), v_z(t)]^T$, $\dot{\boldsymbol{\theta}}(t) = [\dot{\theta}_1(t), \dot{\theta}_2(t), \dot{\theta}_3(t)]^{\mathrm{T}}$, and $\mathbf{I} = diag(I_{11},\ I_{22},\ I_{33})$.

$$V = mgz_c(t) + \frac{1}{2} \boldsymbol{\theta}(t)^T\ \boldsymbol{K} \boldsymbol{\theta}(t) \tag{3. 9}$$

where V is the potential energy, $z_c(t)$ is the vertical distance of C_C from the coordinate system, $\boldsymbol{\theta}(t) = (\theta_1(t), \theta_2(t), \theta_3(t))^T$, and $\theta(t)$ is the angle of rotation from the

equilibrium position θ_o where $\boldsymbol{\theta_o} = \{\theta_{10}, \theta_{20}, \theta_{30}\}^T$ is the initial static equilibrium postural angle for the flexion, lateral flexion, and lateral rotations, respectively.

$$D = \frac{1}{2}\dot{\boldsymbol{\theta}}(t)^T \mathbf{C}\dot{\boldsymbol{\theta}}(t) \tag{3. 10}$$

where D is the dissipation function representing the viscous energy (Eq. (3.10)).

The final dynamical equation for the passive model in the time domain is as follows:

$$\mathbf{I_s}\ddot{\boldsymbol{\theta}} + \mathbf{C_s}\dot{\boldsymbol{\theta}} + \mathbf{K_s}\boldsymbol{\theta} = \boldsymbol{\alpha}\ddot{\boldsymbol{x}}_{\mathbf{0}} \tag{3. 11}$$

where $\mathbf{I_s}$ is the inertia matrix of the HNS.

$$\mathbf{I_s} = \begin{bmatrix} LL_c m\cos^2\theta_{20} + I_{11} & 0 & -\frac{1}{2}L_c m\, L\cos\theta_{10}\sin(2\theta_{20}) \\ 0 & L_c mL + I_{22} & L_c mL\sin\theta_{10} \\ -\frac{1}{2}L_c m\, L\cos\theta_{10}\sin(2\theta_{20}) & L_c mL\sin\theta_{10} & b_{33} \end{bmatrix} \tag{3. 12}$$

where

$$b_{33} = \frac{3LL_c m}{4} - \frac{1}{4}\mathrm{mcos}(2\theta_{10})\, LL_c - \frac{1}{8}\mathrm{mcos}\big(2(\theta_{10} - \theta_{20})\big)\, LL_c - \frac{1}{4}\mathrm{mcos}(2\theta_{20})\, LL_c - \frac{1}{8}mcos(2(\theta_{10} + \theta_{20}))L_c L + I_{33}$$

$\mathbf{K_s}$ is the stiffness matrix of the head-neck.

$$\mathbf{K_s} = \begin{bmatrix} \frac{1}{2}(2k_{11} - 2gL_c m\cos\theta_{10}\cos(\theta_{20})) & \frac{1}{2}(2k_{12} + 2gL_c m\sin\theta_{10}\sin(\theta_{20})) & k_{13} \\ \frac{1}{2}(2k_{12} + 2gL_c m\sin\theta_{10}\sin(\theta_{20})) & \frac{1}{2}(2k_{22} - 2gL_c m\cos\theta_{10}\cos(\theta_{20})) & k_{23} \\ k_{13} & k_{23} & k_{33} \end{bmatrix} \tag{3. 13}$$

$\mathbf{C_s}$ is the damping matrix of the head-neck.

$$\mathbf{C} = \boldsymbol{C_s} \tag{3. 14}$$

$\boldsymbol{\alpha}$ is the matrix containing the geometrical information of the head-neck.

$$\boldsymbol{\alpha} = \begin{bmatrix} a_{lm}\cos\theta_{10}\cos\theta_{20}\cos\theta_{30} & a_{lm}\cos\theta_{10}\cos\theta_{20}\sin\theta_{30} & a_{lm}\cos\theta_{20}\sin\theta_{10} \\ -a_{lm}\cos\theta_{30}\sin\theta_{10}\sin\theta_{20} - a_{lm}\cos\theta_{20}\sin\theta_{30} & a_{lm}\sin\theta_{10}\sin\theta_{20}\sin\theta_{30} - a_{lm}\cos\theta_{20}\cos\theta_{30} & a_{lm}\cos\theta_{10}\sin\theta_{20} \\ -a_{lm}\cos\theta_{30}\sin\theta_{20} + Lm\cos\theta_{20}\sin\theta_{10}\sin\theta_{30} & a_{lm}\sin\theta_{20}\sin\theta_{30} - a_{lm}\cos\theta_{20}\cos\theta_{30}\sin\theta_{10} & 0 \end{bmatrix}$$

(3. 15)

where $a_{lm} = -L\,m + (L - L_h) \times \frac{m_n}{2}$.

$\ddot{\boldsymbol{x}}_{\boldsymbol{o}}(t) = (\ddot{x}_o(t), \ddot{y}_o(t), \ddot{z}_o(t))^T$ is the input acceleration at C_7, and $\ddot{\boldsymbol{\theta}}(t) = (\ddot{\theta}_1(t), \ddot{\theta}_2(t), \ddot{\theta}_3(t))^T$ is the output angular acceleration of the head-neck.

Transforming the dynamic equations from the time domain into the Laplace domain, the theoretical transfer function **H** between the input $\ddot{\boldsymbol{X}}_{\boldsymbol{0}}(s)$ and output $\ddot{\boldsymbol{\theta}}(s)$ is illustrated in Eq. (3.16).

$$\mathbf{H} = (\mathbf{I}_{\boldsymbol{s}} + \frac{\mathbf{C}_{\boldsymbol{s}}}{s} + \frac{\mathbf{K}_{\boldsymbol{s}}}{s^2})^{-1}\boldsymbol{\alpha} \tag{3. 16}$$

where $\ddot{\boldsymbol{X}}_{\boldsymbol{0}}(s)$ and $\ddot{\boldsymbol{\theta}}(s)$ are the Laplace transforms of $\ddot{\boldsymbol{x}}_{\boldsymbol{o}}(t)$ and $\ddot{\boldsymbol{\theta}}(t)$**,** respectively.

3.3.2 Muscle-based Model

The muscle-based model (Figure 26b) is based on the passive model (Figure 26a), with an extra muscle component (Figure 26c) that captures the extra muscle response. The muscle component comprises three parts. AB resembles the contractile muscle component (Winter, 2005; Chapman, 1983), which is modeled in this work as a resistive force, including a rotational linear damper (C_{mi}) and a spring (K_{ai}) parallel to each other; BC resembles the tissue-like elements represented by a series of elastic components, including a rotational linear spring (K_{bi}); and CD represents the inertia of the muscle (I_{mi}). The angle of rotation of AB in Figure 26c is θ_a; the angle of rotation of BC is θ_b; the angle of rotation of CD is $\theta = \theta_a + \theta_b$; $\dot{\theta}$, $\ddot{\theta}$ and $\dddot{\theta}$ represents the angular velocity, angular acceleration, and angular jerk, respectively.

The final dynamical equation for the muscle-based model in the time domain will take the following form:

$$\mathbf{I}_{\boldsymbol{s}}\ddot{\boldsymbol{\theta}} + \mathbf{C}_{\boldsymbol{s}}\dot{\boldsymbol{\theta}} + \mathbf{K}_{\boldsymbol{s}}\boldsymbol{\theta} = \boldsymbol{\alpha}\ddot{\boldsymbol{x}}_{\mathbf{0}} - \boldsymbol{M}_M \tag{3. 17}$$

where $\boldsymbol{M}_{\boldsymbol{M}}$ represents the muscle force component (Eq. (3.18)).

$$M_{Mi} = C_{mi}\left(\dot{\theta}_i - \frac{I_{mi}}{K_{bi}}\dddot{\theta}_i\right) + K_{ai}\left(\theta - \frac{I_{mi}}{K_{bi}}\ddot{\theta}_i\right)$$

$$= -C_{mi}\frac{I_{mi}}{K_{bi}}\ddot{\theta}_i - K_{ai}\frac{I_{mi}}{K_{bi}}\ddot{\theta}_i + C_{mi}\dot{\theta}_i + K_{ai}\theta_i$$

$$= -C_{mi}P_i\ddot{\theta}_i - K_{ai}P_i\ddot{\theta}_i + C_{mi}\dot{\theta}_i + K_{ai}\theta_i \quad (i = 1, 2, and\ 3) \tag{3. 18}$$

$\boldsymbol{M_M} = \{M_{M1}, M_{M2}, M_{M3}\}^T$, where M_{M1}, M_{M2} M_{M3} and represent the muscle torque in the θ_1, θ_2 and θ_3 directions, respectively, and $P_i = I_{mi} / K_{bi}$.

3.3.3 Parameters Identification

The subjects were exposed to fore-aft, $\ddot{x}_0$(t), and 3D $\ddot{x}_0$(t), $\ddot{y}_0$(t) and $\ddot{z}_0$(t) random input vibrations under four different postures (neutral, flexion, lateral flexion, and rotation). The data of the first four subjects with the rotational flexion posture under 3D input vibration were used in the identification of parameters for the stiffness $\boldsymbol{K}$ and damping $\boldsymbol{C}$ matrices. The rotation posture was chosen to put the HNS in a condition where most DOF are excited, which would help in characterizing the complex coupling between the head-neck parameters in different directions. The anthropometrical and response data of the fifth participant, under a new fore-aft random input vibration with the four postures, and the anthropometrical and response data of the sixth participant, under a new 3D random input vibration with the four postures, were used to validate the accuracy of the models.

The initial investigation of the experimental data indicated that the out-of-diagonal components of the geometric transfer function are significantly smaller than those of the diagonal components; therefore, they will not be considered in this work.

The system identification process proceeded as follows. First, ***H(f)*** of each participant was determined from the experimental data using Eq. (3.16). This was followed by calculating $\boldsymbol{H}^g(f)$ of the first nine participants using Eq. (3. 1). There are two steps in optimizing c_{ij} and k_{ij}. First, the frequency domain system identification is used to fit $\boldsymbol{H}^g(f)$ from the experimental data (Kollar, 2001; Fard, 2003a). The second step is to optimize k_{ij} and c_{ij} using the optimization scheme by MATLAB (Kollar, 2001;

Mathworks, 2010). The objective function (f^{obj}) shown in Eq. (3.19) represents the normalized differences between the predicted ($H_{ii}(f)$) and experimental ($H_{ii}{}^{g}(f)$) transmissibility's magnitude and phase, respectively.

$$f^{obj} = \sum_{i=1}^{3} \sum_{f} \left[\frac{(|H_{ii}(f)|-|H_{ii}{}^{g}(f)|)}{\||H_{ii}(f)|-|H_{ii}{}^{g}(f)|\|}\right]^2 + \left[\frac{(Pha(H_{ii}(f))-Pha(H_{ii}{}^{g}(f)))}{\|Pha(H_{ii}(f))-Pha(H_{ii}{}^{g}(f))\|}\right]^2 \quad (3.19)$$

where the independent variables are

$x = [k_{11}, k_{12}, k_{13}, k_{22}, k_{23}, k_{33}, c_{11}, c_{12}, c_{13}, c_{22}, c_{23}, c_{33}]^T$, the lower bound on the independent variables is [1, 1, 1, 1, 1, 1, -30, -30, -30, -30, -30, -30], the upper bound is [100, 100, 100, 100, 100, 100, 30, 30, 30, 30, 30, 30], and the converge tolerance is 1.0e-6 for all parameters.

For the muscle-based model, the passive parameters are similar to those of the passive model. The active parameters are identified as follows. First $\boldsymbol{M}_M$ is calculated from Eq. (3.17). This is followed by substituting $\boldsymbol{M}_M$ in Eq. (3.18). Equation (3.18) is then transformed to the frequency domain using FFT. Finally, the optimization scheme by MATLAB (Kollar 2001; Mathworks 2010) is used to find the muscle-based model parameters P_i, K_{ai}, and C_{mi}.

3.3.4 Solution Approach

In the solution approach for the passive model, the system outputs $\ddot{\boldsymbol{\Phi}}$, $\dot{\boldsymbol{\Phi}}$, and $\boldsymbol{\Phi}$ under a certain input motion $\ddot{\boldsymbol{X}}_{\boldsymbol{0}}(s)$ are calculated in the frequency domain using Eq. (3.20). The system outputs are then transformed to the time domain using the inverse Fourier transform. For the active model, Eq. (3.19) is used first to calculate $\boldsymbol{M}_{\boldsymbol{M}}$. This is followed by substituting $\boldsymbol{M}_{\boldsymbol{M}}$ in Eq. (3.18). $\ddot{\boldsymbol{\theta}}$, $\ddot{\boldsymbol{\theta}}, \dot{\boldsymbol{\theta}},$ and $\boldsymbol{\theta}$ are solved in the frequency domain based on the parameters from optimization and then are transformed to the time domain using the inverse Fourier transform.

3.4 Results

The results of the identification process of the passive components **K** (k_{ij}) and **C** (c_{ij}) are illustrated in Table 9. The muscle-based model parameters are illustrated in Table 10.

Figure 27 shows the predicted displacement of the passive and muscle-based model when compared with the response data of the sixth subject in fore-aft (x direction 1 input) WBV. It can be seen that the passive and the muscle-based models were able to capture the characteristics of the experimental displacement for the four postures—neutral, side, down, twist—with the muscle-based model being closer to the experiments. Similar characteristics were observed for the fifth subject under the 3D input motion, with the muscle-based model showing a trend closer to that of the experiments, as shown in Figure 28.

The accelerations of the muscle-based model of the sixth subject under fore-aft WBV (Figure 29) were closer to those of the experiments for all postures. The situation becomes harder to compare for the fifth subject under the combined 3D input vibration (Figure 30), where both models behaved more similarly; the muscle-based model, however, was closer to the experiments.

In WBV the interest is mostly in the system characteristics in the frequency domain. Figure 31 shows the PSD of the acceleration response of both models in comparison with the experimental data under fore-aft WBV of the sixth subject. Again, the muscle-based model showed characteristics closer to those of the experiments. For all postures, the signals showed considerable power for frequencies up to 4 Hz and negligible power after that.

As with the fore-aft input file, the PSD of the experiments and the models for all postures under the 3D files in Figure 31 showed little power after 4 Hz in the x and y directions, but showed observable energy between 4-6 Hz in the z direction.

Figure 33 shows the transmissibility of subject 6 under fore-aft WBV using both models and experimental data. It can be seen from the figure that the muscle-based model was closer to the experimental data for all posture. The transmissibility of subject 5 under multiple-axis WBV is demonstrated in Figure 34, where both models showed close agreement with the experimental data, with the muscle-based model showing a trend closer to the experiments when compared to that of the passive model.

Table 9: Stiffness and damper coefficient results for one-link 3D model (passive model)

Stiffness (Nm/rad)	k_{11}	k_{12}	k_{13}	k_{22}	k_{23}	k_{33}
	7.41	2.09	0.19	8.04	1.36	0.49
damper (Nms/rad)	c_{11}	c_{12}	c_{13}	c_{22}	c_{23}	c_{33}
	0.091	0.304	0.0785	0.780	0.272	-0.0491

Table 10: Muscle-based model parameters

Parameters	i=1	i=2	i=3
C_{mi}	0.0073	0.0621	0.1067
P_i	0.0560	0.0058	0.1084
K_{ai}	5.8598	2.5889	3.1404

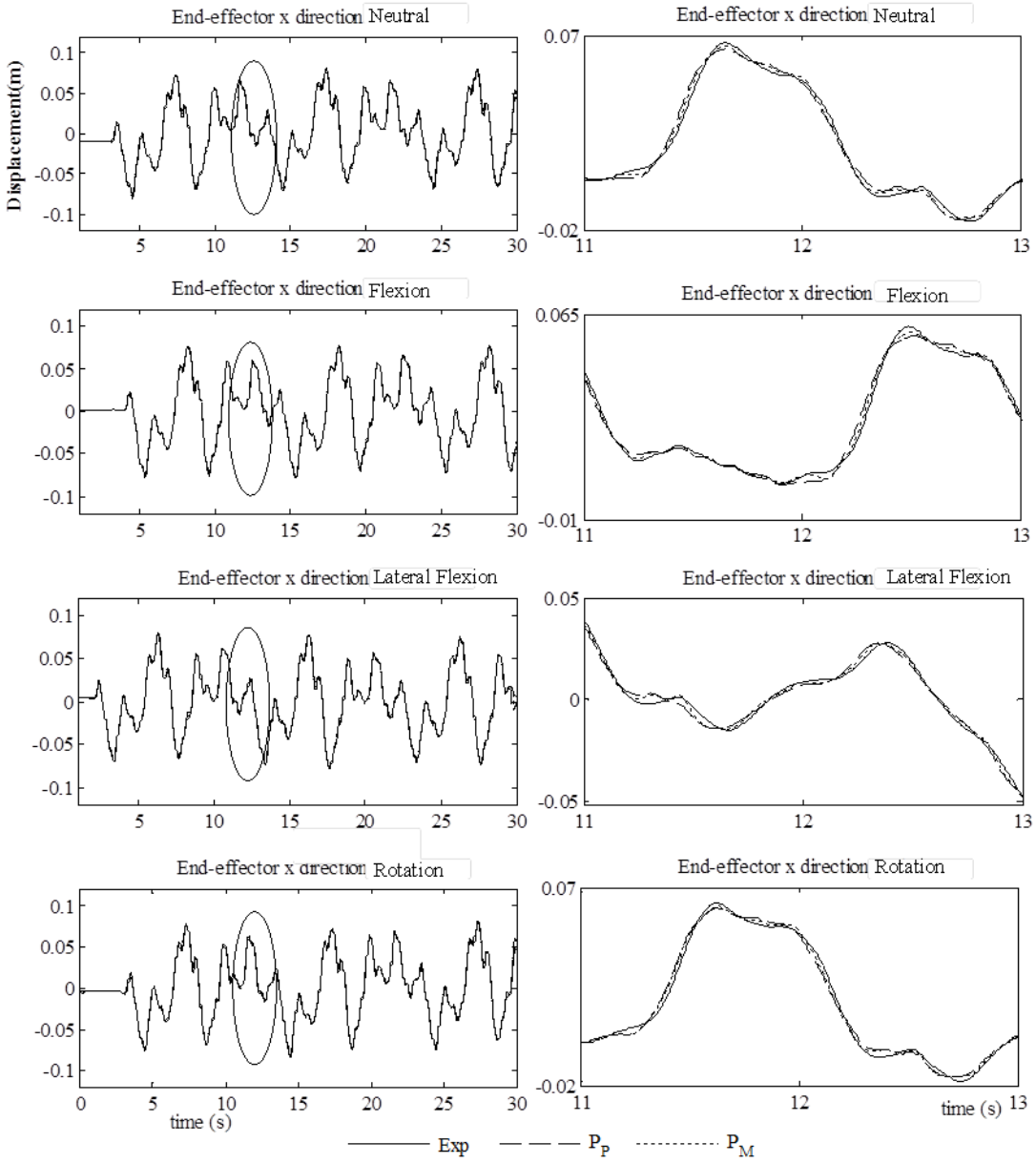

Figure 27: End-effector displacement results due to x direction input signal for the four postures (neutral, flexion, lateral flexion, and rotation). The figures in the left column are the end-effector figures in the time domain from 0-30 second; the figures in the right column are snapshots from 11-13 second.

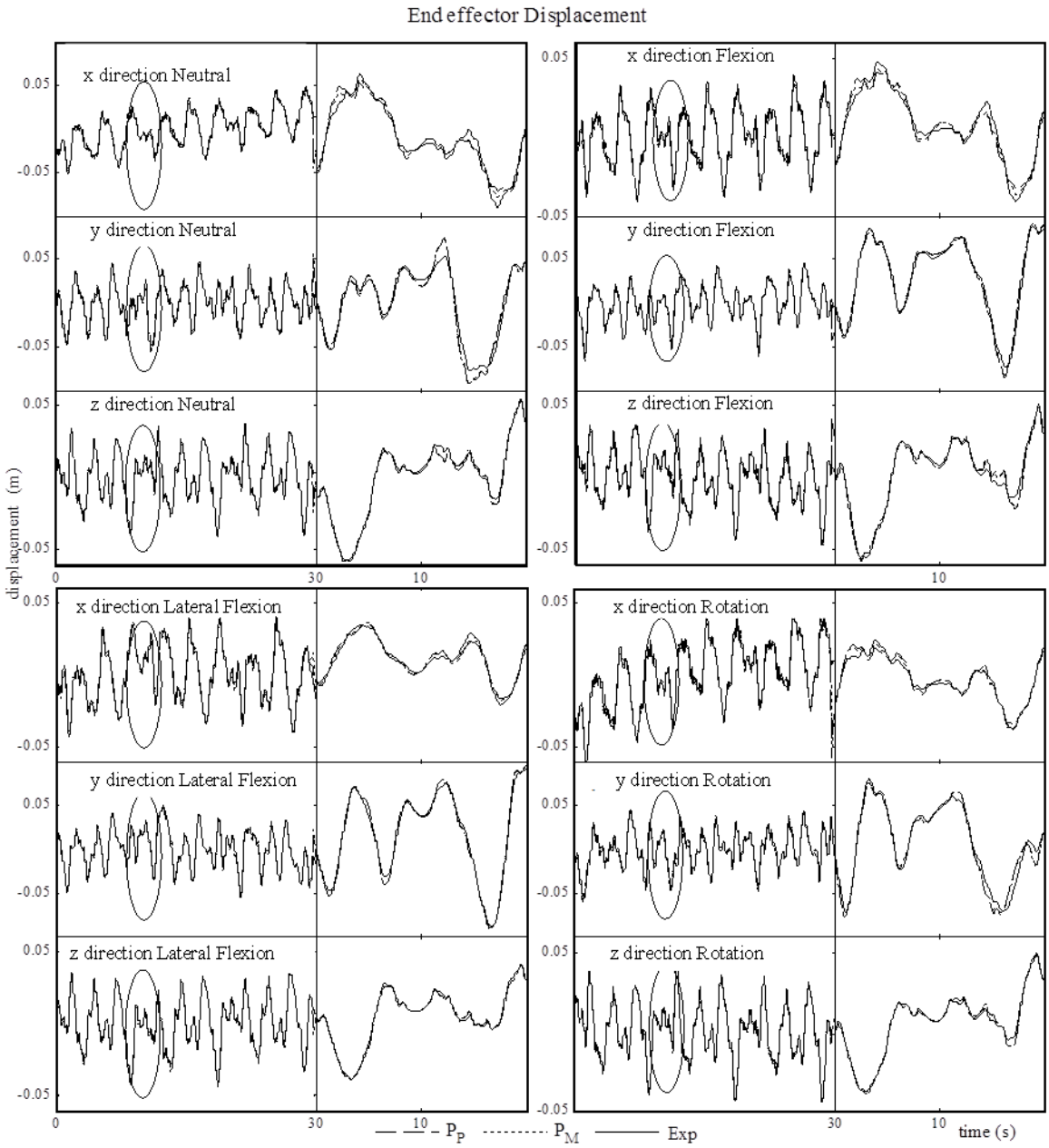

Figure 28: The 3 D head displacement due to 3 D inputs for the four postures (neutral, flexion, lateral flexion and rotation) in the time domain. The first and third columns are results from 0-30 second; the second and fourth columns are snapshots from 8 second.

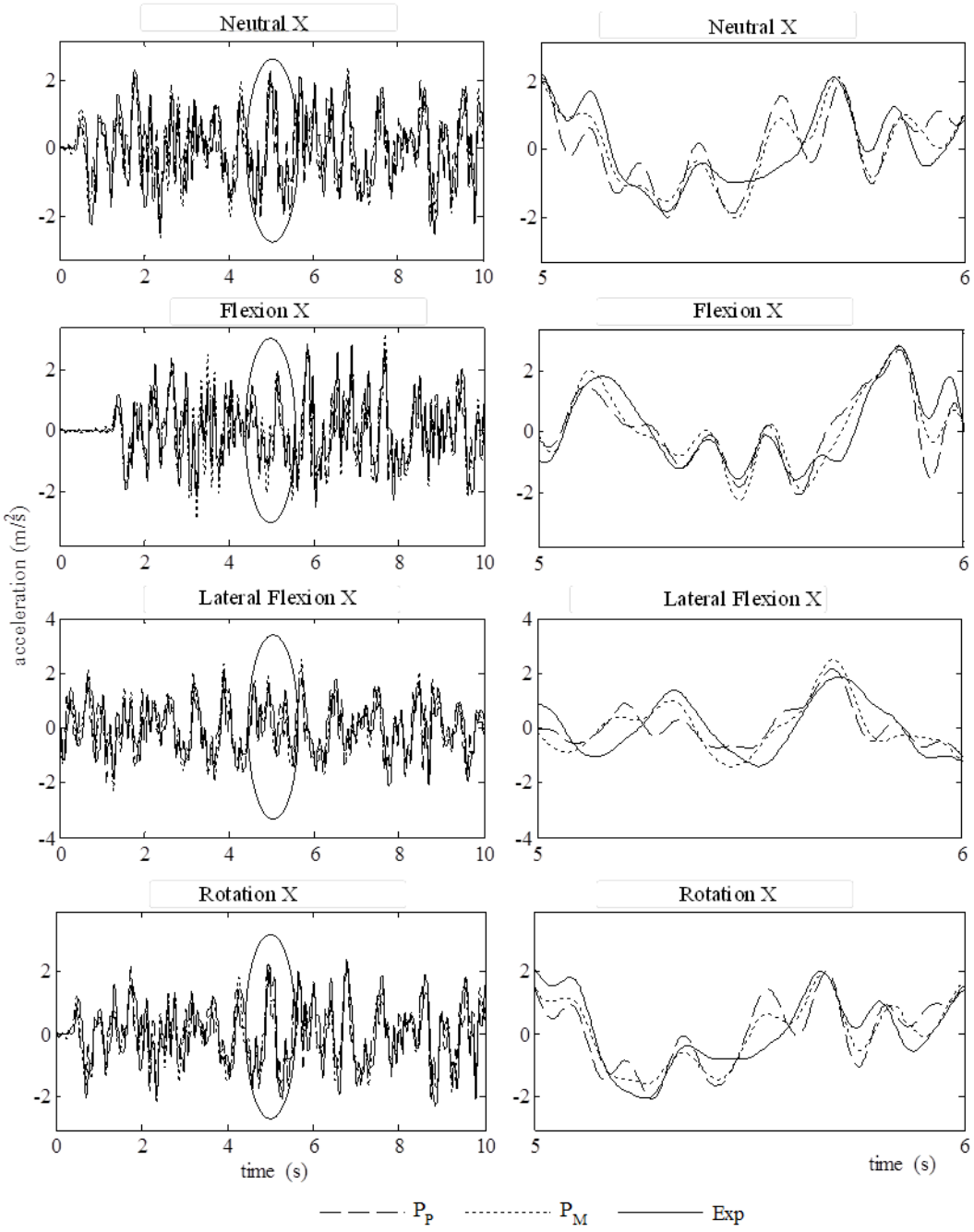

Figure 29: Head-neck response (fore-aft acceleration at center of the head C_0 level) in the time domain as results of input fore-aft acceleration at rigid-platform level for four different postures (neutral, flexion, lateral flexion, and lateral rotation). The figures in the left column are results from 0-10 second; the figures in the right column are snapshots from 5-6 second. P_p with dashed lines represents passive model, P_m with dotted lines represents muscle-based model, and E_{xp} with a solid line represents experiments.

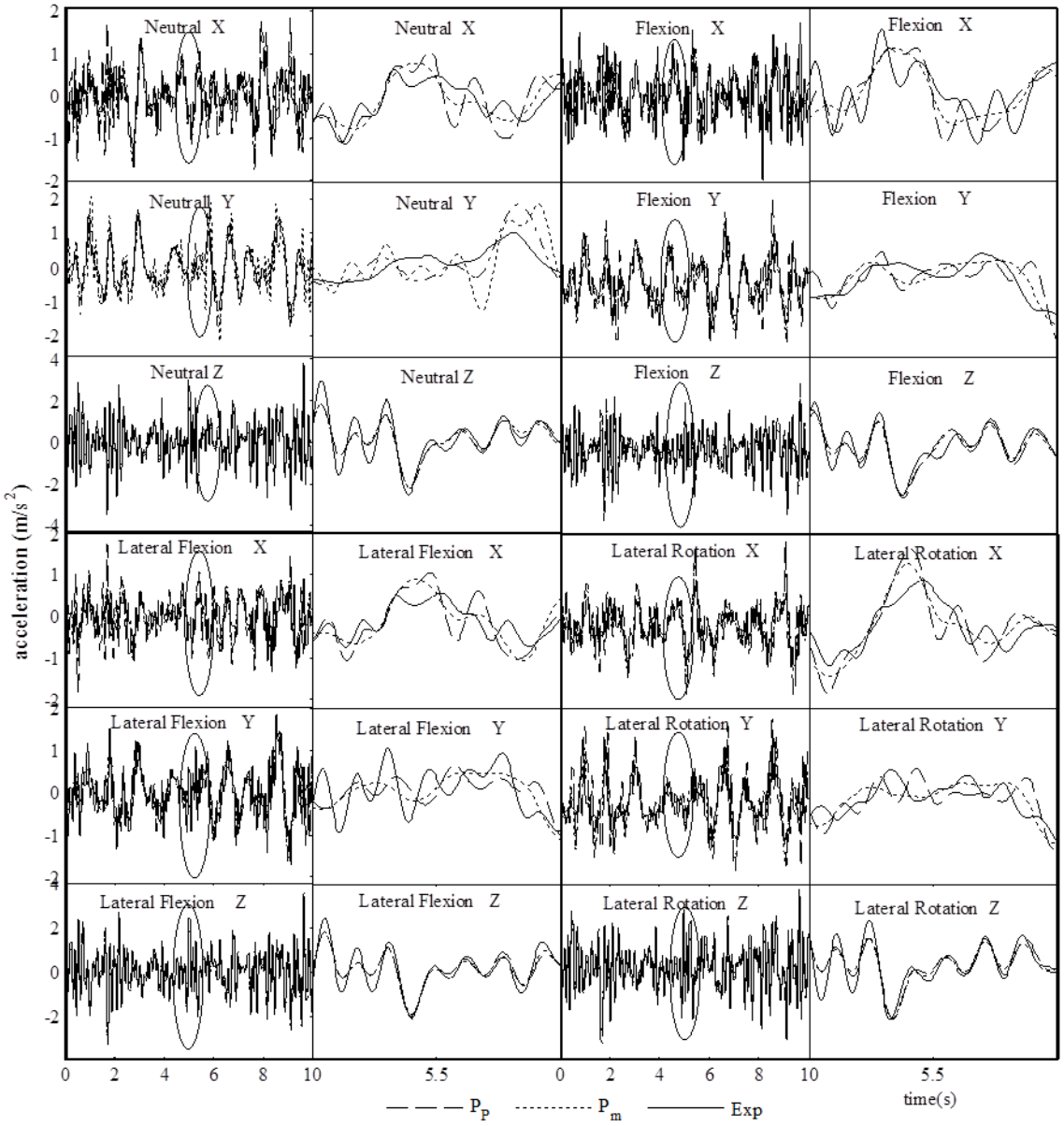

Figure 30: Head-neck response (3 D acceleration at center of the head C_0 level) in the time domain as results of input 3 D acceleration at rigid-platform level for four different postures (neutral, flexion, lateral flexion, and rotation). The first (left) and third columns are results from 0-10 sec; the second and fourth columns are snapshots between 2-4 second. P_p with dashed lines represents passive model, P_m with dotted lines represents muscle-based model, and Exp with a solid line represents experiments.

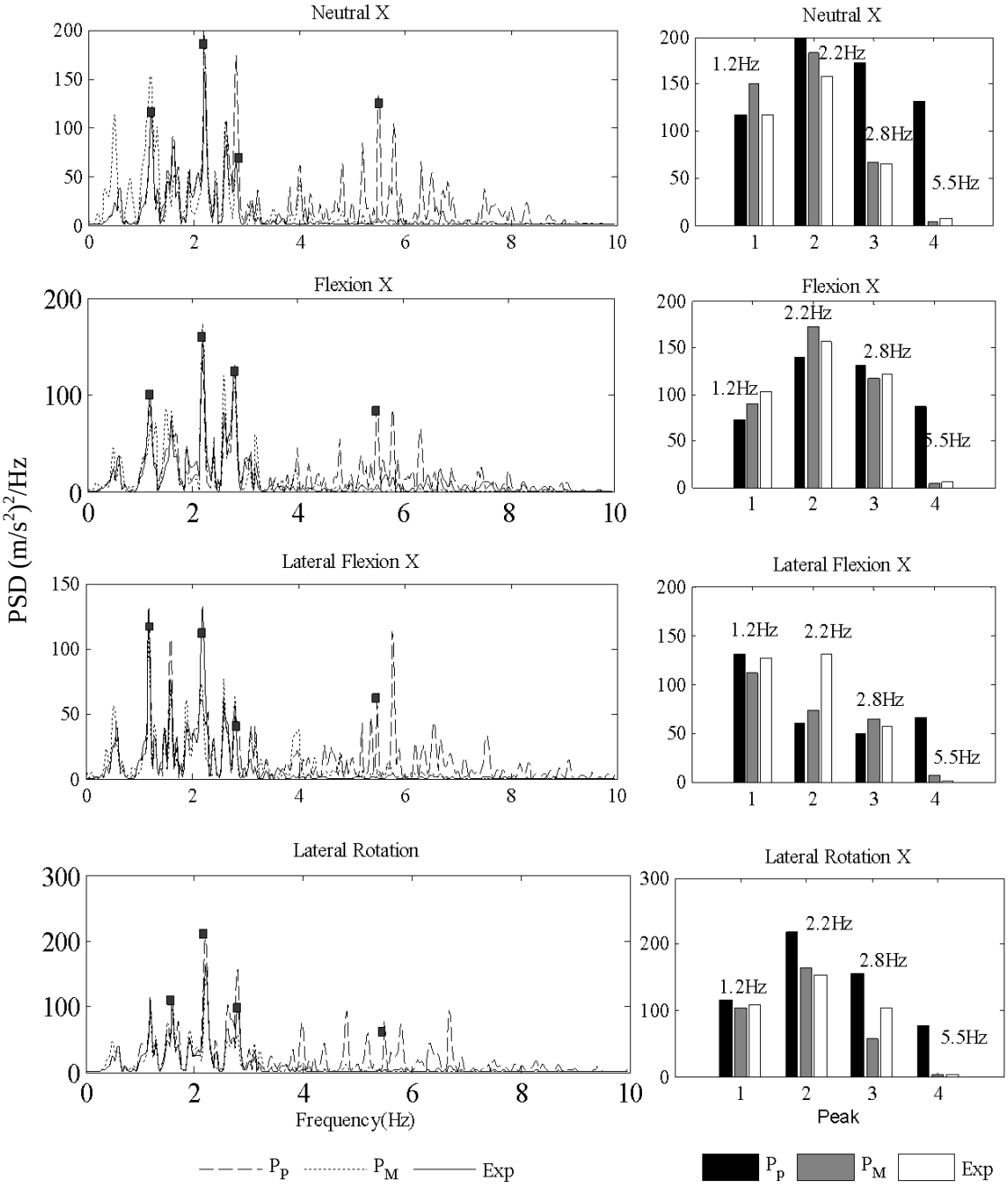

Figure 31: PSD for fore-aft input vibration with four different postures (neutral, flexion, lateral flexion, and lateral rotation). Figures in left column represent PSD from 0-10 Hz; figures in the right column are snapshots at critical zones. P_p with dashed lines represents passive model, P_m with dotted lines represents muscle-based model, and E_{xp} with a solid line represents experiments.

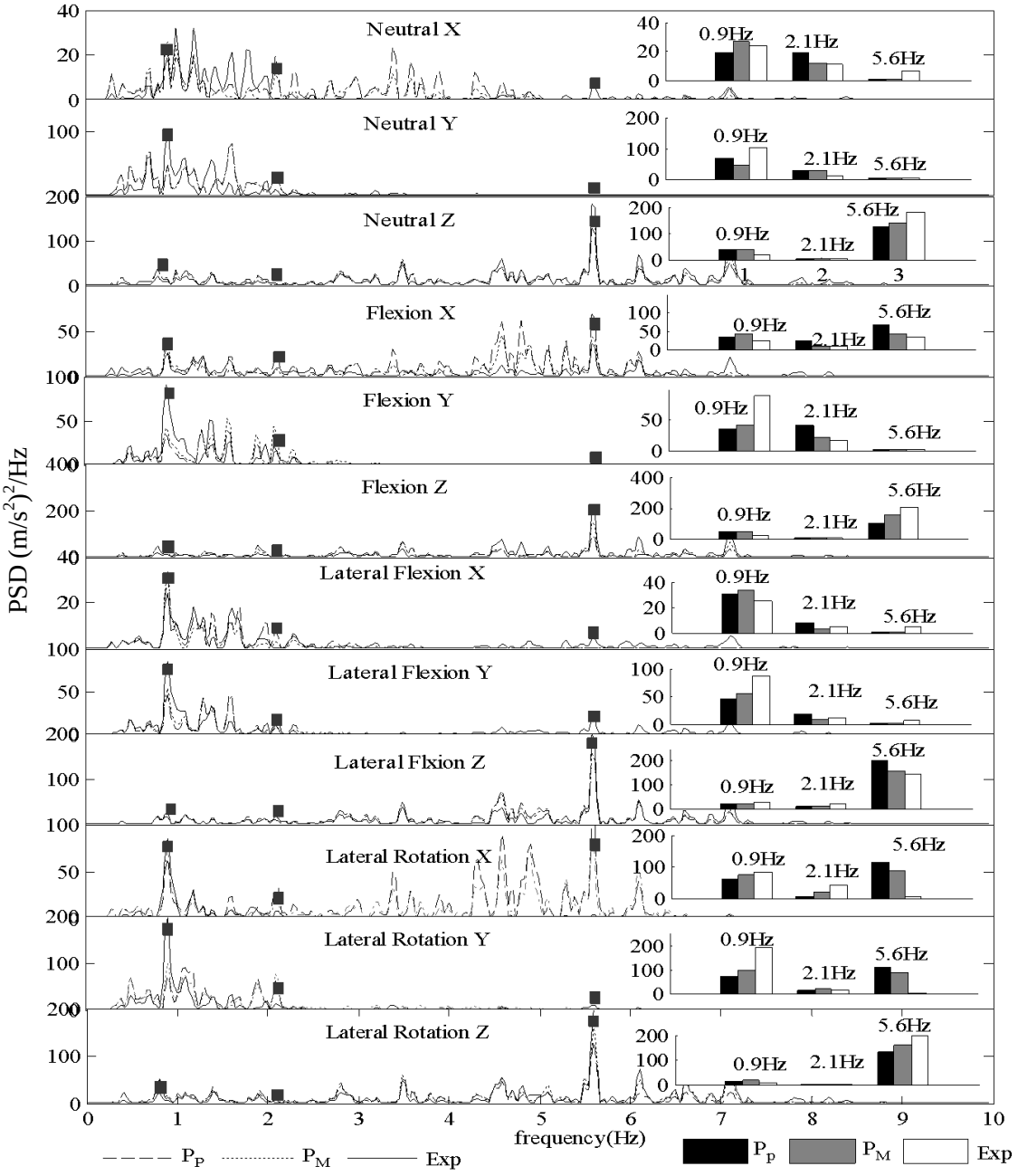

Figure 32: PSD for 3 D input vibration with four different postures (neutral, flexion, lateral flexion, and lateral rotation). Figures in left column represent PSD from 0-10 Hz; figures in the right column are snapshots at critical zones. P_p with dashed lines represents passive model, P_m with dotted lines represents muscle-based model, and E_{xp} with a solid line represents experiments.

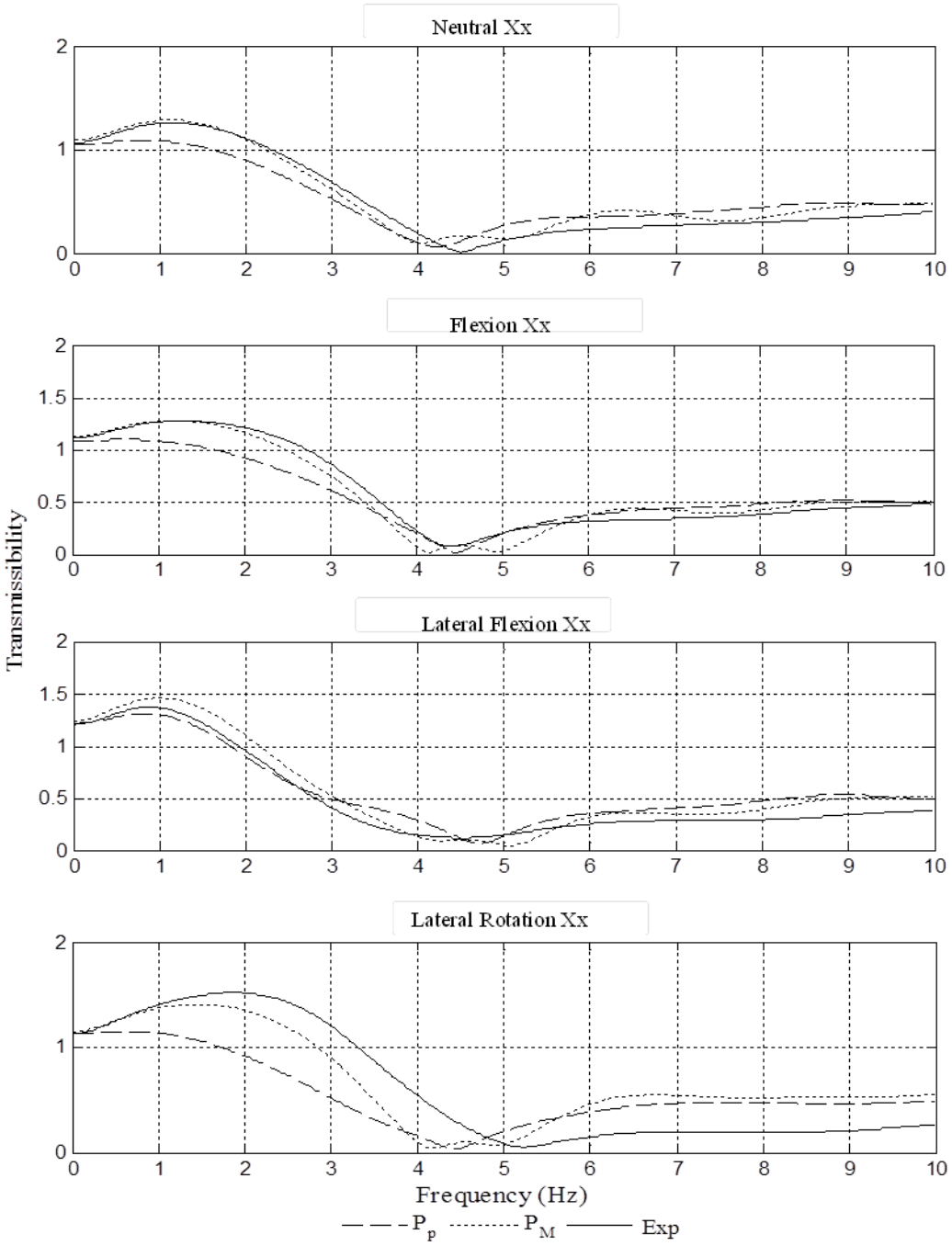

Figure 33: Magnitude of transmissibility of different postures. Input is x direction signal, and output is x direction end-effector.

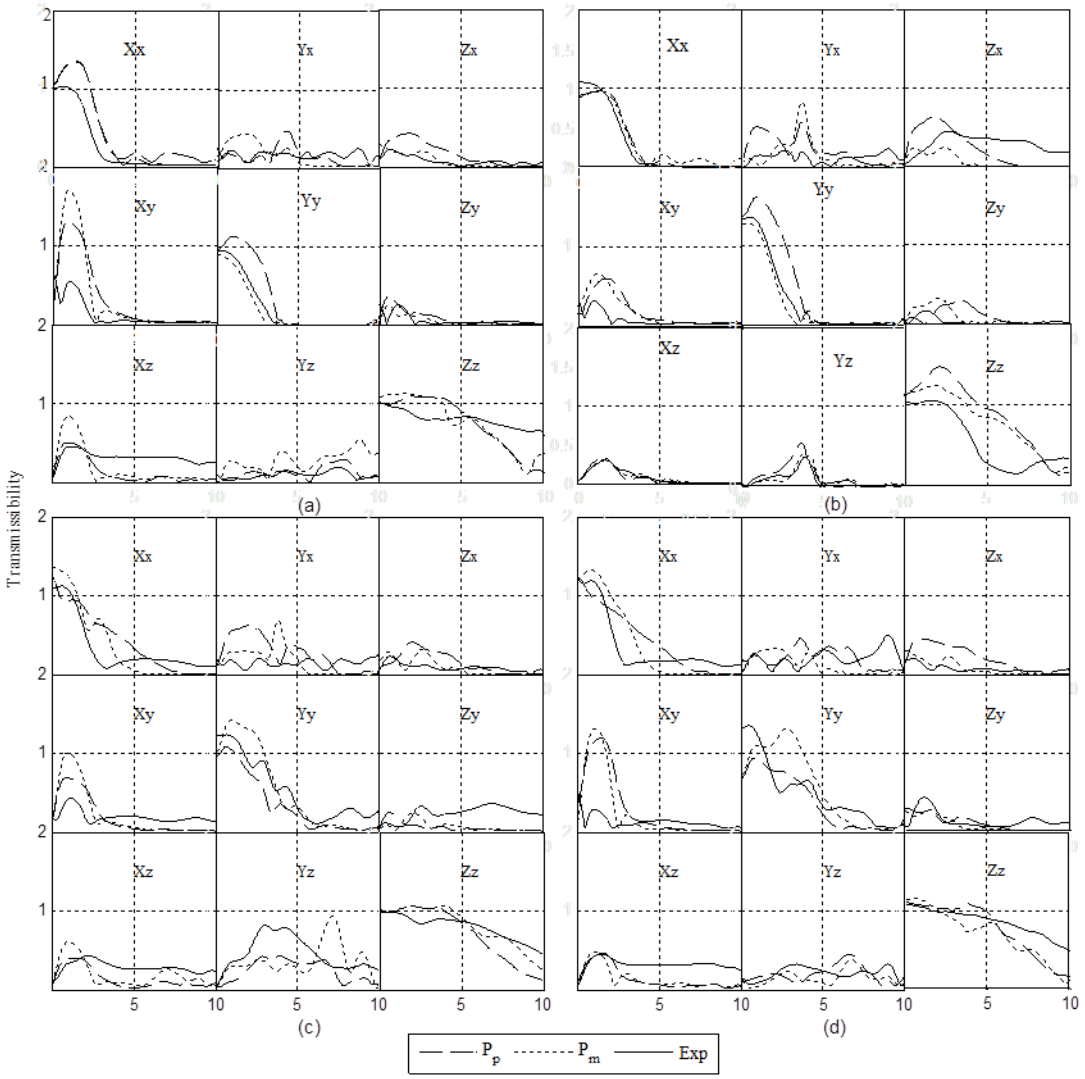

Figure 34: The magnitudes of transmissibility of different postures: (a) neutral, (b) flexion, (c) lateral flexion, and (d) rotation. The solid line is the experiment of subject 5. The center line (one dot and one dash) is the muscle model results. The dashed line is the skeletal.

3.5 Conclusions and Discussion

This work presents one-link passive and muscle-based models with the capability of predicting human head-neck motion under fore-aft and multiple-axis input vibration when the person is taking different postures. The results indicate that the passive and muscle-based models were able to reasonably predict the resulting motion of the HNS for

the postures under consideration; however, a model of the head-neck was improved in this work by taking muscle activity into account, which was consistent with the literature(Zadpoor and Nikooyan, 2010; Rahmatalla and Liu, 2012).

The results showed that the PSD for all postures under the combined-axis WBV have demonstrated high energy at frequencies lower than 5 Hz for the X and Y directions. This is consistent with the literature (Paddan and Griffin, 1998; Hinz, Menzel et al., 2010; Madakashira-Pranesh, 2011; Mandapuram, Rakheja et al., 2011), where the system resonates within this range of frequencies. In the Z direction, both models and experiments showed energy between 4-6 Hz, which is also consistent with the literature (Paddan and Griffin, 1998; Hinz, Menzel et al., 2010; Madakashira-Pranesh, 2011; Mandapuram, Rakheja et al., 2011). This could also indicate that the human HNS is acting like a low-pass filter in the X and Y directions, with the contribution of many muscles, and as a band filter in the Z direction.

The motion capture system provided the chance to measure the required DOF by using a small number of markers; however, experimental accelerations calculated from the motion capture data using the finite difference method are prone to error depending on system and environmental noise, skin movement, marker occlusions, and system resolution. While filtering is an option, this process is prone to windowing and is considered a limitation to the use of marker-based motion capture systems in WBV.

In this work, the lateral rotation posture under multiple-axis vibration was solely selected for the identification of the model parameters with the assumption that this posture would activate most of the head-neck parameters. Although the models were able to predict reasonable motion under different postures and vibration conditions with this assumption, using all postures in the parameter identification may introduce better results. Also, while this study presented simplistic forms of head-neck models that might not be able to explain the various aspects of the complexity of the HNS, the muscle-based model has the potential to be used in conjunction with existing kinematics-driven detailed-

muscle models (Pankoke, Hofmann et al., 2001; Bazrgari, Shirazi-Adl et al., 2008; Wang, Bazrgari et al., 2010) to investigate muscle forces and the physiological and pathological implications of postures in WBV scenarios.

One limitation of the proposed models is that it does not consider the effect of wobbling masses, such as the internal organs and soft tissues (Yue and Mester, 2002; Bazrgari, Nussbaum et al., 2010; Nikooyan and Zadpoor, 2011), on the response of the HNS. For the head-neck region, however, it is expected that the wobbling masses may have smaller effects than they do on the trunk and the lower extremities. Also, wobbling masses seem to be more affected by impact (Bazrgari, Nussbaum et al., 2010) than by the vibration encountered in this work. Another limitation of the models is the linearization of the equation of motion around the initial posture, which makes the predictability of the model under large rotation questionable. In this work, the range of the rotation angles around the initial postures was found to be around 3-6 deg. One final limitation is that the model parameters in this article were identified under one vibration magnitude condition, so the capacity of the models to capture nonlinearity under different vibration magnitudes is not discussed.

Finally, the head-neck models including the 2 D model (Chapter 2) and 3 D model are parts of the human body instead of the whole human body. There are two reasons. Firstly, in this study, our goal is to predict the head-neck response of WBV in seated position. We do not need extra human body parts to get extra results because the head-neck complex model is good enough to provide accurate results. Secondly, and most important, during experiments, all subjects' torsos were fixed to the seatback by a waist seatbelt and a six-strip vest as shown in Figures 4 and 5. It is assumed that the random signal is applied to the bottom of the neck (C_7). However, there is a certain interaction between the torso and neck. That part is ignored in this research.

CHAPTER IV

BIODYNAMIC RESPONSE OF THE SUPINE HUMAN BODY DURING WHOLE–BODY VIBRATION IN THE SAGITTAL PLANE

4.1 Introduction

The objective of this chapter is to introduce supine-human models and their transportation systems under WBV, such as those involved in ground and aerial transportation in the sagittal plane. There are five sections in this chapter. Section 4.1 is the introduction. Then, experimental conditions and set-up are introduced in Section 4.2. The biodynamic measurements of the experiments and the frequency domain experimental results are also shown in this section. In the main section, Section 4.3, a 6-DOF supine model is first explained as the primary model in Section 4.3.1. Then, in Section 4.3.2, the secondary model, which is a litter-board model, is proposed. The results of the two conditions compared with the experimental results in both the time and frequency domain are illustrated in Section 4.4. The final section is the discussion.

4.2 Methods

4.2.1 Participants

Eight healthy male subjects participated in this study. The participants had a mean age of 23 ± 3.16 years, a mean weight of 81±14.98 kg, and a mean height of 182 ± 8.36 cm. Detailed information is provided in Table 11. The participants had no history of muscle-based disorders or injury. The study was approved by the University of Iowa IRB for human subject studies, and an informed consent was obtained for each participant prior to the study. The data from seven participants were used in the parameter identification of the system, while anthropometric and response data from the eighth subject were selected for testing and validation purposes. Subjects were exposed to a total

of no more than 28 minutes of vibration, and limits established in ISO 2631-1(2010), ISO 2631-5(2004), and ISO 13090-1(1998) were considered.

Table 11: Basic information about subjects

Subject	Age	Weight (kg)	Height (cm)
1	21	69.09	170.18
2	18	88.18	180.34
3	26	95.45	177.8
4	26	65.91	185.42
5	21	93.18	185.42
6	25	63.64	182.88
7	24	100.00	198.12
8	19	69.55	175.26

4.2.2 Experiments

A six-DOF Moog-FCS 628-1800 electrical motion platform system was used in this work to generate random vibration files of 1 m/s^2 RMS in the vertical direction with frequency content of 0.5-20 Hz at the platform level. Power spectral density (Newland; 1984) across the bandwidth of 0.5-20 Hz was approximately flat for each file. All files represented a different random vibration time history 60 sec in length with sample frequency 120 Hz. Two types of support conditions were conducted on the participants. In the first type, called the rigid case, the participants were lying down and strapped to the rigid motion platform (Figure 35a) with straps over the shoulders, chest, pelvis, mid-thigh, and mid-shank. In the second type, called the litter-board case, the participants first lay down and were strapped to a long spinal-board in a similar manner to the rigid case, and then the human and board were strapped to a litter, rigidly attached to the motion platform, using straps on the chest and mid-thigh (Figure 35b). The output displacement and accelerations at the surfaces of the head (at the forehead), torso (at the sternum), and

pelvis were measured using a Vicon motion capture system (Rahmatalla and DeShaw, 2011) and inertial sensors (DeShaw and Rahmatalla, 2012).

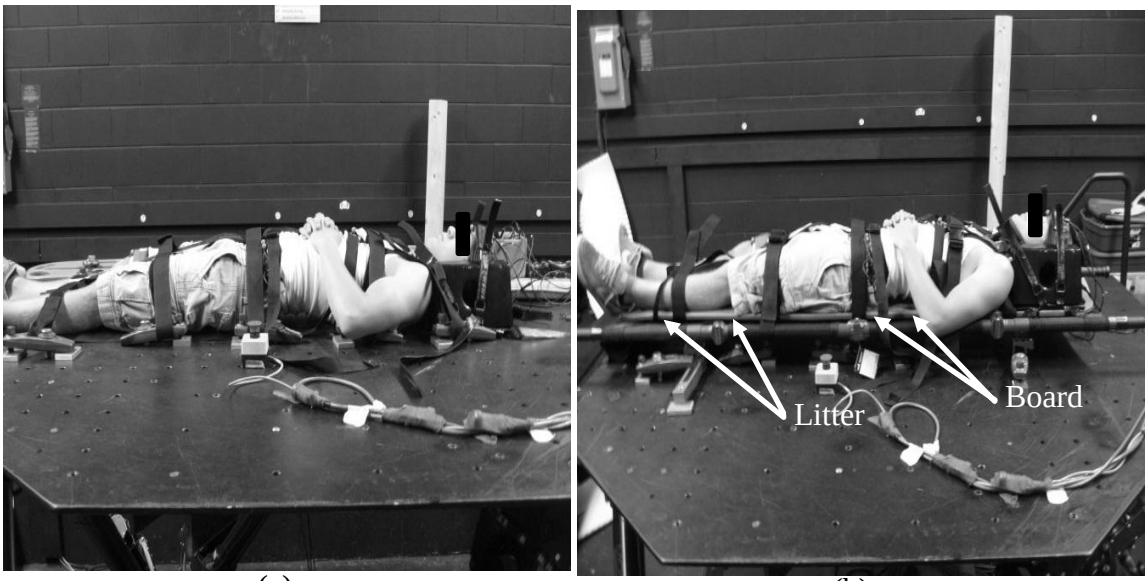

(a) (b)

Figure 35: A Supine subject on platform. (a) A supine subject lying on a rigid platform, (b) a supine subject lying on a board litter system with the latter attached firmly to the motion platform.

4.2.3 Biodynamic Measure

The single-input multiple-outputs transmissibility $H^i(f)$ is defined in this work as the complex ratio between the output vertical acceleration $\ddot{z}_i$ at the segment level and the input vertical acceleration $\ddot{z}_0$ at the rigid-platform level as shown in Eq. (4. 1).

$$\mathbf{H}^{\boldsymbol{e}}(f) = \begin{bmatrix} G_{\mathrm{X}Y_1}/G_{\mathrm{XX}} \\ G_{\mathrm{X}Y_2}/G_{\mathrm{XX}} \\ G_{\mathrm{X}Y_3}/G_{\mathrm{XX}} \end{bmatrix} \tag{4.1}$$

i is the segment's number and represents the location of the measured acceleration on the human body (1 for head, 2 for sternum, and 3 for pelvis). The geometric mean (H_g^i) is used in this work to calculate the average transmissibility of the

seven subjects (Eq. (4. 1)). H_g^i reduces the effects of noise corruption and gives an unbiased estimation of the transfer function better than the arithmetic mean(Schoukens and Pintelon, 1990).

$$H_i^g = \prod_{k=1}^{n} \sqrt[n]{[H_i{}^e(f)]_k} \tag{4.2}$$

where *k* is a counter and *n* is the number of subjects.

4.2.4 Experimental Results

4.2.4.1 Rigid Case

The experimental transmissibility and phase graphs of the seven tested subjects under the rigid-support case (Figure 36) showed observable subject inter-variability. The geometric mean transmissibility H_g^1 of the head showed a dominant resonant frequency at 16 Hz with a magnitude of 2.84. H_g^2 of the sternum showed a resonance frequency around 8 Hz with a magnitude of 1.4. H_g^3 of the pelvis showed a peak around 11 Hz with a magnitude of 1.6. The phase graphs for the head, sternum, and pelvis showed less inter-subject variability than those observed in the transmissibility graphs.

4.2.4.2 Litter-board Case

The experimental results of the transmissibility and phase of the seven subjects under the litter-board case (Figure 37) showed similar characteristics to that of the rigid case in terms of subject inter-variability; however, the transmissibility peaks at resonance were more dominant than those in the rigid case. H_g^1 showed two peaks around 5.2 Hz and 11 Hz with a magnitude of 1.8 and 2.0, respectively. H_g^2 showed a peak around 5.4 Hz with a magnitude of 3.5. H_g^3 showed a peak around 5.2 Hz with a magnitude of 3.3. The phase graphs for the head, torso, and pelvis showed more inter-subject variability than in the rigid case.

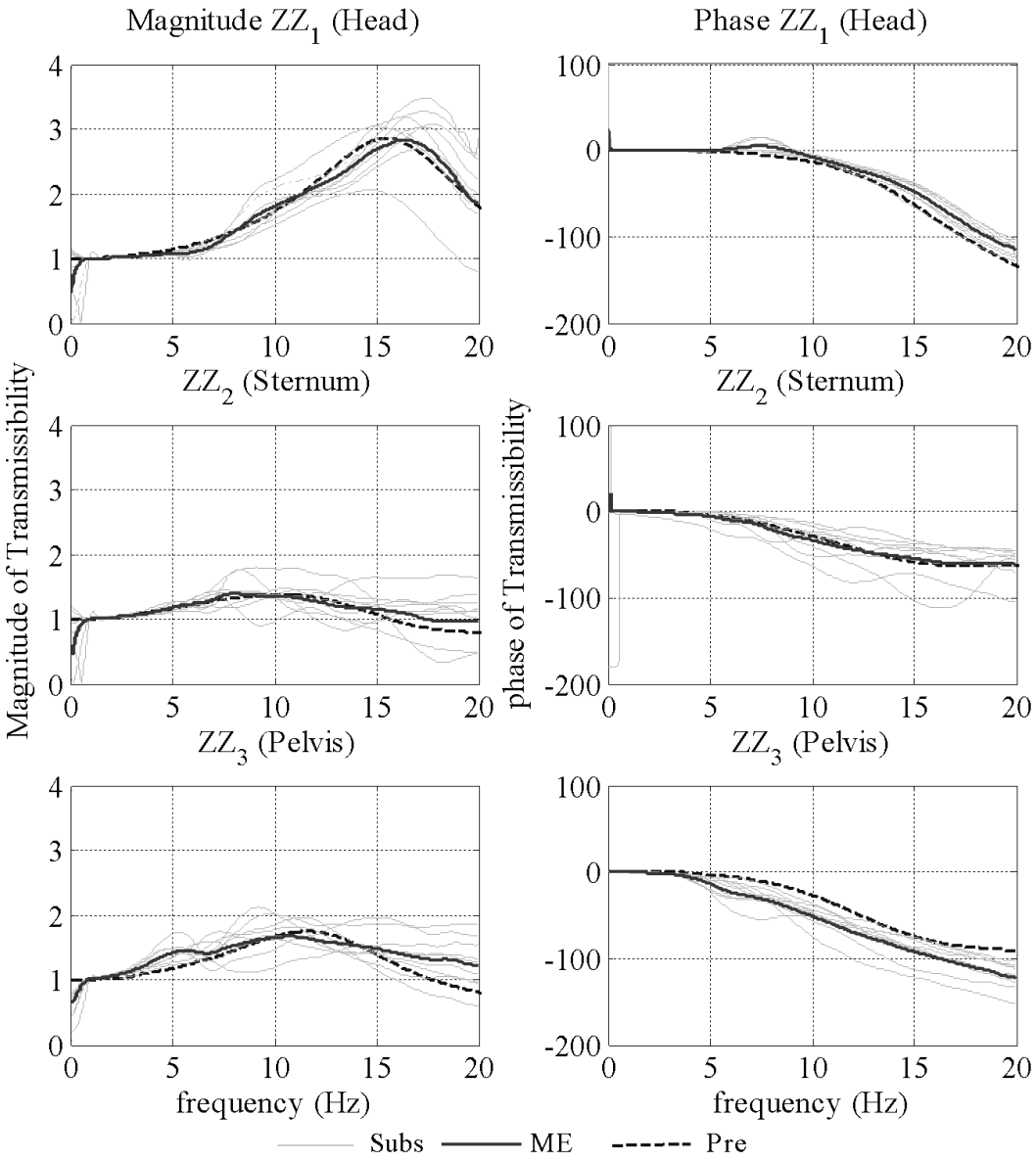

Figure 36: Rigid-case experimental and optimization results. The thin lines are the experimental transmissibility of seven subjects; the dashed thick lines are the experimental geometric mean transmissibility (ME) of the seven subjects; and the solid thick lines are the optimization results of transmissibility (Pre).

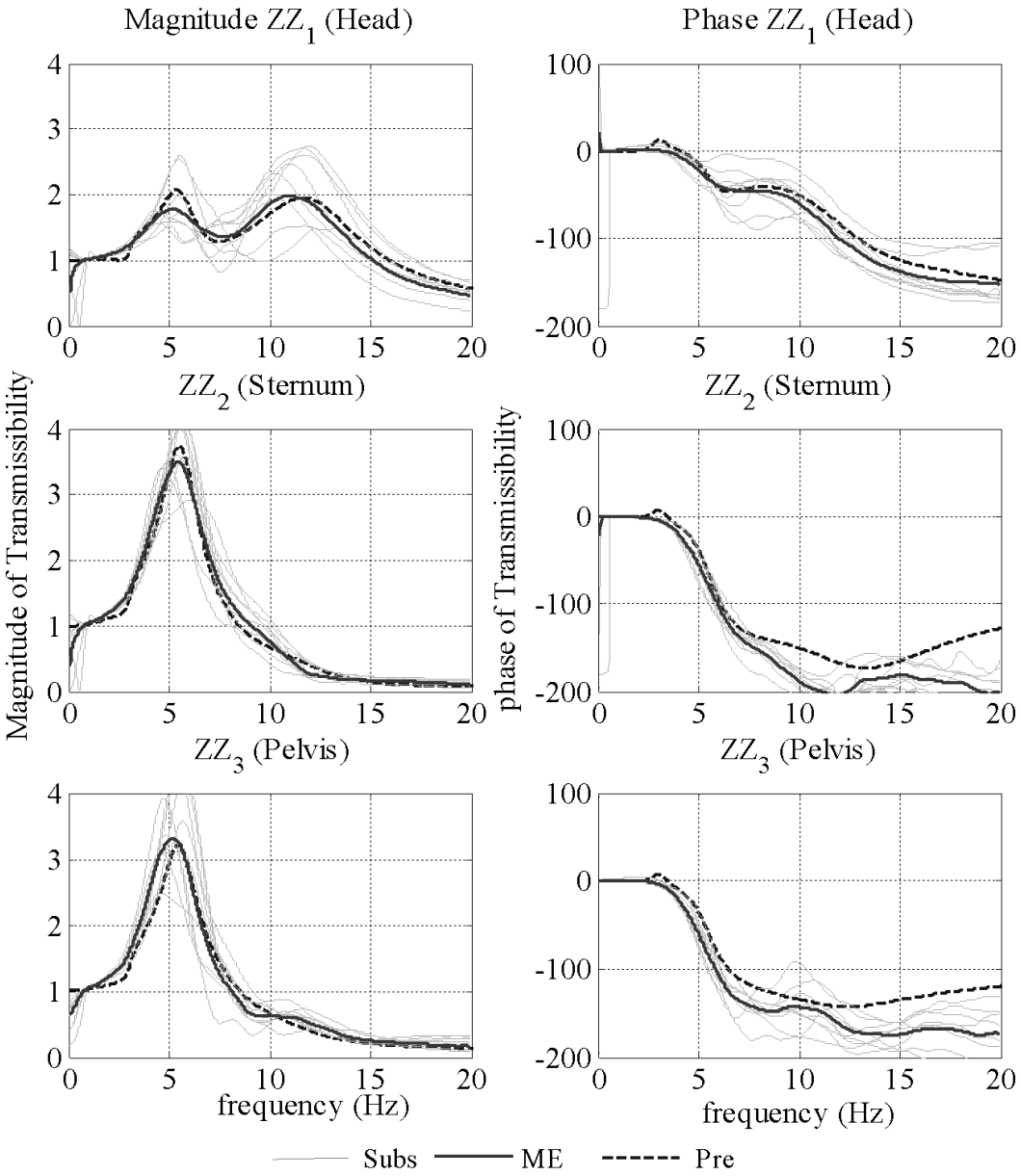

Figure 37: Litter-board case experimental and optimization results. The thin lines are the experimental transmissibility of seven subjects; the dashed thick lines are the experimental geometric mean transmissibility (ME) of the seven subjects; and the solid thick lines are the optimization results of transmissibility (Pre).

4.3 Modeling

4.3.1 Rigid Case

4.3.1.1 Geometric description

Figure 38 shows a schematic representation of the proposed supine human model and the underlying support for the rigid-case condition. The human is modeled with three segments: the head (spherical segment), representing the head and neck with a center of mass at position $\mathbf{Z}_1$*;* the torso (ellipsoid segment), representing the thorax, abdomen, and arms with a center at of mass position $\mathbf{Z}_2$; and the pelvis (ellipsoid segment), representing the hips and legs, with a center of mass at position $\mathbf{Z}_3$. The position of the segment's centers is expressed as $\mathbf{Z}_\mathbf{i} = [x_i,\ z_i]^T$ *i*=1 for the head, 2 for the torso, 3 for the pelvis. x_i and z_i represent the horizontal and vertical positions, respectively, of the segment's center. Due to the difficulty of experimentally measuring the motion of the center of each segment directly, the position and acceleration of selected points on the surfaces of the head ($\mathbf{Z}_1^e$) (forehead), torso ($\mathbf{Z}_2^e$) (sternum), and pelvis ($\mathbf{Z}_3^e$) were measured. The position of the lateral points can be expressed as $\mathbf{Z_i^e} = [x_i^e,\ z_i^e]^T$. The relationship between the position of the center of the segment, $\mathbf{Z_i}$, and the experimental (testing) position, $\mathbf{Z_i^e}$, on each segment can be expressed using the following transformation:

$$\mathbf{Z_i^e} = \mathbf{Z_i} + \mathbf{T}\,\mathbf{P_i^e} \tag{4.3}$$

where $\mathbf{T}$ is a transformation matrix

$$\mathbf{T} = \begin{bmatrix} \cos\theta_i & -\sin\theta_i \\ \sin\theta_i & \cos\theta_i \end{bmatrix} \tag{4.4}$$

and $\mathbf{P_i^e} = [P_{ix}^e,\ P_{iz}^e]^T$ is the Cartesian distance between the center of the segment and the location of the sensors on the segment.

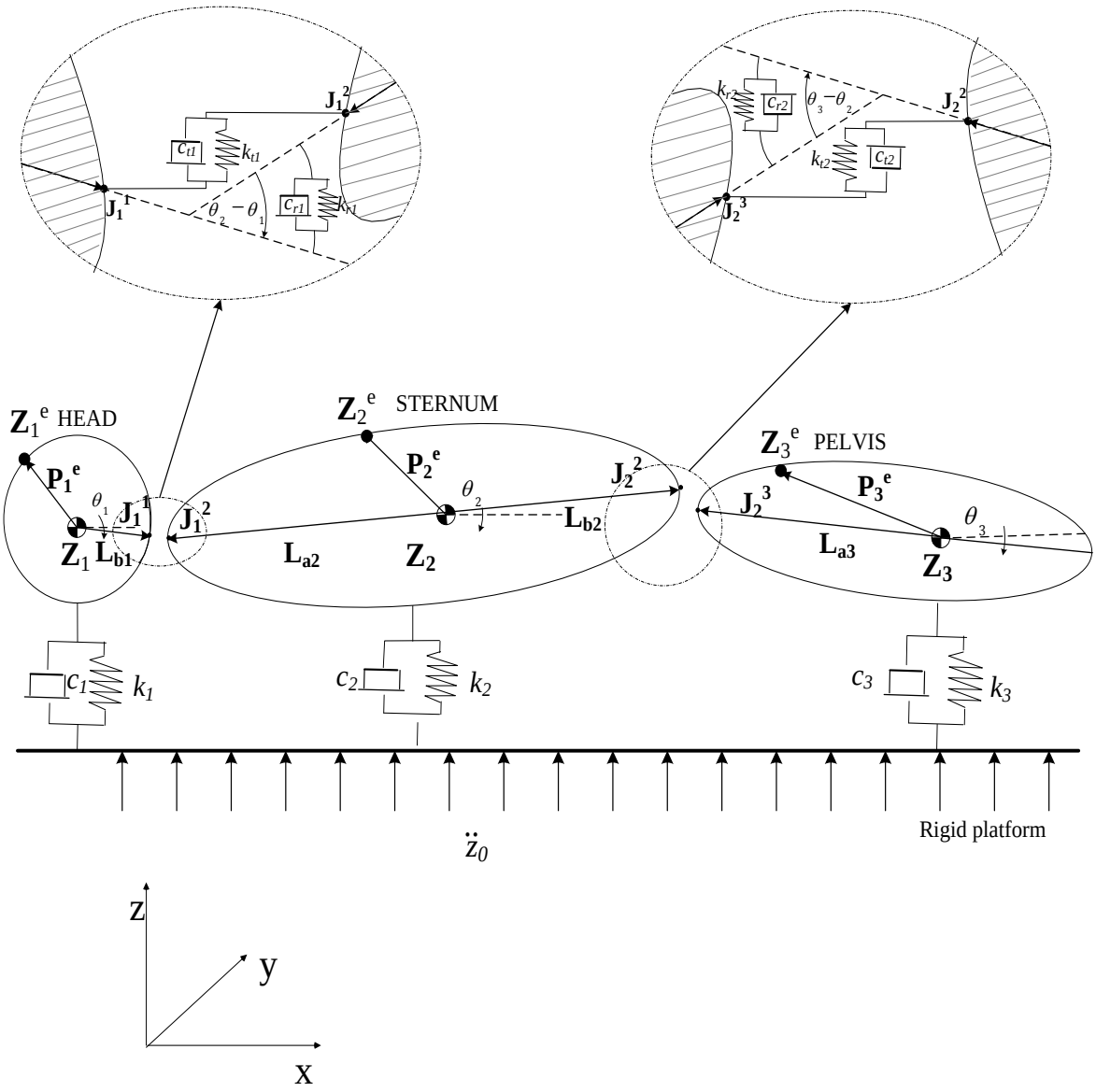

Figure 38: Schematic drawing of the supine human model and the underlying transport system for the rigid case.

The head, torso, and pelvis are connected via the rotational and translational joints $\mathbf{J}_1$ and $\mathbf{J}_2$. $\mathbf{J}_1$ represents the joint between the head and torso, and $\mathbf{J}_2$ represents the joint between the torso and pelvis. $\mathbf{J}_1$ has two components: $\mathbf{J}_1^1$ represents the location of $\mathbf{J}_1$ on the head side, and $\mathbf{J}_1^2$ represents the location of $\mathbf{J}_1$ on the torso side as shown in Figure 38 in the left zoom-in picture . Similarly, $\mathbf{J}_2$ has two components: $\mathbf{J}_2^2$ represents the location

of $\mathbf{J}_2$on the torso side, and $\mathbf{J}_2^3$ represents the location of $\mathbf{J}_2$ on the pelvis side as shown in Figure 38 in the right zoom-in picture. The horizontal (x) and vertical (z) components of the position of each joint can be represented as $\mathbf{J_m^i} = \left[J_{mx}^i,\ J_{mz}^i\right]^T$ where m=1, 2. The vectors from the center of each segment $\mathbf{Z}_i$ to the connection joint $\mathbf{J_m^i}$ between two body segments are $\mathbf{L}_{\mathbf{b}\boldsymbol{m}} = [L_{bmx},\ L_{bmz}]^T$ and $\mathbf{L}_{an} = [L_{anx},\ L_{anz}]^T$, ($m$=1, 2 and n =2, 3). The position of $\mathbf{J}_m^i$ can be found using the following transformation:

$$\left.\begin{aligned} \mathbf{J}_1^1 &= \mathbf{Z}_1 + \mathbf{T}\mathbf{L}_{b1} \\ \mathbf{J}_1^2 &= \mathbf{Z}_2 + \mathbf{T}\mathbf{L}_{a2} \\ \mathbf{J}_2^2 &= \mathbf{Z}_2 + \mathbf{T}\mathbf{L}_{b2} \\ \mathbf{J}_2^3 &= \mathbf{Z}_3 + \mathbf{T}\mathbf{L}_{a3} \end{aligned}\right\} \tag{4.5}$$

4.3.1.2 Dynamic Equation

In Figure 38, $\ddot{z}_0$ represents the vertical z direction of the input platform random acceleration. $\ddot{z}_1$, $\ddot{z}_2$, and $\ddot{z}_3$ represent the vertical accelerations of the geometric center of the head, torso, and pelvis, respectively. The proposed supine-human model has six DOFs: z_1, z_2, z_3 represent the vertical translational motion of the head, torso, and pelvis, respectively, and θ_1, θ_2, θ_3 represent the rotation of the head, torso, and pelvis, respectively. The first segment represents the head and neck (C_7-T_1 to ear canal) with a mass m_1 at position $\mathbf{Z}_1$; the second segment represents the torso, including the thorax and abdomen (from C_7-T_1 to L_4-L_5) and arms with mass m_2 at position $\mathbf{Z}_2$; and the third segment represents the hips and legs, including the pelvis (L_4-L_5 to trochanter) and legs and feet with a mass m_3 at position $\mathbf{Z}_3$. The segments have a mass m_i and a moment of inertia I_i. The basic mass and inertia information of the human body segments were obtained from the literature (Dempster and Gaughran, 1967; Winter, 1979; Winter, 2005) and were based on the ratio of the segment mass relative to that of the total body mass, as shown in Table 12. The ratio of length of each segment to the total height is shown in Figure 39.

Table 12: Body segments' masses and lengths based on the literature (Schoukens and Pintelon, 1990)

	Head and Neck	Torso	Hip, Legs, and Feet
Ratio mass/total mass	0.081	0.455	0.464
Segment length/height	0.182	0.288	0.53
Proximal length (La/L)	-	0.63	0.105
Proximal length (Lb/L)	0.118	0.37	0.895
Gyration/segment	0.495	0.496	0.326

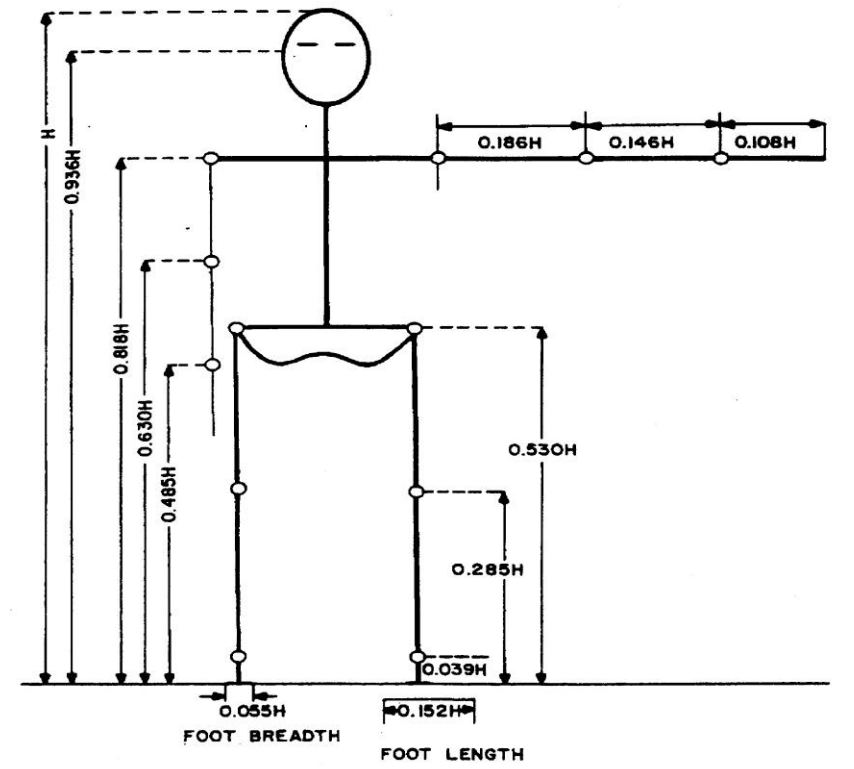

Figure 3.9 Some body segment lengths expressed as proportion of body stature by Drillis and Contini (Roebuck, Kroemer, and Thomson, 1975).

Figure 39: Body segment lengths expressed as proportion of body stature by Drillis and Contini (Roebuck, Kroemer and Thomson, 1975) (Cited from Winter book).

The stiffness and damping characteristics of the vertebras, ligaments, tendons, and muscles are modeled as translational and rotational spring and damper elements and were lumped between the adjacent segments at the joints $\mathbf{J}_m^i$. The translational stiffness components at joints $\mathbf{J}_1$ and $\mathbf{J}_2$ are represented by k_{t1} and k_{t2}, respectively, and the rotational stiffness components are represented by k_{r1}, k_{r2}. The translational damping components are represented by c_{t1} and c_{t2}, and the rotational damping components by c_{r1} and c_{r2}. The contact points between the body segments and the underlying rigid support are represented by springs with coefficient k_i and dampers with coefficient c_i.

The forces between the adjacent segments at joints $\mathbf{J}_1$ and $\mathbf{J}_2$ are illustrated in Eqs. (4.6)-(4.9). The joint forces are produced by the translation motion in the z-axis direction and the rotation motion about the y-axis. In this work, the forces due to translation in the horizontal x-direction are considered negligible compared to the forces in the other directions. Equations (4.6)-(4.7) illustrate the forces at joints $\mathbf{J}_1$ and $\mathbf{J}_2$ due to the translation motion in the vertical direction, while Eqs. (4.8)-(4.9) illustrate the moment at joints $\mathbf{J}_1$ and $\mathbf{J}_2$ due to the rotational motion.

$$f_{J1} = k_{t1} l_{12z} + c_{t1} \dot{l}_{12z} \tag{4.6}$$

$$f_{J2} = k_{t2} l_{23z} + c_{t2} \dot{l}_{23z} \tag{4.7}$$

$$M_{J1} = k_{r1}(\theta_2 - \theta_1) + c_{r1}(\dot{\theta}_2 - \dot{\theta}_1) \tag{4.8}$$

$$M_{J2} = k_{r2}(\theta_3 - \theta_2) + c_{r2}(\dot{\theta}_3 - \dot{\theta}_2) \tag{4.9}$$

where $\mathbf{l}_{12} = [l_{12x},\ l_{12z}]^T$ represents the displacement between joints $\mathbf{J}_1^2$ and $\mathbf{J}_1^1$, and $\boldsymbol{l}_{32} = [l_{32x},\ l_{32z}]^T$ represents the displacement between joints $\mathbf{J}_2^3$ and $\mathbf{J}_2^2$. The equations for $\boldsymbol{l}_{12}$ and $\boldsymbol{l}_{32}$ are shown in Eqs. (4.10)-(4.11).

$$\mathbf{l}_{12} = \mathbf{J}_1^2 - \mathbf{J}_1^1 = \mathbf{Z}_2 + \mathbf{T}_2\mathbf{L}_{2a} - \mathbf{Z}_1 + \mathbf{T}_1\mathbf{L}_{1b} \tag{4.10}$$

$$\mathbf{l}_{32} = \mathbf{J}_2^3 - \mathbf{J}_2^2 = \mathbf{Z}_3 + \mathbf{T}_3\mathbf{L}_{3a} - \mathbf{Z}_2 + \mathbf{T}_2\mathbf{L}_{2b} \tag{4.11}$$

The contract forces (f_{ci}) between each segment and the rigid platform is shown in Eq. (4.12).

$$f_{ci} = k_i(z_i - z_0) + c_i(\dot{z}_i - \dot{z}_0) \tag{4.12}$$

The dynamic equation for the dynamic model is derived by the Lagrangian equation as follows:

$$\tau = \frac{d}{dt}\left(\frac{\partial L}{\partial \dot{\mathbf{x}}}\right) - \frac{\partial L}{\partial \mathbf{x}} + \frac{\partial D}{\partial \dot{\mathbf{x}}} \tag{4.13}$$

where L is the Lagrangian $L = T - V$, T is the kinetic energy, V is the potential energy, and D is the dissipation energy.

$$T = \sum_{i=1}^{3}\left(\frac{1}{2}I_i\dot{\theta}_i^{\,2} + \frac{1}{2}m_i\dot{z}_i^{\,2}\right) \tag{4.14}$$

$$V = \sum_{i=1}^{3}\left[\frac{1}{2}k_i(z_i - z_0)^2 + \frac{1}{2}m_i g z_i\right] + \sum_{i=1}^{2}\left[\frac{1}{2}k_{ti}l_{12}^{\,2} + \frac{1}{2}k_{ri}(\theta_{i+1} - \theta_i)^2\right] \tag{4.15}$$

$$D = \sum_{i=1}^{3}\left[\frac{1}{2}c_i(\dot{z}_i - \dot{z}_0)^2\right] + \sum_{i=1}^{2}\left[\frac{1}{2}c_{ti}\dot{l}_{12}^{\,2} + \frac{1}{2}c_{ri}(\dot{\theta}_{i+1} - \dot{\theta}_i)^2\right] \tag{4.16}$$

A linear expression of the dynamic Eq. (4.13) is derived by taking the Taylor's series first expansion at the equilibrium state $\mathbf{x_0} = \{z_{1o}, z_{2o}, z_{3o}, \theta_{1o}, \theta_{2o}, \theta_{3o}\}^{\mathrm{T}}$ where $\mathbf{x_0}$ is initial position position of $\mathbf{x} = \{z_1, z_2, z_3, \theta_1, \theta_2, \theta_3\}^{\mathrm{T}}$.

$$\mathbf{M}\ddot{\mathbf{x}} + \mathbf{C}\dot{\mathbf{x}} + \mathbf{K}\mathbf{x} = \boldsymbol{\alpha}_{\mathrm{k}} z_0 + \boldsymbol{\alpha}_{\mathrm{c}}\dot{z}_0 \tag{4.17}$$

where $\mathbf{M} = \left.\frac{\partial(\Delta\tau)}{\partial\,\ddot{\mathbf{x}}}\right|_{\mathbf{x}=\mathbf{x}_0}$, $\mathbf{M}$ is a diagonal matrix of (m_1, m_2, m_3, I_1, I_2, I_3),

$\mathbf{C} = \left.\frac{\partial(\Delta\tau)}{\partial\dot{\mathbf{x}}}\right|_{\mathbf{x}=\mathbf{x}_0} =$

$$\begin{bmatrix} c_1+c_{t1} & -c_{t1} & 0 & c_{t1}L_{b1x} & -c_{t1}L_{a2x} & 0 \\ -c_{t1} & c_2+c_{t1}+c_{t2} & -c_{t2} & -c_{t1}L_{b1x} & c_{t2}L_{b2x}+c_{t1}L_{a2x} & -c_{t2}L_{a3x} \\ 0 & -c_{t2} & c_3+c_{t2} & 0 & -c_{t2}L_{b2x} & -c_{t2}L_{a3x} \\ c_{t1}L_{b1x} & -c_{t1}L_{b1x} & 0 & {c_{t1}L_{b1x}}^2+c_{r1} & -c_{t1}L_{b1x}L_{a2x}-c_{r1} & 0 \\ -c_{t1}L_{a2x} & c_{t2}L_{a2x}+c_{t1}L_{a2x} & -c_{t2}L_{b2x} & -c_{t1}L_{b1x}L_{a2x}-c_{r1} & {c_{t1}L_{a2x}}^2+{c_{t2}L_{b2x}}^2+c_{r1}+c_{r2} & -c_{t2}L_{b2x}L_{a3x}-c_{r2} \\ 0 & -c_{t2}L_{a3x} & c_{t2}L_{a3x} & 0 & -c_2-c_{t2}L_{b2x}L_{a3x} & {c_{t2}L_{a3x}}^2+c_{r2} \end{bmatrix} \tag{4.18}$$

$$\mathbf{K} = \left.\frac{\partial(\Delta\tau)}{\partial\mathbf{x}}\right|_{\mathbf{x}=\mathbf{x}_0} = \begin{bmatrix} k_1+k_{t1} & -k_{t1} & 0 & k_{t1}L_{b1x} & -k_{t1}L_{a2x} & 0 \\ -k_{t1} & k_2+k_{t1}+k_{t2} & -k_{t2} & -k_{t1}L_{b1x} & k_{t1}L_{a2x}+k_{t2}L_{b2x} & -k_{t2}L_{a3x} \\ 0 & -k_{t2} & k_3+k_{t2} & 0 & -k_{t2}L_{b2} & k_{t2}L_{a3x} \\ k_{t1}L_{b1x} & -k_{t1}L_{b1x} & 0 & {k_{t1}L_{b1x}}^2+k_{r1}-k_{t1}L_{b1z}(L_{b1z}-L_{a2z}) & -k_{t1}L_{b1x}L_{a2x}-k_{r1} & 0 \\ -k_{t1}L_{a2x} & k_{t1}L_{a2x}+k_{t2}L_{b2x} & -k_{t2}L_{b2x} & -k_{t1}L_{b1x}L_{a2x}-k_{r1} & k_{55} & -k_{t2}-k_{t2}L_{b2x}L_{a3x} \\ 0 & -k_{t2}L_{a3x} & k_{t2}L_{a3x} & 0 & -k_{r2}-k_{t2}L_{b2x}L_{a3x} & k_{66} \end{bmatrix} \tag{4.19}$$

where $k_{44} = k_{t1}{L_{b1x}}^2 + k_{r1} - k_{t1}L_{b1z}(L_{b1z} - L_{a2z})$,

$$k_{55} = k_{t1}{L_{a2x}}^2 + k_{t2}{L_{b2x}}^2 + k_{r1} + k_{r2} - k_{t1}L_{a2z}(L_{a2z} - L_{b1z}) - k_{t2}L_{b2z}(L_{b2z} - L_{a3z})$$

$$k_{66} = k_{t2}{L_{a3x}}^2 + k_{t2} - k_{t2}L_{a3z}(L_{a3z} - L_{b2z})$$

$$\boldsymbol{\alpha}_{\mathbf{k}} = \{k_1, k_2, k_3, 0, 0, 0\}^T \tag{4.20}$$

$$\boldsymbol{\alpha}_{\mathbf{c}} = \{c_1, c_2, c_3, 0, 0, 0\}^T \tag{4.21}$$

The theoretical transmissibility ($\mathbf{H^{th}}(f)$) between the output acceleration at the testing locations and the input vertical acceleration is demonstrated in Eq. (4.22). In this equation, matrix **R** represents the transformation between the accelerations at the segment surface(the testing point of each segment) and the center of each segment. The linearized form of **R** is shown in Eq. (4.23), and $\mathbf{H^{th}}(f) = [{H_1}^{th}, {H_2}^{th}, {H_3}^{th}]^T$.

$$\mathbf{H^{th}}(f) = \mathbf{R}\mathbf{H}(f) \tag{4.22}$$

$$\mathbf{R} = \begin{bmatrix} 1 & 0 & 0 & P_{x1} & 0 & 0 \\ 0 & 1 & 0 & 0 & P_{x2} & 0 \\ 0 & 0 & 1 & 0 & 0 & P_{x3} \end{bmatrix} \tag{4.23}$$

$$\mathbf{H}(s) = (\mathbf{M}s^2 + \mathbf{C}\mathbf{s} + \mathbf{K})^{-1} \times (\boldsymbol{\alpha}_{\mathbf{k}} + \boldsymbol{\alpha}_{\mathbf{c}}s) \tag{4.24}$$

4.3.1.3 System Identification

The unknown biomechanical model's parameters are the translational and rotational spring and damping coefficients at each joint and the contact spring and damping coefficients between the body segments and the rigid platform. These unknown parameters are identified by matching the model and the experimental transmissibility and phase.

Optimization schemes are used to identify the system parameters. The design variables of the optimization problem are the unknown parameters $\mathbf{x}^r$,

$\mathbf{x^r} = \{x_1, x_2, \dots, x_{14}\}^T = \{k_1, k_2, k_3, c_1, c_2, c_3, k_{t1}, k_{t2}, c_{t1}, c_{t2}, k_{r1}, k_{r2}, c_{r1}, c_{r2}\}^T$.

The objective function is f^{obj}. Equation (4.25) represents the normalized differences between the predicted and experimental transmissibility and phase.

$$f^{obj} = \sum_{i=1}^{3} \sum_f \left\{ \frac{|H_i{}^{th}(f)| - |H_i{}^{g}(f)|}{\| |H_{ii}(f)| - |H_{ii}{}^{g}(f)| \|} \right\}^2 + \sum_f \left\{ \frac{Pha\left(H_i{}^{th}(f)\right) - Pha\left(H_i{}^{g}(f)\right)}{\left\| Pha\left(H_i{}^{th}(f)\right) - Pha\left(H_i{}^{g}(f)\right) \right\|} \right\}^2 \quad (4.25)$$

where $H_i{}^{g}(f)$ represents the experimental transmissibility, $|.|$ represents the magnitude of transmissibility, and $Pha(.)$ represents the phase of the transmissibility.

The upper boundary limits on the design variables are considered as $\mathbf{UB}^r$:

$\mathbf{UB}^r = \{100,100,100,50,50,50,100,100,50,50,100,100,50,50\} * 10000$

The lower boundary limits are considered as $\mathbf{LB}^r$: $\mathbf{LB^r} = \{0.001, 0.001, 0.001, 0.001, 0.001, 0.001, 0.001, 0.001, 0.001, 0.001, 0.001, 0.001, 0.001, 0.001\}$. The starting points for the design variables are denoted as $\mathbf{x}_0{}^r$, $\mathbf{x}_0{}^r = \{1, 1, 1, 1, 1, 1, 1, 1, 1, 1, 1, 1, 1, 1\}^T$. The frequency (f) in Eq. (4.24) is considered from 0 Hz to 20 Hz.

The nonlinear least square method (Mathworks, 2010) with the trust region reflective algorithm is used to solve the nonlinear minimization problem.

4.3.2 Litter-board Case

The geometric description of the litter-board case (Figure 40) is similar to the rigid case (Figure 38) but with the addition of the litter-board model. In the litter-board model, the board is modeled as a rigid flat strip. The litter is modeled by a series of linear translational spring and damper elements (Figure 40) represented by k_{bi} and c_{bi}. The total contact forces between the human segments and the litter-board are lumped and presented as:

$$f_{ci} = \frac{k_i\, k_{bi}}{k_i + k_{bi}}(z_1 - z_0) + \frac{c_i\, c_{bi}}{c_i + c_{bi}}(\dot{z}_1 - \dot{z}_0)$$

$$f_{ci} = k_{eqi}(z_1 - z_0) + c_{eqi}(\dot{z}_1 - \dot{z}_0) \quad (i=1, 2, 3) \tag{4.26}$$

where $k_{eqi} = k_i\,[k_{bi}/(k_i + k_{bi})] = \mu_i^k k_i$ and $c_{eqi} = c_i[\,c_{bi}/(\,c_i + c_{bi})] = \mu_i^c c_i$. μ_i^c and μ_i^k are the softening damper and spring coefficients.

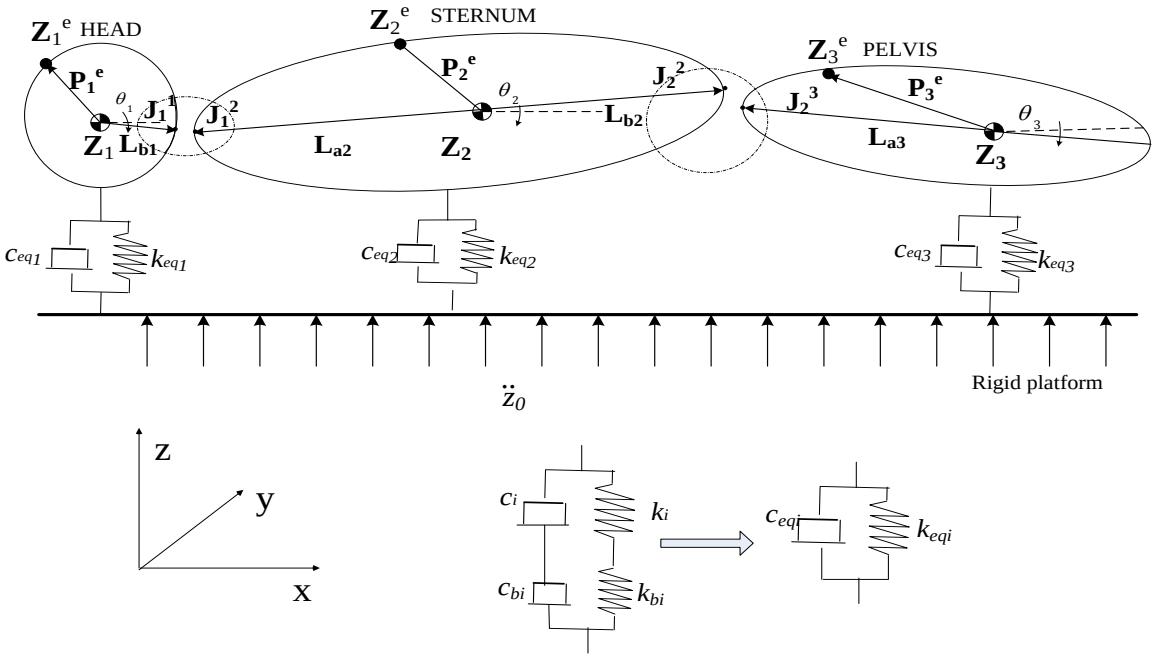

Figure 40: Schematic drawing of the supine human model and the underlying transport system for the litter-board case.

The supine-human parameters are similar to those in the rigid-case condition. The equivalent parameters of c_{bi} and k_{bi} are characterized based on optimization schemes similar to those of the rigid case. The objective function form is similar to the rigid-case model (Eq. (4.24)). The design variables of the optimization are ($\mathbf{x}^l$), $\mathbf{x}^l = [x_1,\ x_2,\ \ldots,\ x_6]^T = [\mu_1^k,\ \mu_2^k, \mu_3^k, \mu_1^c, \mu_2^c, \mu_3^c]^T$. The upper and lower boundary on the design variables are considered as $\mathbf{UB}^l$, $\mathbf{UB}^l = \{1, 1, 1, 1, 1, 1\}^T$, the lower boundary limits are considered as $\mathbf{LB}^l$, $\mathbf{LB}^l = \{0.001,\ 0.001,\ 0.001,\ 0.001,\ 0.001,\ 0.001\}^T$, and the starting point for the optimization is denoted as $\mathbf{x_0}^l$, $\mathbf{x_0}^l = \{1, 1, 1, 1, 1, 1\}^T$.

4.4 Results

Table 13 demonstrates the optimization results of the stiffness and damping coefficients of the supine human, while Table 13 shows the stiffness and damping coefficients for the litter-board transport system.

Figure 37 and Figure 36 show the transmissibility and phase results for the rigid case and the litter-board case, respectively. The thick solid line represents the experimental geometrical mean of seven subjects, and the thick dashed line represents the optimization results. As shown in the figures, the optimization results, to some extent, followed the basic trends of the mean experimental response and were able to capture the primary peaks with small shifts. However, the transmissibility magnitudes were close to those of the experiments.

In Figures 41-44, the response data of the eighth subject were compared with the dynamic model. It should be noted that the anthropometrical data of the dynamic model were based on the measurement of the eighth subject. Also, the comparison between the response of eighth subject and the dynamic model were conducted under vibration files that were not used in the system's parameters identification process shown in Eq. (4. 2).

The predicted acceleration of the head for the rigid-case (Figure 41) showed better trend to that of pelvis and torso; however, the predicted acceleration for the torso

followed the experimental peaks but was not able to reach the experimental magnitudes. The picture is different for the litter-board case (Figure 42), where the predicted acceleration of the torso showed better trend in comparison to the pelvis and head.

The PSD of the predicted acceleration of the rigid case for the head, torso, and pelvis (Figure 43) were able to capture most of the frequency components of the experimental data. The predicted PSD magnitude of the head showed the best performance when compared to the torso and pelvis. Similar characteristics were observed for the litter-board case (Figure 44) in terms of capturing the frequency content of the signals; however, the magnitude of the PSD at the pelvis was better than those of the torso and head.

Table 13: Supine human model spring and damper coefficients for three DOF

	Head	Torso	Pelvis	Rotational Joint 1	Translate Joint 1	Rotational Joint 2	Translate Joint 2
Spring	*55448.23*	*207185.39*	*242609.46*	*3132.58*	*7578.2373*	*540962.6422*	*10195.0095*
Damper	*172.94467*	*3449.5632*	*2155.1538*	*0.001058910*	*147.39050*	*48681.06650*	*183.7761*
Spring coefficient unit*: N/m* (translate) and *N·m/rad* (rotational) Damper coefficient unit: *N·s/m* (translate) and *N·m·s/rad* (rotational)							

Table 14: Litter-board spring and damper coefficients

	k_{b1}	k_{b2}	k_{b3}	c_{b1}	c_{b2}	c_{b3}
coefficients	*61269.92*	*44843.74*	*62264.61*	*126.77*	*361.24*	*645.83*
Spring coefficient unit: N/m (translate) Damper coefficient unit: N·s/m (translate)						

Table 15: Litter-board spring and damper softening coefficients.

	μ_1^k	μ_2^k	μ_3^k	μ_1^c	μ_2^c	μ_3^c
coefficients	*0.423*	*0.0948*	*0.2306*	*0.5249*	*0.1779*	*0.2042*

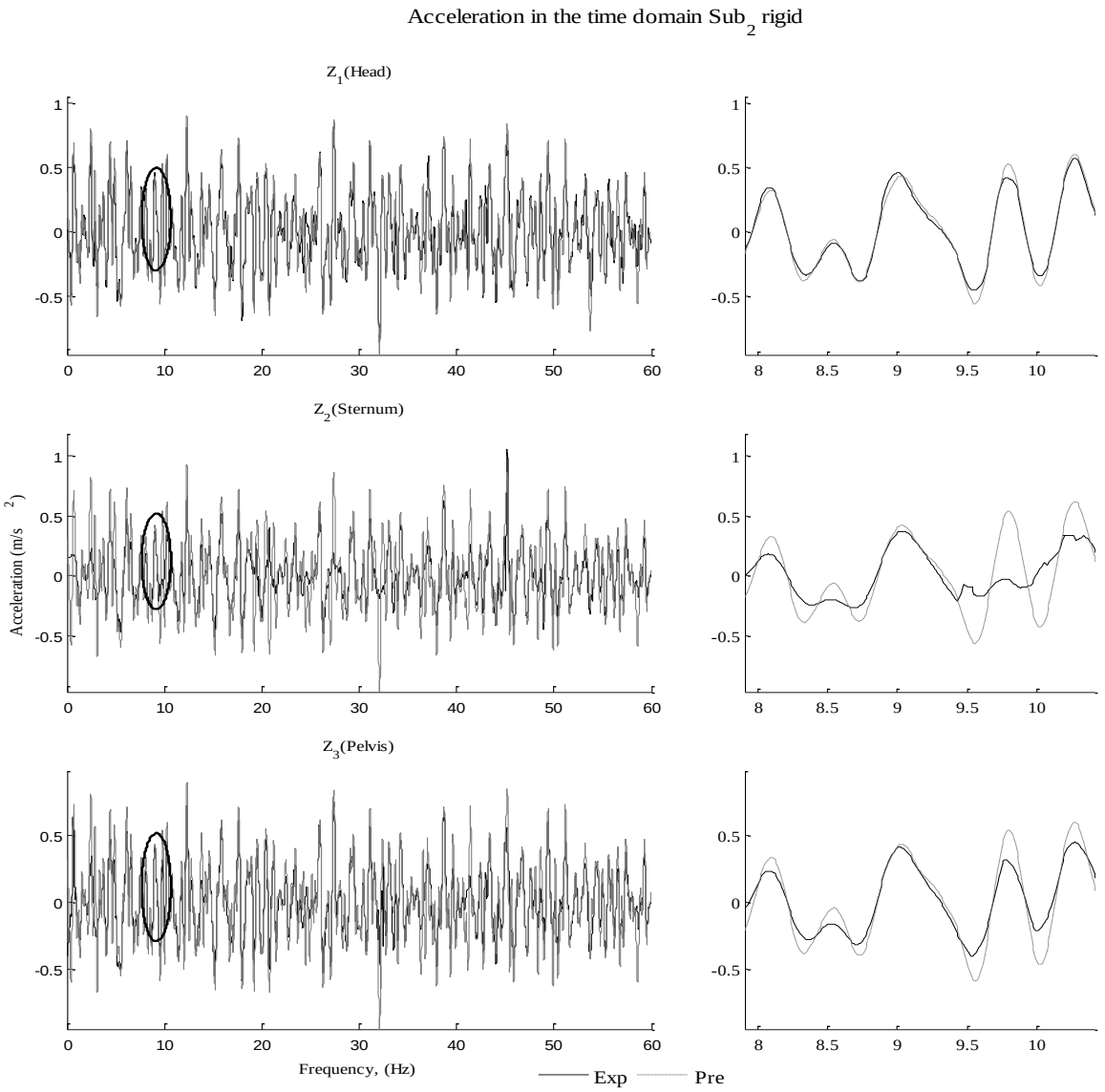

Figure 41: The time domain experimental (Subject Eight) and predicted (based on anthropometrical data of Subject Eight) acceleration for the head, torso, and pelvis under the rigid-case condition.

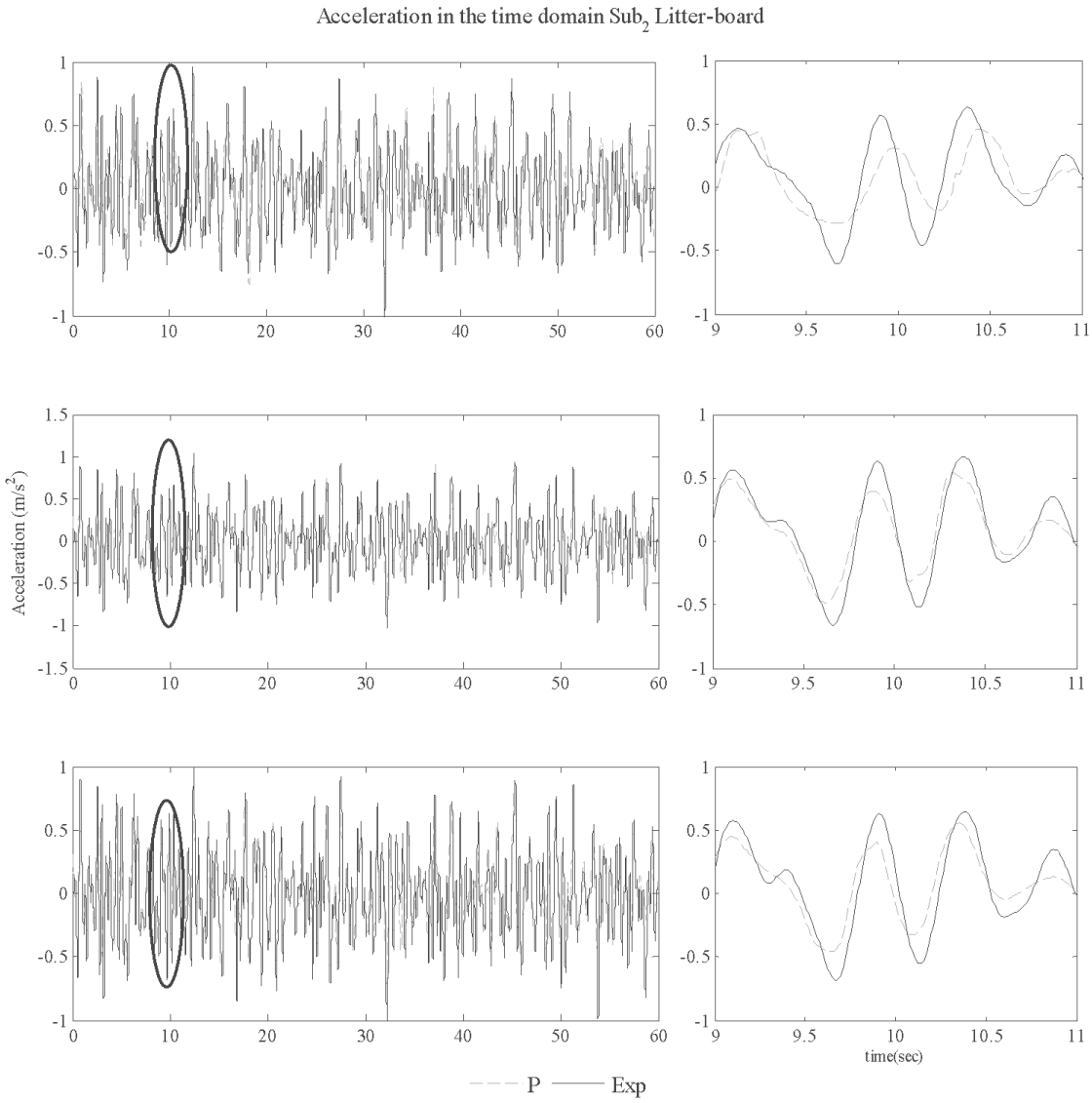

Figure 42: The time domain experimental (Subject 8) and predicted (based on anthropometrical data of Subject 8) acceleration for the head, torso, and pelvis under the litter-board condition.

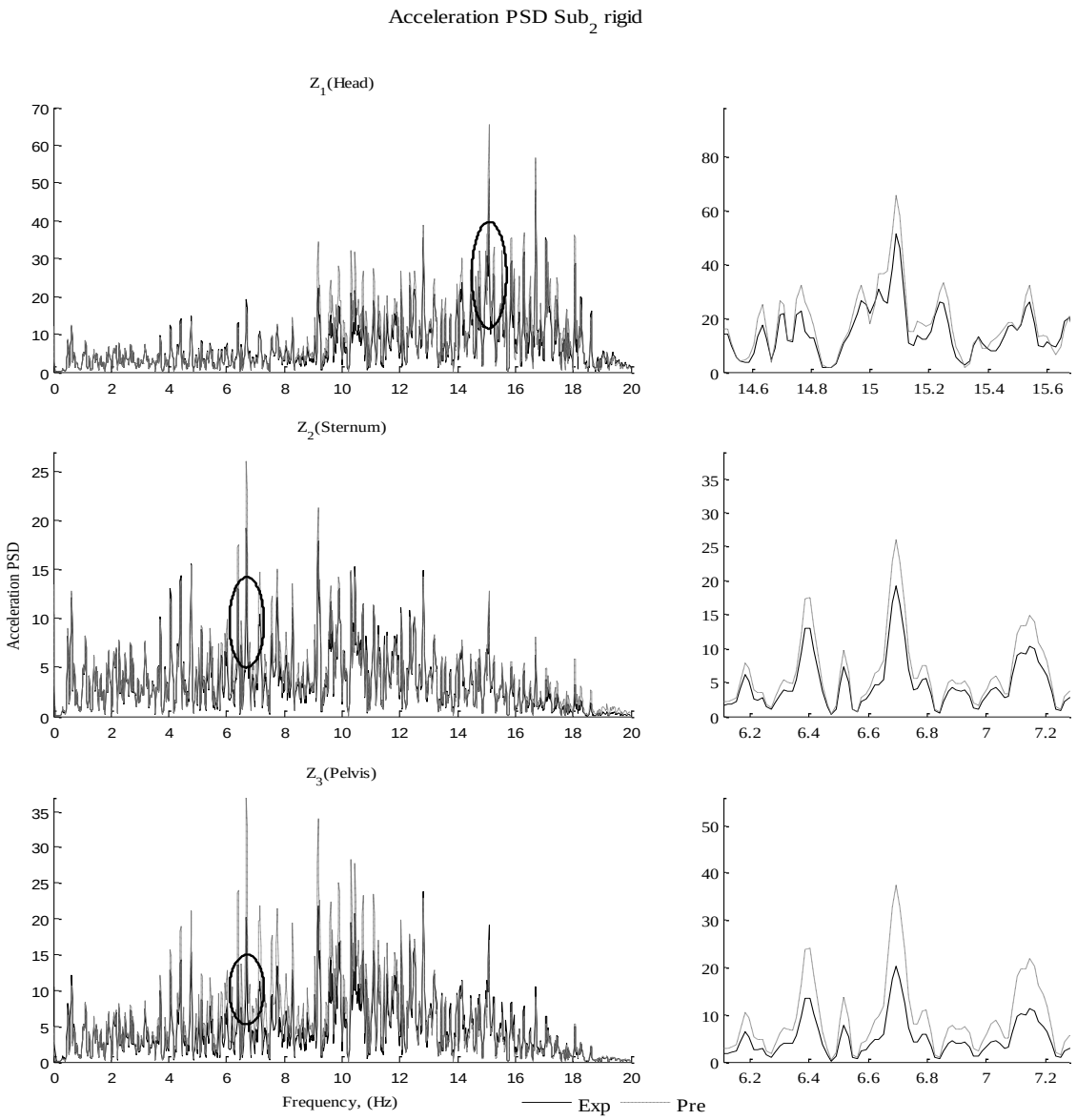

Figure 43: The frequency domain experimental (Subject 8) and predicted (based on anthropometrical data of Subject 8) acceleration for the head, torso, and pelvis under the rigid-case condition.

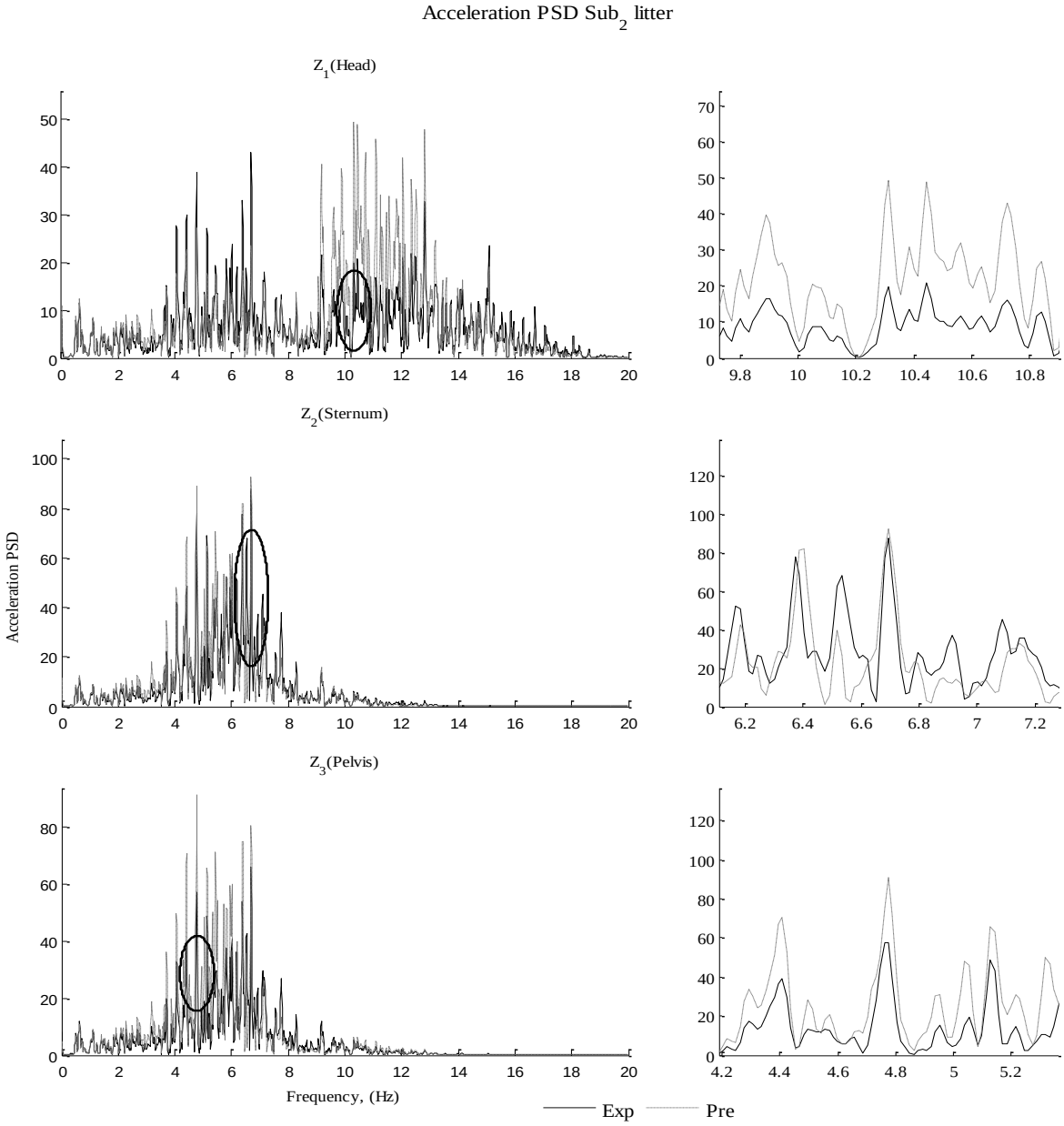

Figure 44: The frequency domain experimental (Subject 8) and predicted (based on anthropometrical data of Subject 8) acceleration for the head, torso, and pelvis under the litter-board condition.

4.5 Discussion

The dynamic model proposed in this work presents a new framework for the inclusion of the coupling effect between individual body segments in supine human modeling. The model also presents a practical approach to combining the supine human model with different types of transport systems, where the human model parameters are defined in front, and the optimization process works to characterize the parameters of different transport systems.

The inclusion of the coupling effect between the adjacent segments enabled the model to capture the effect between neighboring segments. For example, for the litter-board case, the head showed a peak at 5 Hz in places where the torso showed maximum peak, indicating that the 5 Hz on the head is related to the torso resonance. Such findings would make the proposed model a useful tool for vibration-suppression designers to gain more insight on supine-human response.

Still, several assumptions were used in the parameter estimation of the model that may impose some limitations on the applicability of the model. First, each body segment was considered as rigid, which could be reasonable for the head but not for the rest of the body segments. Second, the contact points between the body segments and the rigid platform were assumed to have no motion in the motion platform fore-aft direction, and that may generate some errors in cases where considerable platform fore-aft motion exists. Third, the current study assumed linear contact elements between the human and the spinal board and between the spinal board and the litter, which may not be true for cases where material nonlinearity is strong. In these cases, nonlinear elements may provide more realistic representations of these areas.

The current study showed that the head has resonance frequencies different than those presented by Vogt, Mertens et al. (1978) who indicated that the head has a resonance of 63 Hz. The discrepancy resulted because a rubber pad was placed underneath the head in the current study, and therefore the head showed a peak around 17

Hz for the rigid case and peaks around 6 Hz and 11 Hz for the litter-board case. In general, the torso peak frequencies of this work are consistent with those presented by Huang and Griffin (2008, 2009).

CHAPTER V

BIODYNAMIC RESPONSE OF THE SUPINE HUMAN BODY DURING WHOLE–BODY VIBRATION IN 3D

5.1 Introduction

The objective of this chapter is to introduce 3 D supine-human models that can predict motion in response to 3 D WBV with two different support conditions, rigid and litter-board.

This chapter is organized into eight sections. After this brief introduction, Section 5.2 introduces the experiment and participants. In Section 5.3, the biodynamic measurement is illustrated. This section mainly deals with the geometric measurement for experiments and later models. The experimental results are demonstrated in Section 5.4. After that, a 3 D supine model is proposed under a rigid support condition in Section 5.5. This model is the primary model for 3 D supine human modeling. Then a secondary model is proposed. In Section 5.6, the results are demonstrated compared with experimental testing. The discussions and conclusions are presented in Sections 5.7 and 5.8.

5.2 Methods

5.2.1 Participants

Eight healthy male subjects participated in this study. The participants had a mean age of 23 ± 3.16 years, a mean weight of 81±14.98 kg, and a mean height of 182 ± 8.36 cm. The participants had no history of muscle-based disorders or injury. The study was approved by the University of Iowa IRB for human subject studies, and an informed consent was obtained for each participant prior to the study. The data from seven participants were used in the parameter identification of the system, while anthropometric

and response data from the eighth subject were selected for testing and validating the dynamic model response under WBV.

5.2.2 Experiments

A six-DOF Moog-FCS 628-1800 electrical motion platform system was used in this work to generate random vibration files of 0.5 m/s^2 (RMS) in each direction, x, y, and z, applied at the platform level. It is worthy to mention that all the experiments satisfy the standards (Standardization, 1998; Standardization, 2004; Standardization, 2010). The PSD (Newland, 1984) across the bandwidth of 0.5-20 Hz was approximately flat for each file. All files represented a different random vibration time history of 60 sec in length. Two experimental conditions were conducted on the participants. In the first condition, called the rigid case, the participants were lying down and strapped to the rigid motion platform (Figure 45.a) with straps over the shoulders, chest, pelvis, mid-thigh, and mid-shank. In the second condition, called the litter-board case, the participants first lay down and were strapped to a long spinal-board (Spine Board 50-013, North American Rescue, Greer, SC) in a similar manner to the rigid case. Then the human and board were strapped together to a standard military litter (Talon II Model 90C Litter, North American Rescue, Greer, SC), rigidly attached to the motion platform, using straps on the chest and mid-thigh (Figure 45b). The output displacement and accelerations at the surfaces of the head (at the forehead), torso (at the sternum), and pelvis were measured using a Vicon motion capture system (Rahmatalla and DeShaw, 2011) and inertial sensors (DeShaw and Rahmatalla, 2012).

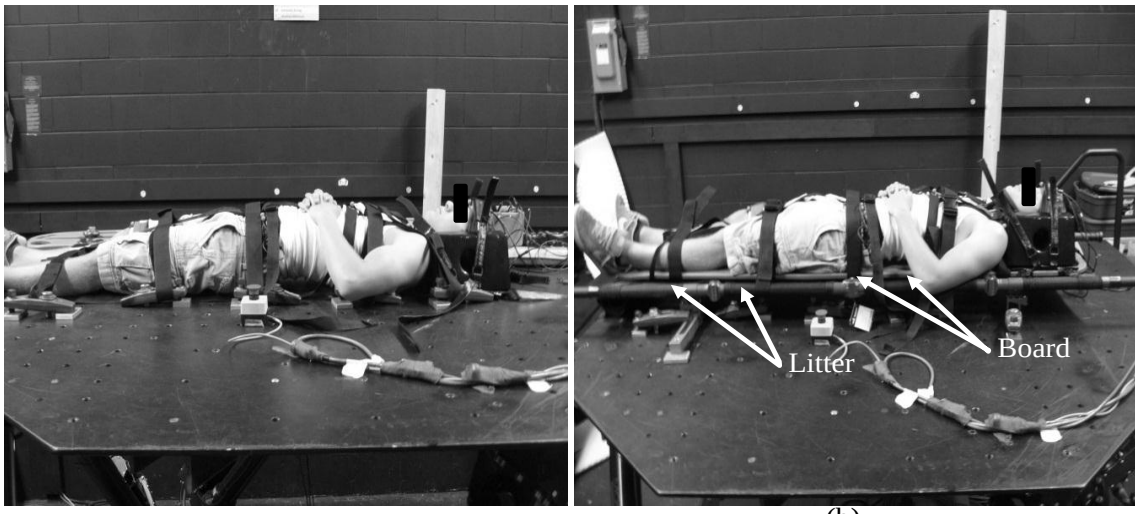

(a) (b)

Figure 45:Supine subjects testing on the two different supporting conditions (a) A supine subject lying on a rigid platform, (b) a supine subject lying on a board litter system with the latter attached firmly to the motion platform.

5.3 Biodynamic Measure

The experimental MIMO transmissibility $\boldsymbol{H}^{e}(f)$ is defined in this work as the complex ratio between the output acceleration measurement by $\ddot{\boldsymbol{x}}_{\boldsymbol{e}} = \{\ddot{x}_1^e, \ddot{y}_1^e, \ddot{z}_1^e, \ddot{x}_2^e, \ddot{y}_2^e, \ddot{z}_2^e, \ddot{x}_3^e, \ddot{y}_2^e, \ddot{z}_2^e\}^T$ at the segment levels and the input tri-axis acceleration ($\boldsymbol{x_o}^{\boldsymbol{T}} = \{\ddot{x}_o, \ddot{y}_o, \ddot{z}_o\}$) measured at the shaker's rigid-platform level . $\{\ddot{x}_1^e, \ddot{y}_1^e, \ddot{z}_1^e\}$ are the coordinates of the head measured at $\mathbf{E_1}$ (Figure 48), $\{\ddot{x}_2^E, \ddot{y}_2^E, \ddot{z}_2^E\}$ represent the coordinates of the torso measured at $\mathbf{E_2}$, and $\{\ddot{x}_3^E, \ddot{y}_3^E, \ddot{z}_3^E\}$ are the coordinates of the pelvis measured at $\mathbf{E_3}$.

The geometric mean ($H_{ij}^{g}(f)$) is used in this work to calculate the geometric mean transmissibility of seven subjects (Eq. (5. 1)). Previous work has shown that H_{ij}^{g} reduces the effects of noise corruption and gives an unbiased estimation of the transfer function better than the arithmetic mean (Mathworks, 2010). i is a counter representing the directions of the measured output-acceleration on the human body segments (i =1,2, and 3 for head, i =4,5, and 6 for torso, i =7, 8, and 9 for pelvis,). j represents the directions of input signal (j =1 for x axis, j =2 for y axis and j =3 for z axis).

$$H_{ij}^{g}(f) = \prod_{k=1}^{n} \sqrt[n]{\left[H_{ij}{}^{e}(f)\right]_{k}} \tag{5.1}$$

where k is a counter ($k = 1 \rightarrow n$) and n is the number of subjects.

5.4 Experimental Results

5.4.1 Rigid Case

The magnitude of the experimental transmissibilities of seven tested subjects under the rigid-support case (gray lines in Figure 46) showed observable subject inter-variability, especially at the first peak and after that. The transmissibility graphs shows 27 components, with each segment having nine components representing the relationship between three inputs and 3 outputs at the area of accelerometers. When it comes to the z direction input and output, for each segment, the resonant frequency is not very clear. Among the non-diagonal transmissibility, the head transmissibility in the x direction in response to input z direction ($H_{13}{}^{g}$) showed a large magnitude after about 9 Hz compared to the other transmissibility components. The geometric mean transmissibility of seven subjects is shown in the black solid lines in Figure 46.

5.4.2 Litter-board Case

For the litter-board case, the magnitudes of the x direction input and output are greater than the magnitudes of the rigid case except H_{41}. Different from the rigid case when the input and the output are both in the z direction, Figure 47 shows significant resonance frequencies. For the head, $H_{33}{}^{g}$ shows two peaks at frequency 5.13 Hz and 10.8 Hz with magnitude 1.8 and 2.045, respectively. For the sternum, the peak frequency of $H_{63}{}^{g}$ is 5.25 with magnitude 3.52. For the pelvis, the peak frequency is 5.03 Hz with magnitude 3.51.

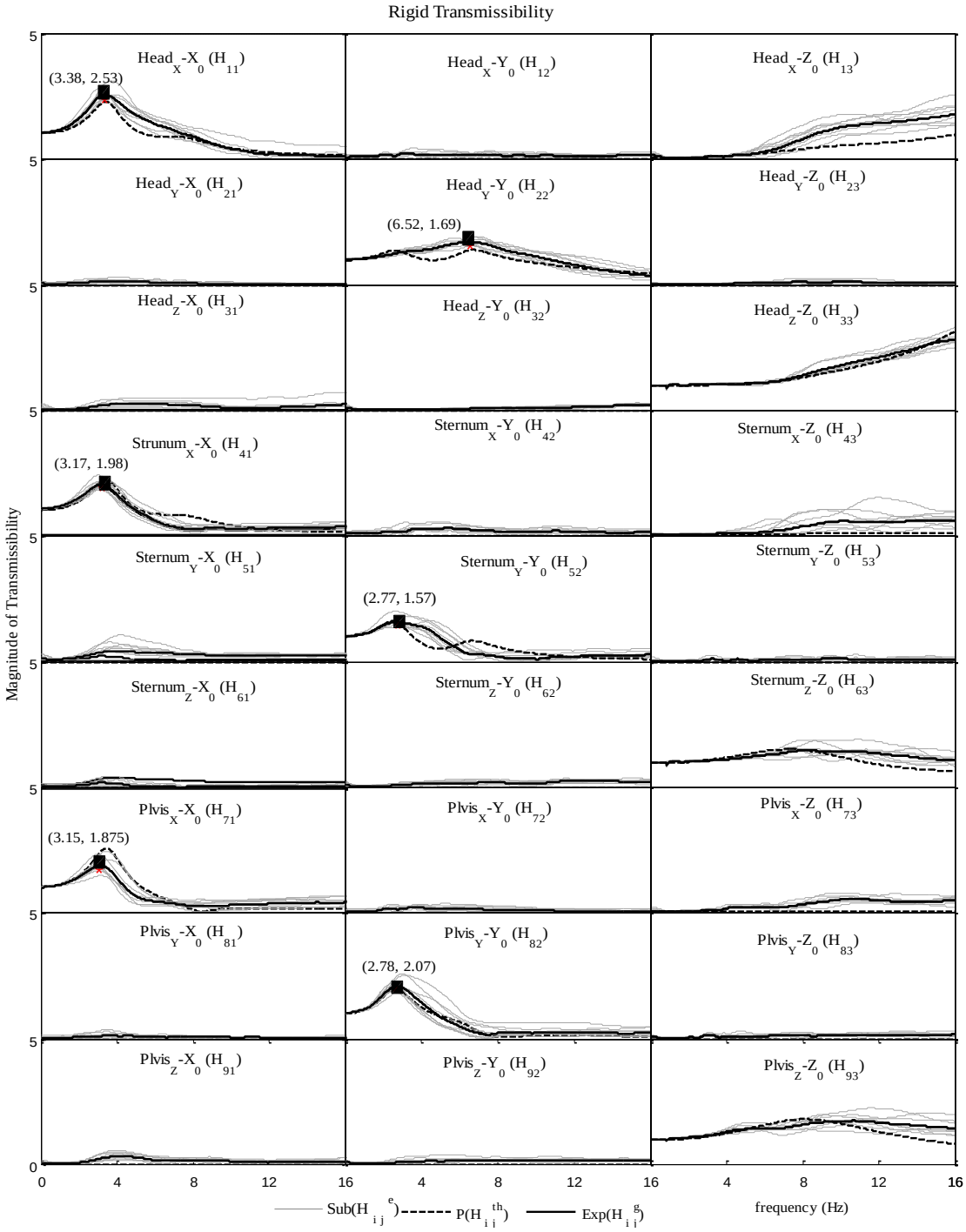

Figure 46: Transmissibility of rigid case. Gray line is the subjective experimental results; black solid line is the 8th subjective experimental result; the dashed black line is the predictive theoretical results based on the mass and weight of the 8th subject.

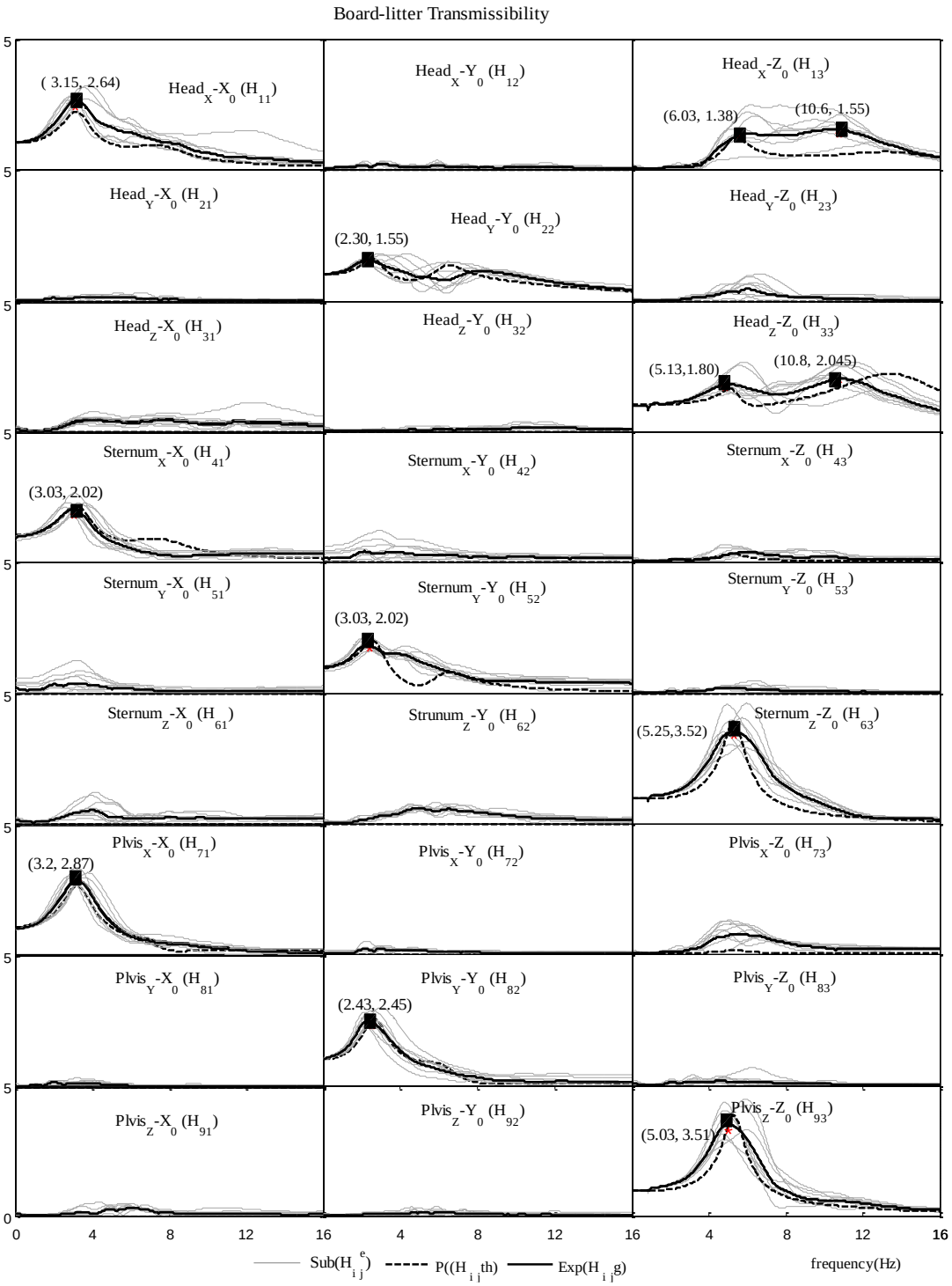

Figure 47: Transmissibility of litter-board case. Gray line is the subjective experimental results; black solid line is the 8th subjective experimental result; the dashed black line is the predictive theortical results based on the mass and weight of the 8th subject.

5.5 Modeling

5.5.1 Rigid Case

5.5.1.1 Geometric description

Figure 48 shows a schematic representation of the proposed supine human model and the underlying support for the rigid-case condition. The human is modeled with three segments: the head (spherical segment), representing the head and neck with a center at position $\mathbf{F}_1$; the torso (ellipsoid segment), representing the thorax, abdomen, and arms with a center at position $\mathbf{F}_2$, and the pelvis (ellipsoid segment), representing the hips and legs, with a center at position $\mathbf{F}_3$. The position of the segment's centers is expressed as

$$\mathbf{F}_m = \begin{Bmatrix} x_m \\ y_m \\ z_m \end{Bmatrix} \tag{5.2}$$

with *m*=1 for the head, *m*=2 for the torso, and *m*=3 for the pelvis. Due to the difficulty of experimentally measuring the motion of the center of each segment directly, the position and acceleration of selected points on the surfaces of the head ($\mathbf{E}_1$) (forehead), torso ($\mathbf{E}_2$) (sternum), and pelvis ($\mathbf{E}_3$) were measured and then transformed to the segment centers. The position of the experimental accelerometers can be expressed as

$$\mathbf{E}_m = \begin{Bmatrix} x_m^e \\ y_m^e \\ z_m^e \end{Bmatrix} \tag{5.3}$$

The relationship between the position of the center of the segment ($\mathbf{F}_m$) and the experimental (testing) position ($\mathbf{E}_m$) on each segment can be expressed using the following transformation:

$$\mathbf{F_m} = \mathbf{E}_m - \mathbf{A}\mathbf{T}_m\mathbf{P}_m^e \tag{5.4}$$

where $\mathbf{A} = \begin{bmatrix} 1 & 0 & 0 & 0 \\ 0 & 1 & 0 & 0 \\ 0 & 0 & 1 & 0 \end{bmatrix}$.

$$\mathbf{P}_m^e = \begin{Bmatrix} P_{mx}^e \\ P_{my}^e \\ P_{mz}^e \end{Bmatrix} \tag{5.5}$$

$\mathbf{P}_m^e$ is the Cartesian distance between the center of the segment and the location of the sensors on the mth segment. The transformation matrix T_m, based on the DH method (Denavit and Hartenberg, 1955), can be obtained using Eq. (5.6).

$$\mathbf{T}_m = \prod_{j=1}^{3} \mathbf{T}_m^j \tag{5.6}$$

$$\mathbf{T}_j^m = \begin{bmatrix} \cos\theta_{mj} & -\cos\alpha_j \sin\theta_{mj} & \sin\alpha_j \sin\theta_{mj} & a_j \cos\theta_{mj} \\ \sin\theta_{mj} & \cos\alpha_j \cos\theta_{mj} & -\sin\alpha_j \cos\theta_{mj} & a_j \sin\theta_{mj} \\ 0 & \sin\alpha_j & \cos\alpha_j & d_j \\ 0 & 0 & 0 & 1 \end{bmatrix} \tag{5.7}$$

where j is the number of rotational DOF of the m^{th} segment (shown in Table 16) and $\mathbf{T}_m^j$ is the transformation matrix between adjacent rotational DOF for the m^{th} segment. $\mathbf{T}_m^j$ is represented by the four parameters $\theta_{mj}, d_{mj}, \alpha_{mj}$ and a_{mj} in Eq. (5.7) (Denavit and Hartenberg, 1955).

Table 16: DH table for one-link 3D model

Joint Number(m)	θ	d	α	a
1	$90^o + \theta_{mz}$	0	90^o	0
2	$90^o + \theta_{mx}$	0	90^o	0
3	$90^o + \theta_{my}$	0	90^o	0

The head, torso, and pelvis are connected via rotational and translational joints $\mathbf{J}_1$ and $\mathbf{J}_2$. $\mathbf{J}_1$ represents the joint between the head and torso, and $\mathbf{J}_2$ represents the joint between the torso and pelvis. $\mathbf{J}_1$ includes two positions: $\mathbf{J}_1^1$ represents the location of $\mathbf{J}_1$on the head side, and $\mathbf{J}_1^2$ represents the location of $\mathbf{J}_1$ on the torso side. Similarly, $\mathbf{J}_2$ has two components: $\mathbf{J}_2^2$ represents the location of $\mathbf{J}_2$on the torso side, and $\mathbf{J}_2^3$ represents the location of $\mathbf{J}_2$ on the pelvis side. The Cartesian components of the position of each joint can be represented as

$$\mathbf{J}_o^m = \begin{Bmatrix} J_{ox}^m \\ J_{oy}^m \\ J_{oz}^m \end{Bmatrix} \tag{5.8}$$

where o is the joint's number, o=1, 2. The vectors from the center of each segment $\mathbf{F}_m$ to the connection joint $\mathbf{J}_o^m$ between two body segments are

$$\mathbf{L}_{bs} = \begin{Bmatrix} L_{bsx} \\ L_{bsy} \\ L_{bsz} \end{Bmatrix} \tag{5.9}$$

$$\mathbf{L}_{at} = \begin{Bmatrix} L_{atx} \\ L_{aty} \\ L_{atz} \end{Bmatrix} \tag{5.10}$$

where s=1, 2 and t =2, 3. The position of $\mathbf{J}_o^m$ can be found using the following transformation:

$$\begin{aligned} \mathbf{J_1^1} &= \mathbf{F_1} + \mathbf{AT_1 L_{b1}} \\ \mathbf{J_1^2} &= \mathbf{F_2} + \mathbf{AT_2 L_{a2}} \\ \mathbf{J_2^2} &= \mathbf{F_2} + \mathbf{AT_2 L_{b2}} \\ \mathbf{J_2^3} &= \mathbf{F_3} + \mathbf{AT_3 L_{a3}} \end{aligned} \tag{5.11}$$

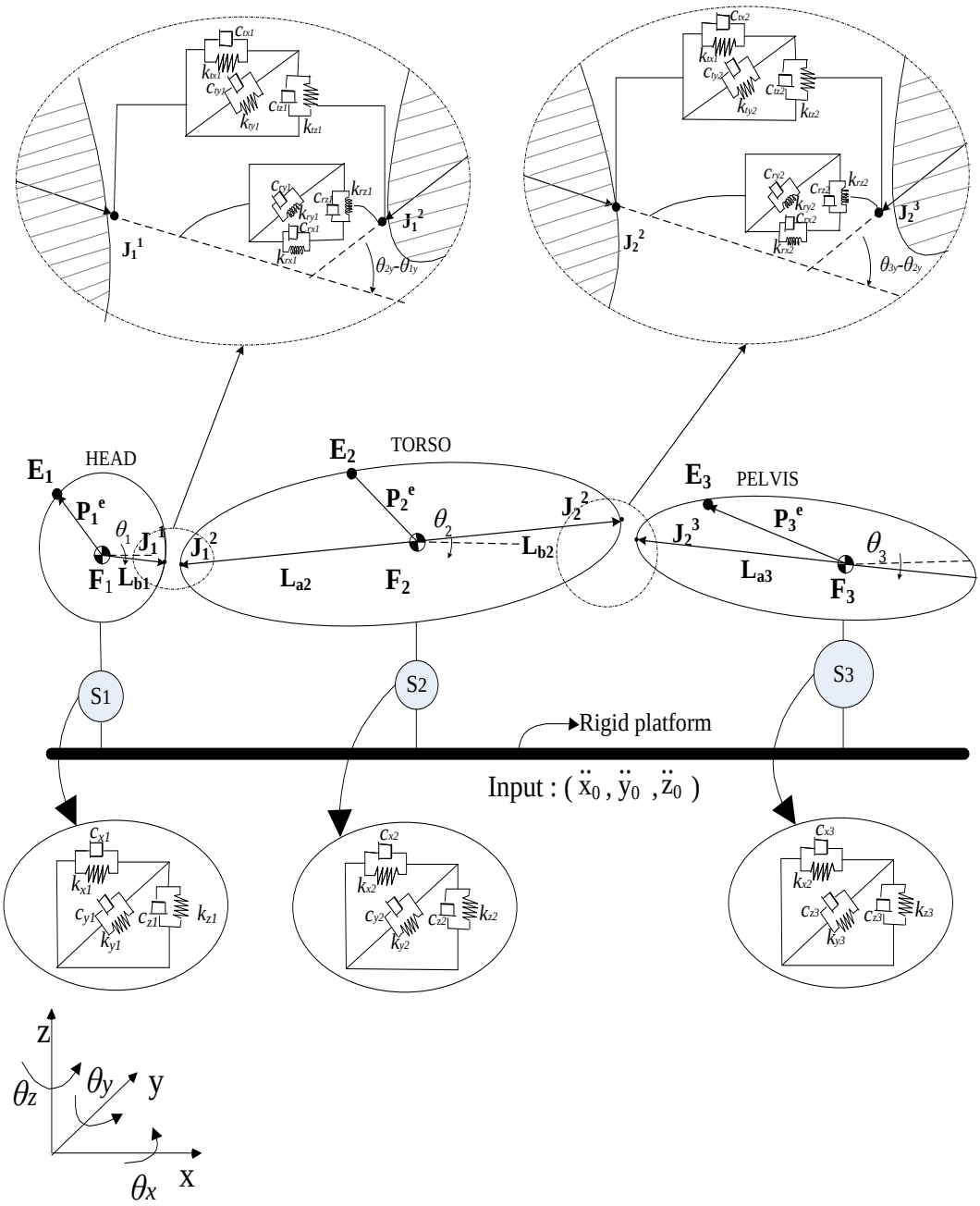

Figure 48: 3 D supine human model based on rigid case.

5.5.1.2 Dynamic Equation

In Figure 48, $\{\ddot{x}_0, \ddot{y}_0, \ddot{z}_0\}$ represents the x, y, and z directions of the input platform random accelerations. $\{\ddot{x}_1, \ddot{y}_1, \ddot{z}_1\}$, $\{\ddot{x}_2, \ddot{y}_2, \ddot{z}_2\}$, and $\{\ddot{x}_3, \ddot{y}_3, \ddot{z}_3\}$ represent the linear acceleration of the geometric center of the head (at $\mathbf{F}_1$), torso (at $\mathbf{F}_2$), and pelvis (at $\mathbf{F}_3$), respectively. The proposed supine-human model has 18 DOFs with $\{x_m, y_m, z_m\}$ $(m = 1,2,3)$ representing the translational motion of the head, torso, and pelvis respectively, and $\boldsymbol{\theta}_m = \{\theta_{xm}, \theta_{ym}, \theta_{zm}\}$ representing the rotation motion about x, y, and z axes of the m^{th} segments (head, torso, and pelvis). The segments have a mass m_m and a moment of inertia I_m. The basic mass and inertia information of the human body segments were obtained from the literature (Dempster and Gaughran, 1967; Winter, 1979; Winter, 2005)and were based on the ratio of the segment mass relative to that of the total body mass. Table 12 shows the mass and length of each segment.

The stiffness and damping characteristics of the vertebras, ligaments, tendons, and muscles at each joint are modeled as translational and rotational spring and damper elements and were lumped between the adjacent segments at joint $\mathbf{J}_o^m$. The translational stiffness components at joints $\mathbf{J}_1$ and $\mathbf{J}_2$ are represented by $\mathbf{k}_{t1} = diag\{k_{tx1}, k_{ty1}, k_{tz1}\}$ and $\mathbf{k}_{t2} = diag\{k_{tx2}, k_{ty2}, k_{tz2}\}$, respectively, and the rotational stiffness components are represented by $\mathbf{k}_{r1} = diag\{k_{rx1}, k_{ry1}, k_{rz1}\}$ and $\mathbf{k}_{r2} = diag\{k_{rx2}, k_{ry2}, k_{rz2}\}$, respectively. The translational damping components are represented by $\mathbf{c}_{t1} = diag\{c_{tx1}, c_{ty1}, c_{tz1}\}$ and $\mathbf{c}_{t2} = diag\{c_{tx2}, c_{ty2}, c_{tz2}\}$, and the rotational damping components by $\mathbf{c}_{r1} = diag\{c_{rx1}, c_{ry1}, c_{rz1}\}$ and $\mathbf{c}_{r2} = diag\{c_{rx2}, c_{ry2}, c_{rz2}\}$. The contact points between the body segments and the underlying rigid support are represented by springs with coefficient $\mathbf{k}_m = diag\{k_{xm}, k_{ym}, k_{zm}\}$, and dampers with coefficients $\mathbf{c}_m = diag\{c_{xm}, c_{ym}, c_{zm}\}$. $\mathbf{k}_m$ and $\mathbf{c}_m$ represent the human muscle and tissue at the area connecting to the right platform.

The joint forces are produced by the translation motion in the 3-axis direction (Eq. (5.12) and (5.13)) and the rotation motion (Eq. (5.14) and (5.15)) about the 3-axis.

$$\mathbf{f}_{\mathbf{J}1} = \mathbf{k}_{t1}\boldsymbol{l}_{12} + \mathbf{c}_{t1}\dot{\boldsymbol{l}}_{12} \tag{5.12}$$

$$\mathbf{f}_{\mathbf{J}2} = \mathbf{k}_{t2}\boldsymbol{l}_{23} + \mathbf{c}_{t2}\dot{\boldsymbol{l}}_{23} \tag{5.13}$$

$$\mathbf{m}_{\mathbf{J}1} = \mathbf{k}_{r1}(\boldsymbol{\theta}_2 - \boldsymbol{\theta}_1) + \mathbf{c}_{r1}(\dot{\boldsymbol{\theta}}_2 - \dot{\boldsymbol{\theta}}_1) \tag{5.14}$$

$$\boldsymbol{m}_{\mathbf{J}2} = \mathbf{k}_{r2}(\boldsymbol{\theta}_3 - \boldsymbol{\theta}_2) + \boldsymbol{c}_{r2}(\dot{\boldsymbol{\theta}}_3 - \dot{\boldsymbol{\theta}}_2) \tag{5.15}$$

where $\boldsymbol{l}_{12} = [l_{12\mathrm{x}} \quad l_{12\mathrm{y}} \quad l_{12\mathrm{z}}]^T$ presents the displacement between joints $\mathbf{J}_1^2$ and $\mathbf{J}_\mathbf{1}^\mathbf{1}$, and $\boldsymbol{l}_{32} = [l_{32\mathrm{x}} \quad l_{32\mathrm{y}} \quad l_{32\mathrm{z}}]^T$ represents the displacement between joints $\mathbf{J}_2^3$ and $\mathbf{J}_2^2$. The equations for $\boldsymbol{l}_{12}$ and $\boldsymbol{l}_{32}$ are shown in Eqs. (5.16) and (5.17).

$$\boldsymbol{l}_{12} = \mathbf{J}_1^2 - \mathbf{J}_1^1 = \mathbf{F}_2 + \mathbf{A}\mathbf{T}_2\mathbf{L}_{a2} - \mathbf{F}_1 - \mathbf{A}\mathbf{T}_1\mathbf{L}_{b1} \tag{5.16}$$

$$\mathbf{l}_{32} = \mathbf{J}_2^3 - \mathbf{J}_2^2 = \mathbf{F}_3 + \mathrm{A}\mathbf{T}_3\mathbf{L}_{a3} - \mathbf{F}_2 - \mathbf{A}\mathbf{T}_2\mathbf{L}_{b2} \tag{5.17}$$

The contract forces ($\boldsymbol{f}_{cm} = [f_{cmx} \quad f_{cmy} \quad f_{cmz}]^T$) between each segment and the rigid platform is shown in Eq. (5.18).

$$\boldsymbol{f}_{cm} = \mathbf{k}_m(\mathbf{F}_m - \mathbf{x_0}) + \mathbf{c}_m(\dot{\mathbf{F}}_m - \dot{\mathbf{x}}_\mathbf{0}) \tag{5.18}$$

The dynamic equation for the dynamic model is derived using the Lagrangian equation and is as follows:

$$\boldsymbol{\tau} = \frac{d}{dt}\left(\frac{\partial L}{\partial \dot{\mathbf{x}}}\right) - \frac{\partial L}{\partial \mathbf{x}} + \frac{\partial D}{\partial \dot{\mathbf{x}}} \tag{5.19}$$

where L is the Lagrangian $L = T - V$, T is the kinetic energy, V is the potential energy, and D is the dissipation energy.

$$T = \sum_{m=1}^{3}\left(\frac{1}{2}\dot{\boldsymbol{\theta}}_m{}^T\mathbf{I}_m\dot{\boldsymbol{\theta}}_m + \frac{1}{2}\dot{\mathbf{x}}_m{}^T\boldsymbol{m}_m\dot{\mathbf{x}}_m\right) \tag{5.20}$$

where $\mathbf{I}_m = diag\{I_{mx},\ I_{my},\ I_{mz}\}$ and $\boldsymbol{m}_m = diag\{m_{mx},\ m_{my},\ m_{mz}\}$

$$V = \sum_{m=1}^{3}\left[\frac{1}{2}(\mathbf{C}_m - \mathbf{x}_0)^T\mathbf{k}_m(\mathbf{C}_m - \mathbf{x}_0) + \frac{1}{2}m_m g z_m\right] + \sum_{n=1}^{2}\left[\frac{1}{2}\boldsymbol{l}_{12}{}^T\mathbf{k}_{tn}\boldsymbol{l}_{12} + \frac{1}{2}(\boldsymbol{\theta}_{n+1} - \boldsymbol{\theta}_n)^T\mathbf{k}_{rn}(\boldsymbol{\theta}_{n+1} - \boldsymbol{\theta}_n)\right] \tag{5.21}$$

$$D = \sum_{m=1}^{3}\left[\frac{1}{2}(\dot{\mathbf{C}}_m - \dot{\mathbf{x}}_0)^T\mathbf{c}_m(\dot{\mathbf{C}}_m - \dot{\mathbf{x}}_0)^2(\dot{\mathbf{C}}_m - \dot{\mathbf{x}}_0)\right] + \sum_{n=1}^{2}\left[\frac{1}{2}\dot{\boldsymbol{l}}_{12}{}^T\mathbf{c}_{tn}\dot{\boldsymbol{l}}_{12} + \frac{1}{2}(\dot{\boldsymbol{\theta}}_{n+1} - \dot{\boldsymbol{\theta}}_n)^T\mathbf{c}_{rn}(\dot{\boldsymbol{\theta}}_{n+1} - \dot{\boldsymbol{\theta}}_n)\right] \tag{5.22}$$

A linear expression of the dynamic Eq. (5.23) is derived by taking the Taylor's series first expansion at the equilibrium state $\hat{\mathbf{x}} = \{x_{1o},\ y_{1o},\ z_{1o}, \theta_{1xo},\ \theta_{1yo},\ \theta_{1zo},\ x_{2o},$

$y_{2o},\ z_{2o}, \theta_{2xo},\ \theta_{2yo},\ \theta_{2zo},\ x_{3o},\ y_{3o},\ z_{3o}, \theta_{3xo}, \theta_{3yo}, \theta_{3zo}\}^{\mathrm{T}}$. $\hat{\mathbf{x}}$ is also the initial position of $\mathbf{x} = \{x_1,\ y_1,\ z_1, \theta_{1x},\ \theta_{1y},\ \theta_{1z},\ x_2,\ y_2,\ z_2, \theta_{2x},\ \theta_{2y},\ \theta_{2z},\ x_3,\ y_3,\ z_3, \theta_{3x}, \theta_{3y}, \theta_{3z}\}^{\mathrm{T}}$. $\mathbf{x}_0 = \{\ddot{\mathrm{x}}_0, \ddot{\mathrm{y}}_0, \ddot{\mathrm{z}}_0\}^T$ is the input acceleration signal.

$$\mathbf{M}\ddot{\mathbf{x}} + \mathbf{C}\dot{\mathbf{x}} + \mathbf{K}\mathbf{x} = \boldsymbol{\alpha}_{\mathrm{k}}\mathbf{x}_0 + \boldsymbol{\alpha}_{\mathrm{c}}\dot{\mathbf{x}}_0 \tag{5.23}$$

where $\mathbf{M} = \frac{\partial(\boldsymbol{\tau})}{\partial \ddot{\mathbf{x}}}\Big|_{\mathbf{x}=\hat{\mathbf{x}}}$, $\mathbf{M}$ is a diagonal matrix of (m_1, m_1, m_1, I_{1x}, I_{1y}, I_{1z}, m_2, m_2, m_2, I_{2x}, I_{2y}, I_{2z}, m_3, m_3, m_3, I_{3x}, I_{3y}, I_{3z}), $\mathbf{C} = \frac{\partial(\boldsymbol{\tau})}{\partial \dot{\mathbf{x}}}\Big|_{\mathbf{x}=\hat{\mathbf{x}}}$; and $\mathbf{K} = \frac{\partial(\boldsymbol{\tau})}{\partial \mathbf{x}}\Big|_{\mathbf{x}=\mathbf{x_0}}$. The details of equation of $\mathbf{K}$, $\mathbf{C}$, $\boldsymbol{\alpha}_{\mathbf{k}}$, and $\boldsymbol{\alpha}_{\mathbf{c}}$ are shown in Appendix C.

The theoretical transmissibility ($\mathbf{H}^{th}(f)$) between the output acceleration at the testing locations and the input 3D acceleration is demonstrated in Eq. (5. 24) (Cho and Yoon, 2001). In this equation, matrix $\mathbf{R}$ (also shown in Appendix C) represents the transformation between the accelerations at the segment surface and the center of each segment. The linearized form of $\mathbf{R}$ in Eq. (5.24) is shown in the appendix.

$$\mathbf{H}^{th} = \mathbf{R}\mathbf{H} = \mathbf{R}(\mathbf{M}s^2 + \mathbf{C}s + \mathbf{K})^{-1}(\boldsymbol{\alpha}_{\mathrm{k}} + \boldsymbol{\alpha}_{\mathrm{c}}s) \tag{5.24}$$

where $\ddot{\mathbf{X}}_{\boldsymbol{e}}$, $\ddot{\boldsymbol{X}}_0$ and $\ddot{\mathbf{X}}$ are the Laplace transformation of $\ddot{\boldsymbol{x}}_{\mathbf{e}}$, $\ddot{\boldsymbol{x}}_0$ and $\ddot{\boldsymbol{x}}$

5.5.1.3 System Identification

The unknown biomechanical model's parameters are the translational and rotational spring and damping coefficients at each joint and the contact spring and damping coefficients between the body segments and the rigid platform. These unknown parameters are identified by matching the magnitude and phase of the theoretical transmissibility ($\mathbf{H}^{th}(f)$) and the experimental magnitude and phase of the geometrical transmissibility ($\mathbf{H}^{g}(f)$). Optimization schemes (Mathworks, 2010) are used to identify the system parameters. The design variables of the optimization problem are the unknown parameters $\mathbf{x}^{\boldsymbol{r}}$.

$$\mathbf{x}^r = \{x_1, x_2, \dots, x_{42}\}^T = [k_{x1}, k_{x2}, k_{x3}, k_{y1}, k_{y2}, k_{y3}, k_{z1}, k_{z2}, k_{z3}, k_{tx1}, k_{tx2}, k_{ty1}, k_{ty2}, k_{tz1}, k_{tz2}, k_{rx1}, k_{rx2}, k_{ry1}, k_{ry2}, k_{rz1}, k_{rz2}, c_{x1}, c_{x2}, c_{x3}, c_{y1}, c_{y2}, c_{y3}, c_{z1}, c_{z2}, c_{z3}, c_{tx1}, c_{tx2}, c_{ty1}, c_{ty2}, c_{tz1}, c_{tz2}, c_{rx1}, c_{rx2}, c_{ry1}, c_{ry2}, c_{rz1}, c_{rz2},]^T \tag{5.25}$$

The objective function f^{obj} shown in Eq. (5.26) represents the normalized differences between the predicted and experimental magnitude and phase of the transmissibility.

$$f^{obj} = \sum_f \left\{ \frac{|\boldsymbol{H}^{th}(f)| - |\boldsymbol{H}^{g}(f)|}{\|\|\boldsymbol{H}^{th}(f)| - |\boldsymbol{H}^{g}(f)|\|} \right\}^2 + \sum_f \left\{ \frac{Pha\left(\boldsymbol{H}^{th}(f)\right) - Pha\left(\boldsymbol{H}^{g}(f)\right)}{\left\|Pha\left(\boldsymbol{H}^{th}(f)\right) - Pha\left(\boldsymbol{H}^{g}(f)\right)\right\|} \right\}^2 \tag{5.26}$$

where $|.|$ represents the magnitude of transmissibility, and $Pha(.)$ represents the phase of the transmissibility. In Figure 46 and Figure 47, it is obvious that for both the rigid and litter-board cases, the non-diagonal subjects' magnitude of transmissibility and geometrical mean magnitude of transmissibilities (except H_{13}, H_{43} and H_{73}) are very close to zero. Thus, only diagonal transmissibilities and H_{13}, H_{43} and H_{73} are considered in the optimization process with a total of 12 transmissibilities.

The upper boundary limits on the design variables are considered as $\mathbf{UB}^r$:

$$\mathbf{UB}^r = \{\underbrace{1000000, \cdots, 1000000}_{42\ components}\}^T \tag{5.27}$$

The lower boundary limits are considered as $\mathbf{LB}^r$:

$$\mathbf{LB}^r = \{\underbrace{1, \cdots, 1}_{21\ componenets}, \underbrace{0.001, \cdots, 0.001}_{21\ componenets}\}^T \tag{5.28}$$

The starting points for the design variables are denoted as:

$$\mathbf{x_0}^r = \{\underbrace{1, \cdots, 1}_{42\ components}\} \tag{5.29}$$

The frequency (f) in Eq. (5.26) is considered from 0 Hz to 20 Hz. The nonlinear least square method with the trust region reflective algorithm is used to solve the

nonlinear minimization problem. The optimization calculations are conducted inside MATLAB. The variable tolerance and objective tolerance are both 1.0e-6. The basic optimization process is illustrated in Figure 49.

5.5.2 Litter-board Case

The geometric description of the dynamic model of the litter-board case is similar to the rigid case (Figure 46), but with the addition of the litter-board springs $\boldsymbol{k}_{bm}$and dampers $\boldsymbol{c}_{bm}$ in series with $\mathbf{c}_m$ and $\boldsymbol{k}_m$. In the litter-board model, the board and litter are modeled as linear translate springs and dampers represented by $\boldsymbol{k}_{bm}$ and $\boldsymbol{c}_{bm}$.

$$\boldsymbol{k}_{bm} = \begin{bmatrix} k_{bxm} \\ k_{bym} \\ k_{bzm} \end{bmatrix} \tag{5.30}$$

$$\boldsymbol{c}_{bm} = \begin{bmatrix} c_{bxm} \\ c_{bym} \\ c_{bzm} \end{bmatrix} \tag{5.31}$$

The total contact forces between the human segments and the litter-board are lumped and presented (Boileau and Rakheja, 1998; Cho and Yoon, 2001) as:

$$\boldsymbol{f}_{cm} = \frac{\boldsymbol{k}_m\, \boldsymbol{k}_{bm}}{\boldsymbol{k}_m + \boldsymbol{k}_{bm}}(\mathbf{C}_m - \mathbf{x}_0) + \frac{\boldsymbol{c}_m\, \boldsymbol{c}_{bm}}{\boldsymbol{c}_m + \boldsymbol{c}_{bm}}(\dot{\mathbf{C}}_m - \dot{\mathbf{x}}_0)$$

$$\boldsymbol{f}_{cm} = \boldsymbol{k}_m^{eq}(\mathbf{C}_m - \mathbf{x}_0) + \boldsymbol{c}_m^{eq}(\dot{\mathbf{C}}_m - \dot{\mathbf{x}}_0) \tag{5.32}$$

where $\boldsymbol{k}_m^{eq} = \boldsymbol{\mu}_m{}^k\, \boldsymbol{k}_m$ and $\boldsymbol{c}_m^{eq} = \boldsymbol{\mu}_m{}^c\, \boldsymbol{c}_m$;

$$\boldsymbol{\mu}_m{}^c = \begin{bmatrix} \mu_{mx}{}^c \\ \mu_{my}{}^c \\ \mu_{mz}{}^c \end{bmatrix} \tag{5.33}$$

$$\boldsymbol{\mu}_m{}^k = \begin{bmatrix} \mu_{mx}{}^k \\ \mu_{my}{}^k \\ \mu_{mz}{}^k \end{bmatrix} \tag{5.34}$$

$\boldsymbol{\mu}_m{}^c$ and $\boldsymbol{\mu}_m{}^k$ are the litter-board damping coefficients and litter-board softening coefficients. When $\mu_{mj}{}^c$ or $\mu_{mj}{}^k = 1$ $j = 1,2, or\ 3 (x, y\ and\ z)$; $m = 1, 2\ or\ 3$ physically means that the litter-board damper coefficient and spring stiffness

coefficients are equal to infinite. The effects are exactly the same with only rigid case. When $\mu_{mj}{}^{c}$ *or* $\mu_{mj}{}^{k} = 0$ physically means that the litter-board damper coefficient and spring stiffness coefficients are equal to zero.

The supine-human parameters are considered to be similar to those of the rigid-case condition. The equivalent parameters of $\boldsymbol{\mu}_m{}^{k}$ and $\boldsymbol{c}_m^{eq}$ are characterized based on optimization schemes similar to those used for the rigid case. The objective function form is similar to the rigid-case model (Eq. (5. 26)). The design variables of the optimization are ($\mathbf{x}^{\boldsymbol{l}}$) as shown in Eq. (5. 25). Other parameters in Eq. (5. 25), including $\boldsymbol{k}_m$, $\boldsymbol{c}_m$,$\mathbf{c}_{tm}$, $\mathbf{c}_{rm}$, $\mathbf{k}_{tm}$, and $\mathbf{k}_{rm}$, have been optimized in the process of rigid case.

$$\mathbf{x}^{\boldsymbol{l}} = \{x_1, x_2, \dots, x_{18}\}^T = \{\mu_{1x}{}^{k},\ \mu_{1y}{}^{k},\ \mu_{1z}{}^{k}, \mu_{2x}{}^{k}, \mu_{2y}{}^{k}, \mu_{2z}{}^{k}, \mu_{3x}{}^{k}, \mu_{3y}{}^{k}, \mu_{3z}{}^{k}, \mu_{1x}{}^{c}, \mu_{1y}{}^{c}, \mu_{1z}{}^{c}, \mu_{2x}{}^{c}, \mu_{2y}{}^{c}, \mu_{2z}{}^{c}, \mu_{3x}{}^{c}, \mu_{3y}{}^{c}, \mu_{3z}{}^{c}\}^T \quad (5.35)$$

The upper and lower boundaries on the design variables are considered as $\mathbf{UB}^{l}$.

$$\mathbf{UB}^{l} = \{\ \underbrace{1, \cdots, 1}_{18\ componets}\ \}^T \quad (5.36)$$

The lower boundary limits are considered as $\mathbf{LB}^{l}$,

$$\mathbf{LB}^{l} = \{\ \underbrace{0, \cdots, 0}_{18\ componets}\ \}^T \quad (5.37)$$

The starting point for the optimization is denoted as $\mathbf{x}_0{}^{l}$.

$$\mathbf{x}_0{}^{l} = \{\ \underbrace{1, \cdots, 1}_{18\ componets}\ \}^T \quad (5.38)$$

Similar to rigid case, the optimization calculations are conducted by MATLAB. The variable tolerance and objective tolerance are both 1.0e-6. The details of the optimization process are shown in Figure 49.

5.6 Results

Table 17 demonstrates the optimization results of the stiffness and damping coefficients of the supine human, while Table 18 shows the stiffness and damping coefficients for the litter-board transport system.

Figure 46-51 show the experimental transmissibility results for the rigid case and the litter-board case. The thick solid line represents the experimental geometrical mean of seven subjects.

In Figure 50-57, the response data of the eighth subject were compared with the dynamic model. It should be noted that the anthropometrical data of the dynamic model were based on the measurement of the eighth subject. Also, the comparison between the response of eighth subject and the dynamic model were conducted under vibration files that were not used in the system's parameters identification process shown in Eq. (5. 1).

The PSD of the predicted acceleration of the rigid case for the head, torso, and pelvis (Figure 48) were able to capture most of the frequency components of the experimental data. The predicted PSD magnitude of the head showed the best performance in comparison to the torso and pelvis. Similar characteristics were observed for the litter-board case in terms of capturing the frequency content of the signals; however, the magnitude of the PSD at the pelvis was better than those of the torso and head.

The predicted acceleration of the head for the rigid-case (Figure 52) showed a better trend than that of the pelvis and torso; however, the predicted acceleration for the torso followed the experimental peaks but was not able to reach the experimental magnitudes. The picture is different for the litter-board case (Figure 53), where the predicted acceleration of the torso showed a better trend in comparison to the pelvis and head.

5.7 Discussion

In this paper, a 3D dynamic human supine model is proposed. This model includes the coupling relationship between adjacent segments. This model is not only able to simulate and predict the dynamic response in different input signals, but is also able to simulate the force and moments at each joint (Eqs. (5.13)-(5.16)). Presenting a

practical approach to combining the supine human model with different types of transport systems, this model is able to use previously defined human parameters. The optimization process works to characterize the parameters of different transport systems.

There are three general types of human whole-body models. Most available supine models (Vogt, Mertens et al., 1978; Peng, Yang et al., 2009) are limited to separate lumped mass models, where models do not consider the coupling relationship between segments. Lumped mass models have been widely used in the seated position (Amirouche, Xie et al., 1994; Boileau and Rakheja, 1998; Bazrgari, Shirazi-Adl et al., 2008; Liang and Chiang, 2008; Wang, Bazrgari et al., 2010). Although the lumped mass model is very easy to implement, the lumped mass model cannot simulate the rotational motion. The inclusion of the coupling effect between adjacent segments enables models to capture the effects between neighboring segments. For example, the head showed a peak in the x direction at about 3Hz where the torso and sternum for both conditions also show a peak, as shown in Figure 40 andFigure 41. Such findings would make the proposed model a useful tool for vibration-suppression designers looking to gain more insight on supine-human response to vibration. The other two models are an FE model and a multi-body model. Although an FE model can provide more details of the human body response than a multi-body model, the FE model is a very expensive simulation to run, especially for dynamic problems. On the other hand, the multi-body model proposed in this paper uses much less computing time. While an FE model could provide an accurate prediction if the detailed human parameters are known, the human body is a very complex system. Some of the physical parameters of the human body are hard to define. Therefore, this model utilizes optimization to identify the human physical parameters, including spring and damper coefficients to present the muscle-based human system.

The model proposed in this paper is the first 3D supine model known. Lots of research focused on the 2D or 1D human modeling and simulation (Boileau and Rakheja,

1998; Nikooyan and Zadpoor, 2011). When it comes to supine human modeling, there are hardly any 3D models used. However, in reality, most input signals occur in three dimensions, and the responses from each segment are significant in all three dimensions, as seen in the diagonal transmissibility graphs in Figure 46 and Figure 47. Moreover, in Figure 46 and Figure 47, when the input is in the z direction and the output is in the x direction, the magnitude of transmissibility of each segment, both in the rigid and litter-board cases, are very significant. These graphs indicate that there is a relationship not only between the acceleration signal in the z direction with a z direction response, but also with a response in the x direction. Therefore, a 3D model is very necessary to provide an accurate and complete simulation for the supine human body. The model proposed in this article is also able to predict this phenomenon of z, x transmission of acceleration.

Experimentation shows significant differences, with different supports. In this research only rigid and litter-board are considered. Accordingly, this paper proposed a human supine model as the primary model, and a litter-board model as the secondary model based on the primary model. In practice, rigid support is not used very often, and when it comes to different supports, the article provides a convenient method to simulate the different support by simply adjusting $\boldsymbol{\mu}_m{}^k$ and $\boldsymbol{\mu}_m{}^c$.

Still, there are several assumptions used in this supine human model that may impose limitation on the applicability of the model. First, each body segment was considered as a rigid body. This assumption is reasonable for the head, but not for the rest of the body segments. Second, the contact points between the body segments and the rigid platform were assumed to have the same coordinate in the x direction. Therefore, there are only support forces, no support moments, coming from the rigid platform. Another limitation is that the model is assumed to be linear. At each joint, the forces are presented by linear springs and dampers. These springs and dampers were used to demonstrate the vertebra, ligaments, tendons, and muscles at each joint. However, they

can only demonstrate a linear relationship. Finally, the dynamic equation is derivate based on a linearized equation (the small displacement assumption). For WBV, this model satisfies this assumption in general.

5.8 Conclusion

A 3D dynamic model that resembles a supine human and two types of underlying transport systems under 3D WBV are presented in this work. The proposed model considers the coupling effect between the body segments and three directions. Therefore, the model is expected to capture the characteristics of that coupling. The proposed modeling algorithm has the potential to be used to investigate supine human response under different types of transport systems and therefore would assist vibration-suppression designers in their design efforts.

Table 17: 3 Dimensional supine human model spring and damper coefficients.

	X		Y		Z	
	Spring	Damping	Spring	Damping	Spring	Damping
Head	21042.4687	6.23607	24968.69	1.87634	109881.9	118.37436
Torso	13626.3	230.75564	8756.3798	425.6895	83841.2631	3574.1421
Pelvis	9147.712	487.42307	6041.9735	319.2810	107865.1404	0.15572
RJ-1	50005.3407	1.0	772.99260	11.0276	48964.02044	2140.48901
RJ-2	50005.6369	1.0	18832.4420	278.9596	49596.62756	4992.05973
TJ-1	31967.1758	14335.4643	14553.6	591.9361	122987.7866	8.06080
TJ-2	38485.4276	273.85106	22719.85	66.5209	68341.0267	46061.6181

Spring coefficient unit: *N/m* (translate) and *N·m/rad* (rotational)
Damper coefficient unit: *N·s/m* (translate) and *N·m·s/rad* (rotational)
RJ: Rotational Joint
TJ: Translational Joint

Table 18: Litter-board spring and damper softening coefficients.

	X		Y		Z	
	Spring $\mu_{mx}{}^{k}$	Damping $\mu_{mx}{}^{c}$	Spring $\mu_{my}{}^{k}$	Damping $\mu_{my}{}^{c}$	Spring $\mu_{mz}{}^{k}$	Damping $\mu_{mz}{}^{c}$
Head(m=1)	0.999999	0.00061	0.856369	0.48493	0.392676	0.9895818
Torso(m=2)	1	0.69365	0.83798	0.79235	0.00001	0.136749
Pelvis(m=3)	0.531199	0.94016	1	0.52112	0.61578	0.14479

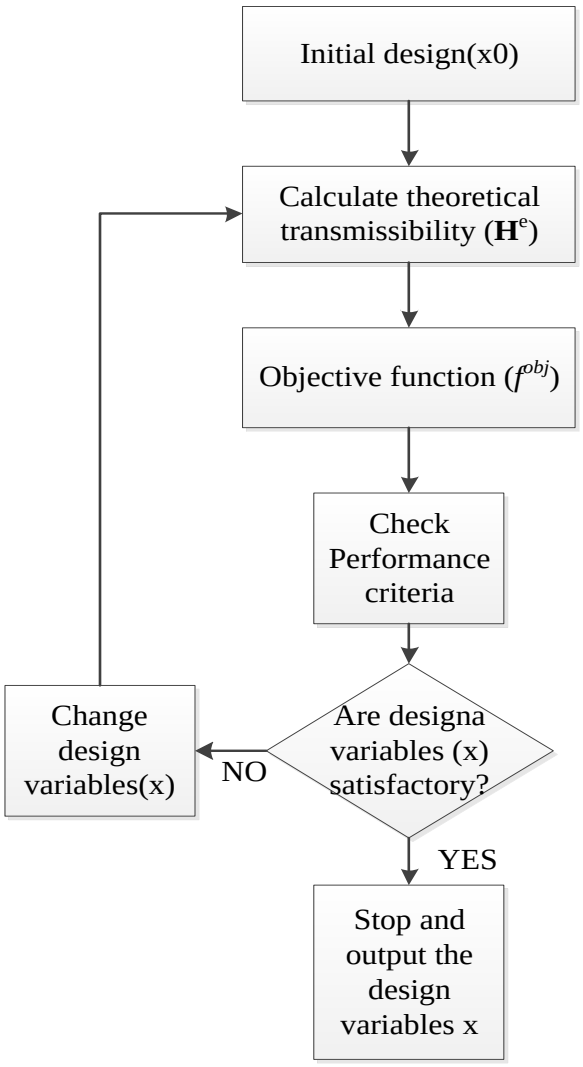

Figure 49: Optimization process

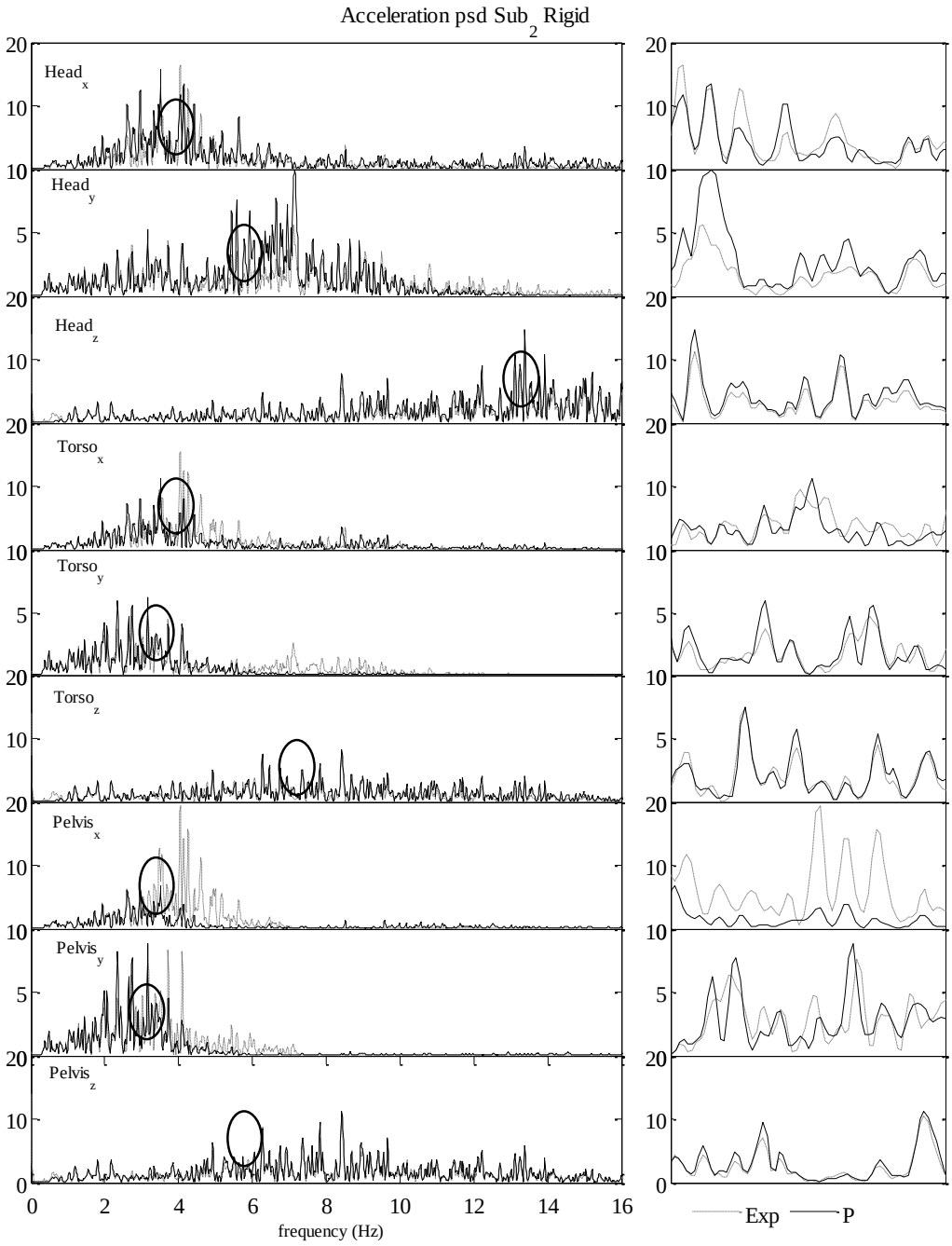

Figure 50: The frequency domain experimental (Subject 8) and predicted (based on anthropometrical data of Subject 8) acceleration for the head, torso, and pelvis under the rigid condition.

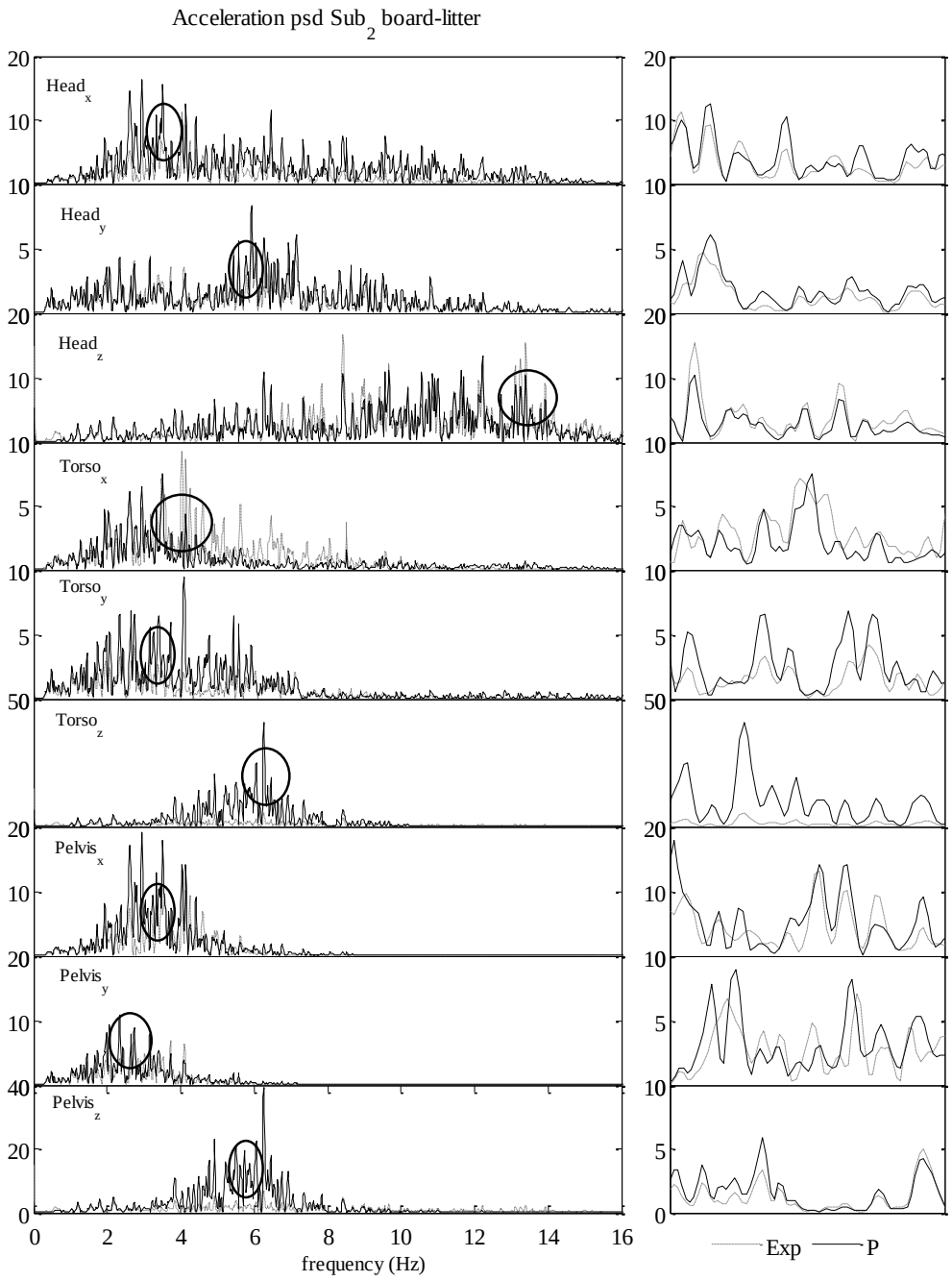

Figure 51: The frequency domain experimental (Subject 8) and predicted (based on anthropometrical data of Subject 8) acceleration for the head, torso, and pelvis under the litter-board condition.

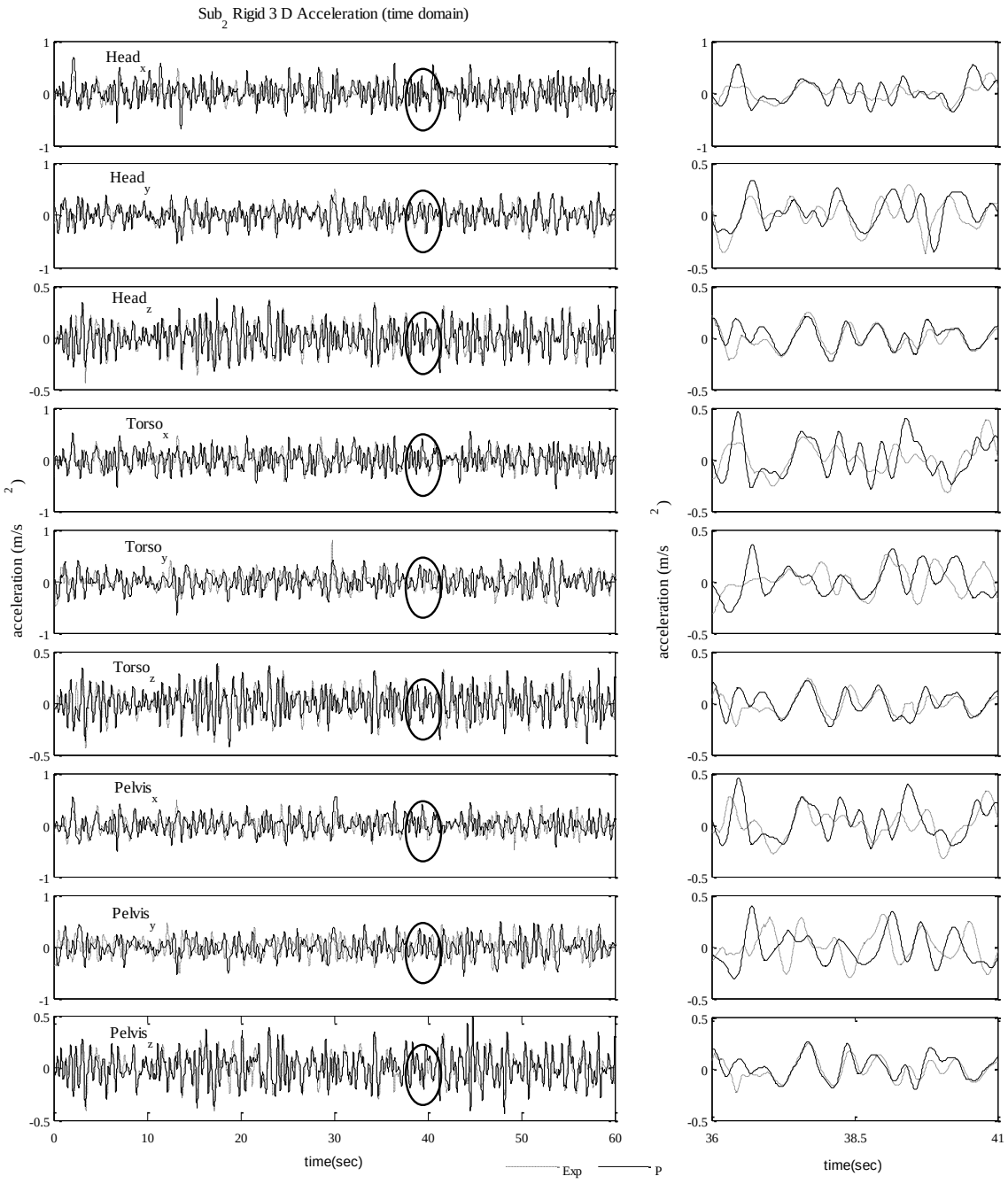

Figure 52: The time domain experimental (Subject 8) and predicted (based on anthropometrical data of Subject 8) acceleration for the head, torso, and pelvis under the rigid condition.

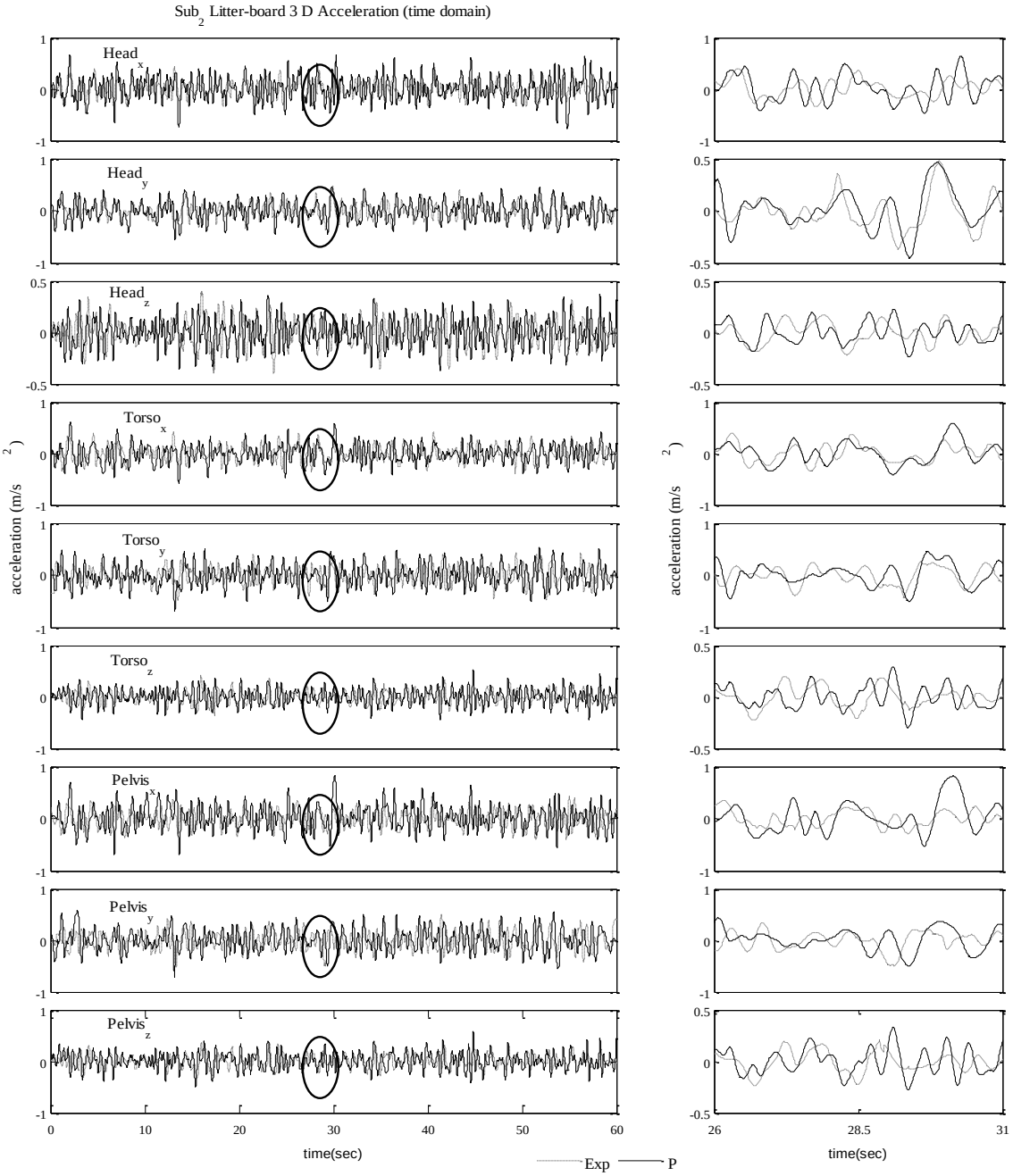

Figure 53: The time domain experimental (Subject 8) and predicted (based on anthropometrical data of Subject 8) acceleration for the head, torso, and pelvis under the litter-board condition.

CHAPTER VI

CONCLUSION AND FUTURE RESEARCH

6.1 Conclusion

Predictive human models for seated and supine positions in response to WBV with consideration of postures and muscle activity are introduced and validated in this thesis. Planar and 3D models are presented to simulate the head-neck and supine-human response in single- and multiple-axis WBV. The dynamic equations for all models are derived based on the Lagrange equation. Optimization methods in the frequency domain are used to identify the model parameters by minimizing the error between the experimental and theoretical transfer functions. Both passive and muscle-based models are explored in this thesis. The results showed that the models were able to reasonably predict the displacement, acceleration, and frequency content of the output motion on the human body. In general, the muscle-based model tends to be more stable and shows better results than the passive models at the high frequencies under consideration.

The major contributions of this thesis to the current knowledge and state of the art in human response to WBV can be summarized as follows:

(1) Development of planar predictive head-neck models in response to fore-aft WBV considering neutral and flexion postures.

(2) Introduction of a muscle-based model that relates muscle activity to motion.

(3) Development of a 3D head-neck model to predict human response to single and multiple-axis WBV considering different postures, including neutral, flexion, lateral flexion, and lateral rotational.

(4) Creation of a planar, coupled, supine-human model to predict human response to vertical WBV in the Cartesian and joint angle spaces under different support conditions.

(5) Development of a 3 D supine-human model under vibration with single- and multiple-axis WBV under different support conditions.

6.2 Future Work

The following issues will be studied in the future.

6.2.1 Anthropometric data

An accurate biomechanical model depends on the experimental data, so that during the optimization step, a set of accurate parameters can be identified. For example, for the rotational joints, the angles as well as the angular velocity and the angular acceleration are very hard to measure during the experiments.

6.2.2 Muscle-based model

For the supine models, muscle activities can only be demonstrated by linear springs and dampers, and the models are passive. However, muscle activities are nonlinear. Thus, a muscle-based model with active muscle activities should be considered for future research.

6.2.3 Optimization Method

All the parameters of HNS models and supine models are identified from experimental data based on an optimization method. However, this optimization problem is very nonlinear and complicated. It took a few hours to run the optimization problem, so a better optimization method is needed to get more optimal results with less computing time.

APPENDIX A: SINGLE-DOF EQUATION DERIVATION

The Lagrangian formulation:

$$\frac{d}{dt}\left(\frac{\partial Lar}{\partial \dot{\theta}}\right) - \frac{\partial Lar}{\partial \theta} + \frac{\partial D}{\partial \dot{\theta}} D = 0 \tag{A.1}$$

where $D = \frac{1}{2}\sum_{j=1}^{m}\sum_{k=1}^{m} C_{jk}\dot{q}_j\, q_k = \frac{1}{2} c\, \dot{\theta}^2$; $Lar = T - V$, Lar is Lagrange. The coordinate of the mass is called the end-effector, and is defined as (x_e, z_e) as shown in Figure A1. θ_0 is the initial reference angle and $\hat{\theta}$ is the angle refer to the reference θ_0 during vibration. And θ is the total angle, $\theta = \theta_0 + \hat{\theta}$ shown in Figure A1.

$$x_e = x_0 + l_0 sin\theta;\;\; z_e = l_0 cos\theta \tag{A.2}$$

$$\dot{x}_e = \dot{x_0} + l_0 cos\theta\dot{\theta};\; \dot{z}_e = -l_0 sin\theta\dot{\theta} \tag{A.3}$$

$$T = \frac{1}{2} m v^2 + \frac{1}{2} I\dot{\theta}^2 \tag{A.4}$$

$$V = mgz_e + \frac{1}{2} k\theta^2 \tag{A.5}$$

$$v^2 = \left(\frac{dx_e}{dt}\right)^2 + \left(\frac{dz_e}{dt}\right)^2 = \dot{x}_e{}^2 + \dot{z}_e{}^2 \tag{A.6}$$

Where l_0 is the length from C_7 to C_0. Substituting Eq.(A.4) and (A.5) into the Lagrangian equation (A.1) will results

$$\left(I + l_0{}^2 m\right)\ddot{\theta} + c\dot{\theta} + (k\theta - mgl_0 sin\theta) = ml_0 cos\theta\ddot{x}_o \tag{A.7}$$

Assuming the small relative angle during vibration, Taylor's first order expansion (A.8) is used to linearize Eq.(A.7).

$$f(x) = f(x_0) + f'(x_0)(x - x_0) + \cdots \tag{A.8}$$

The left side of (A.7) is:

$$\left(I + l_0{}^2 m\right)\ddot{\theta} + c\dot{\theta} + (k\theta - mgl_0 sin\theta)$$

$$= \left(I + l_0{}^2 m\right)\left(\ddot{\theta}_0 + \ddot{\hat{\theta}}\right) + c\left(\dot{\hat{\theta}} + \dot{\theta}_0\right) + k(\hat{\theta} + \theta_0) - mgl_0 \sin\left(\theta_0 + \hat{\theta}\right)$$

$$= \left(I + l_0{}^2 m\right)\ddot{\hat{\theta}} + c\dot{\hat{\theta}} + k\left(\theta_0 + \hat{\theta}\right) - mgl_0\,(\sin\theta_0 + \hat{\theta}\cos\theta_0)$$

$$= \left(I + l_0{}^2 m\right)\ddot{\hat{\theta}} + c\dot{\hat{\theta}} + (k - mgl_0\cos\theta_0)\hat{\theta} + (k\theta_0 - mgl_0\sin\theta_0)$$

The right side of (A.7) is:

$$ml_0 cos\theta \ddot{x}_o = ml_0 \cos(\theta_0 + \hat{\theta})\, \ddot{x}_o = (ml_0 \cos\theta_0 - ml_0 \hat{\theta} sin\theta_0)\ddot{x}_o$$

For the left side of (A.7), $(k\theta_0 - mgl_0 \sin\theta_0)$ is equal to zero. The right side nonlinear term $-ml_0 \hat{\theta} sin\theta_0 \ddot{x}_o$ is ignored. Thus the final dynamic equation is shown in (A.9), where $I_0 = I + {l_0}^2 m$

$$I_0 \ddot{\hat{\theta}} + c\dot{\hat{\theta}} + (k - mgl_0 cos\theta_0)\hat{\theta} = mLcos\theta_0 \ddot{x}_o \qquad \text{(A.9)}$$

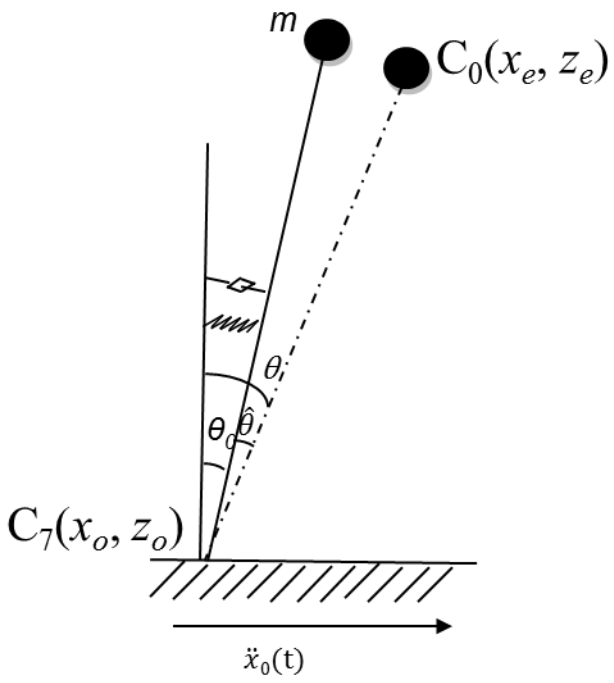

Figure A1: 1-DOF Passive model dynamics Equation

APPENDIX B: DENAVIT-HARTENBERG METHOD

A simplified human skeleton can be considered as a robot manipulator composed of a set of links connected by various joints, including a simple joint such as a revolute joint, a prismatic joint, or a more complex joint, such as a ball-and-socket joint. The Denavit-Hartenberg (DH) method (Denavit and Hartenberg, 1955) relates the position of a point in one coordinate system to another point by using transformation matrices. The basic convention in establishing coordinate systems on each frame is in the following rules (shown in Figure B1):

Embed the z_{i-1} axis along the axis of motion of the i^{th} joint;

Embed the x_i axis normal to the z_{i-1} with direction from joint i to joint $i+1$;

Embed the y_i axis such that it is perpendicular to x_i and z_i subject to right hand rule.

The joint variables $\boldsymbol{q}$ are defined as a vector of n-generalized coordinates. The position vector of a point of interest in the Cartesian space can be written in terms of the joint variables as $\boldsymbol{x}=\boldsymbol{x}(\boldsymbol{q})$, where $\boldsymbol{x}(\boldsymbol{q})$ can be obtained from the multiplication of transformation matrices ${}^{i-1}\mathbf{T}_i$ defined as the transformation matrix by the DH method. The transformation matrix ${}^{i-1}\mathbf{T}_i$ is used to represent frame i with respect to frame $i-1$ as shown in Eq. (B. 1).

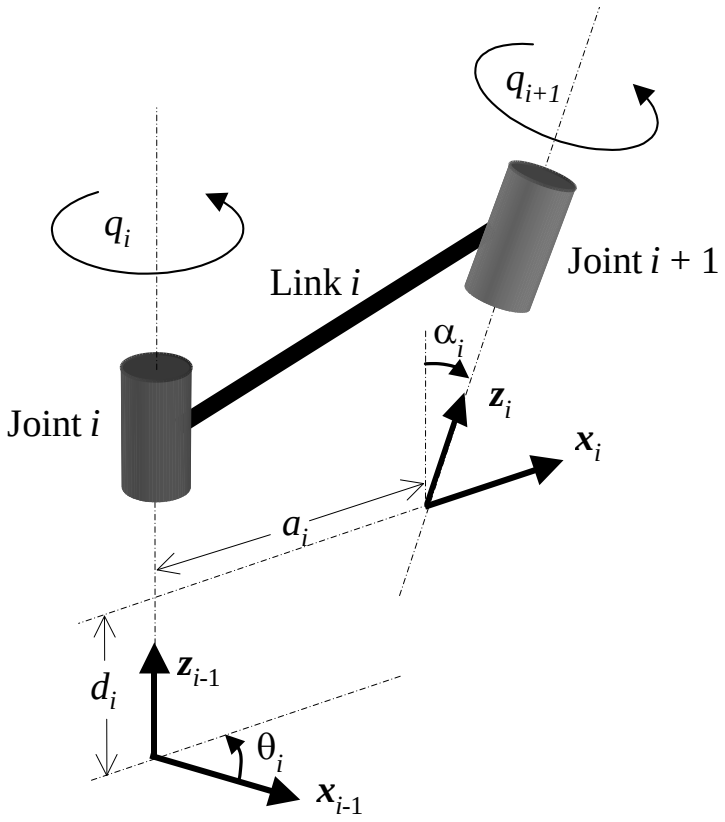

Figure B1: DH parameters

$$ {}^{i-1}\mathbf{T}_i = \left[\begin{array}{ccc|c} \cos\theta_i & -\cos\alpha_i \sin\theta_i & \sin\alpha_i \sin\theta_i & a_i \cos\theta_i \\ \sin\theta_i & \cos\alpha_i \cos\theta_i & -\sin\alpha_i \cos\theta_i & a_i \sin\theta_i \\ 0 & \sin\alpha_i & \cos\alpha_i & d_i \\ \hline 0 & 0 & 0 & 1 \end{array}\right] \quad \text{(B. 1)} $$

The matrix relates coordinate frames i and i-1 and is represented by four parameters: θ_i, d_i, α_i, and a_i. θ_i is the i^{th} joint angle, measured from x_{i-1} to x_i axis about z_{i-1}. d_i is the distance from the origin of the coordinate frame i-1 to the intersection of the z_{i-1}axis with the xi axis along the z_{i-1} axis. For a revolute joint, d_i is a constant and θ_i is the joint variable as shown in Eq. (B. 2). For a prismatic joint, d_i is the joint variable and θ_i is a constant number. α_i is the offset angle from the z_{i-1} axis to the z_i axis about the z_i axis about the x_i axis. a_i is the offset distance from the intersection of the z_{i-1} axis

with the x_i axis to the origin of frame i along the x_i axis. The joint variable q_i is the joint angle or sliding distance as shown in Eq. (B. 2). The set of joint variables $\boldsymbol{q} = [q_1, \dots, q_n]^{\boldsymbol{T}}$ is the joint vector. These joint variables uniquely determine the configuration of a manipulator system with n DOFs, called generalized coordinates. In this chapter, $\boldsymbol{q} = \boldsymbol{\theta}$ represents the joint angles vector.

$$q_i = \begin{cases} \theta_i: & joint\ i\ is\ revolute \\ d_i: & joint\ i\ is\ prismatic \end{cases} \tag{B. 2}$$

Let us define the augmented vector using the global Cartesian vector $\boldsymbol{x}(q)$ and the local Cartesian vector x_i as

$${}^0\boldsymbol{r}_i = \begin{bmatrix} \boldsymbol{x}(\boldsymbol{q}) \\ 1 \end{bmatrix}, \boldsymbol{r}_i = \begin{bmatrix} x_i \\ 1 \end{bmatrix} \tag{B. 3}$$

where $\boldsymbol{x}_i$ is the position of frame with respect to the i^{th} coordinate system. The matrix ${}^0\boldsymbol{T}_i(\boldsymbol{q})$ that relates frame i to frame 0 as shown in Eq. (B. 5) can be obtained by multiplying all intermediate transforms.

$${}^0\boldsymbol{r}_i = {}^0\boldsymbol{T}_i(\boldsymbol{q})\, \boldsymbol{r}_i \tag{B. 4}$$

$${}^0\mathbf{T}_n = \left[\prod_{i=1}^{n} {}^{i-1}\mathbf{T}_i \right] \tag{B. 5}$$

APPENDIX C: 3D SUPINE MODEL PARAMETERS

$$\boldsymbol{\alpha_k} = \begin{bmatrix} k_{x1} & 0 & 0 & 0 & 0 & 0 & k_{x2} & 0 & 0 & 0 & 0 & 0 & k_{x3} & 0 & 0 & 0 & 0 & 0 \\ 0 & k_{y1} & 0 & 0 & 0 & 0 & 0 & k_{y2} & 0 & 0 & 0 & 0 & 0 & k_{y3} & 0 & 0 & 0 & 0 \\ 0 & 0 & k_{z1} & 0 & 0 & 0 & 0 & 0 & k_{z2} & 0 & 0 & 0 & 0 & 0 & k_{z3} & 0 & 0 & 0 \end{bmatrix}^T \tag{C.1}$$

$$\boldsymbol{\alpha_k} = \begin{bmatrix} c_{x1} & 0 & 0 & 0 & 0 & 0 & c_{x2} & 0 & 0 & 0 & 0 & 0 & c_{x3} & 0 & 0 & 0 & 0 & 0 \\ 0 & c_{y1} & 0 & 0 & 0 & 0 & 0 & c_{y2} & 0 & 0 & 0 & 0 & 0 & c_{y3} & 0 & 0 & 0 & 0 \\ 0 & 0 & c_{z1} & 0 & 0 & 0 & 0 & 0 & c_{z2} & 0 & 0 & 0 & 0 & 0 & c_{z3} & 0 & 0 & 0 \end{bmatrix}^T \tag{C.2}$$

$$\mathbf{K} = \mathbf{K}^T = \begin{bmatrix} k_{1,1} & \cdots & k_{1,18} \\ \vdots & \ddots & \vdots \\ k_{18,18} & \cdots & k_{18,18} \end{bmatrix} \tag{C.3}$$

$$\mathbf{C} = \mathbf{C}^T = \begin{bmatrix} c_{1,1} & \cdots & c_{1,18} \\ \vdots & \ddots & \vdots \\ c_{18,18} & \cdots & c_{18,18} \end{bmatrix} \tag{C.4}$$

where $k_{i,j}$ and $c_{i,j}$ are shown in the following:

$$k_{1,1} = k_{tx1} + k_{x1}$$

$$k_{1,2} = \cdots = k_{1,4} = 0$$

$$k_{1,5} = k_{tx1} l_{b1z}$$

$$k_{1,6} = -k_{tx1} l_{b1y}$$

$$k_{1,7} = -k_{tx1}$$

$$k_{1,8} = \cdots = k_{1,10} = 0$$

$$k_{1,11} = -k_{tx1} l_{a2z}$$

$$k_{1,12} = k_{tx1} l_{a2y}$$

$$k_{1,13} = \cdots = k_{1,18} = 0$$

$$k_{2,2} = k_{ty1} + k_{y1}$$

$$k_{2,3} = 0$$

$$k_{2,4} = -k_{ty1} l_{b1z}$$

$$k_{2,3} = k_{2,5} = k_{2,7} = k_{2,9} = k_{2,11} = 0$$

$$k_{2,6} = k_{ty1} l_{b1x}$$

$$k_{2,8} = -k_{ty1}$$

$$k_{2,10} = -k_{ty1} l_{a2z}$$

$$k_{2,12} = -k_{ty1} l_{a2x}$$

$$k_{2,13} = \cdots = k_{2,18} = 0$$

$$k_{3,3} = k_{tz1} + k_{z1}$$

$$k_{3,4} = k_{tz1} l_{b1y}$$

$$k_{3,5} = -k_{tz1} l_{b1x}$$

$$k_{3,6} = \cdots = k_{3,8} = 0$$

$$k_{3,9} = -k_{tz1}$$

$$k_{3,10} = -k_{tz1} l_{a2y}$$

$$k_{3,11} = k_{tz1} l_{a2x}$$

$$k_{3,12} = \cdots = k_{3,18} = 0$$

$$k_{4,4} = k_{tz1} {l_{b1y}}^2 + k_{ty1}(l_{a2y} - l_{b1y}) l_{b1y} + k_{ty1} {l_{b1z}}^2 + k_{r1x} - k_{tz1} l_{b1z}(l_{b1z} - l_{a2z})$$

$$k_{4,5} = -k_{tz1} l_{b1x} l_{b1y} - k_{ty1} l_{b1x}(l_{a2y} - l_{b1y})$$

$$k_{4,6} = k_{tx1} l_{b1z}(l_{b1x} - l_{a2x}) - k_{ty1} l_{b1x} l_{b1z}$$

$$k_{4,7} = 0$$

$$k_{4,8} = k_{ty1} l_{b1z}$$

$$k_{4,9} = -k_{tz1} l_{b1y}$$

$$k_{4,10} = -k_{r1x} - k_{tz1} l_{b1y} l_{a2y} - k_{ty1} l_{b1z} l_{a2z}$$

$$k_{4,11} = k_{tz1} l_{b1y} l_{a2x}$$

$$k_{4,12} = k_{ty1} l_{b1z} l_{a2x}$$

$$k_{4,13} = \cdots = k_{4,18} = 0$$

$$k_{5,5} = k_{tz1} {l_{b1x}}^2 - k_{tx1}(l_{b1x} - l_{a2x}) l_{b1x} + k_{tx1} {l_{b1z}}^2 + k_{ry1} + k_{tz1} l_{b1z}(l_{a2z} - l_{b1z})$$

$$k_{5,6} = k_{ty1} l_{b1z}(l_{b1y} - l_{a2y}) - k_{tx1} l_{b1y} l_{b1z}$$

$$k_{5,7} = -k_{tx1} l_{b1z}$$

$$k_{5,8} = 0$$

$$k_{5,9} = k_{tz1} l_{b1x}$$

$$k_{5,10} = k_{tz1} l_{b1x} l_{a2y}$$

$$k_{5,11} = -k_{ry1} - k_{tz1} l_{b1x} l_{a2x} - k_{tx1} l_{b1z} l_{a2z}$$

$$k_{5,12} = k_{tx1} l_{b1z} l_{a2y}$$

$$k_{5,13} = \cdots = k_{5,18} = 0$$

$$k_{6,6} = k_{ty1} {l_{b1x}}^2 + k_{tx1}(l_{a2x} - l_{b1x}) l_{b1x} + k_{tx1} {l_{b1y}}^2 + k_{rz1} - k_{ty1} l_{b1y}(l_{b1y} - l_{a2y})$$

$$k_{6,7} = k_{tx1} l_{b1y}$$

$$k_{6,8} = -k_{ty1} l_{b1x}$$

$$k_{6,9} = 0$$

$$k_{6,10} = k_{ty1} l_{b1x} l_{a2z}$$

$$k_{6,11} = k_{tx1} l_{b1y} l_{a2z}$$

$$k_{6,12} = -k_{rz1} - k_{ty1} l_{b1x} l_{a2x} - k_{tx1} l_{b1y} l_{a2y}$$

$$k_{6,13} = \cdots = k_{6,18} = 0$$

$$k_{7,7} = k_{tx1} + k_{tx2} + k_{x2}$$

$$k_{7,8} = \cdots = k_{7,10} = 0$$

$$k_{7,11} = k_{tx1} l_{a2z} + k_{tx2} l_{b2z}$$

$$k_{7,12} = -k_{tx1}l_{a2y} - k_{tx2}l_{b2y}$$

$$k_{7,13} = -k_{tx2}$$

$$k_{7,14} = \cdots = k_{7,16} = 0$$

$$k_{7,17} = -k_{tx2}l_{a3z}$$

$$k_{7,18} = k_{tx2}l_{a3y}$$

$$k_{8,8} = k_{ty1} + k_{ty2} + k_{y2}$$

$$k_{8,9} = k_{8,11} = k_{8,13} = k_{8,15} = k_{8,17} = 0$$

$$k_{8,10} = -k_{ty1}l_{a2z} - k_{ty2}l_{b2z}$$

$$k_{8,12} = k_{ty1}l_{a2x} + k_{ty2}l_{b2x}$$

$$k_{8,14} = -k_{ty2}$$

$$k_{8,16} = k_{ty2}l_{a3z}$$

$$k_{8,18} = -k_{ty2}l_{a3x}$$

$$k_{9,9} = k_{tz1} + k_{tz2} + k_{z2}$$

$$k_{9,10} = k_{tz1}l_{a2y} + k_{tz2}l_{b2y}$$

$$k_{9,11} = -k_{tz1}l_{a2x} - k_{tz2}l_{b2x}$$

$$k_{9,12} = \cdots = k_{9,14} = 0$$

$$k_{9,15} = -k_{tz2}$$

$$k_{9,16} = -k_{tz2}l_{a3y}$$

$$k_{9,17} = k_{tz2}l_{a3x}$$

$$k_{9,18} = 0$$

$$k_{10,10} = k_{tz1}{l_{a2y}}^2 + k_{ty1}(l_{b1y} - l_{a2y})l_{a2y} + k_{ty1}{l_{a2z}}^2 + k_{tz2}{l_{b2y}}^2 + k_{ty2}{l_{b2z}}^2 + k_{rx1} + k_{rx2} - k_{tz1}l_{a2z}(l_{a2z} - l_{b1z}) + k_{ty2}l_{b2y}(l_{a3y} - l_{b2y}) - k_{tz2}l_{b2z}(l_{b2z} - l_{a3z})$$

$$k_{10,11} = -k_{ty1}l_{a2x}(l_{b1y} - l_{a2y}) - k_{tz1}l_{a2x}l_{a2y} - k_{tz2}l_{a2x}l_{b2y} - k_{ty2}l_{b2x}(l_{a3y} - l_{b2y})$$

$$k_{10,12} = -k_{tx1}(l_{b1x} - l_{a2x})l_{a2z} - k_{ty1}l_{a2x}l_{a2z} - k_{ty2}l_{b2x}l_{b2z} + k_{tx2}l_{b2z}(l_{b2x} - l_{a3x})$$

$$k_{10,13} = 0$$

$$k_{10,14} = k_{ty2}l_{b2z}$$

$$k_{10,15} = -k_{tz2}l_{b2y}$$

$$k_{10,16} = -k_{rx2} - k_{tz2}l_{b2y}l_{a3y} - k_{ty2}l_{b2z}l_{a3z}$$

$$k_{10,17} = k_{tz2}l_{b2y}l_{a3x}$$

$$k_{10,18} = k_{ty2}l_{b2z}l_{a3x}$$

$$k_{11,11} = k_{tz1}{l_{a2x}}^2 + k_{tx1}(l_{b1x} - l_{a2x})l_{a2x} + k_{tx1}{l_{a2z}}^2 + k_{tz2}{l_{b2z}}^2 + k_{tx2}{l_{b2z}}^2 + k_{ry1} + k_{ry2} + k_{tz1}(l_{b1z} - l_{a2z})l_{a2z} - k_{tx2}l_{b2x}(l_{b2x} - l_{a3x}) + k_{tz2}l_{b2z}(l_{a3z} - l_{b2z})$$

$$k_{11,12} = -k_{tx1}l_{a2y}l_{a2z} + k_{ty1}(l_{a2y} - l_{b1y})l_{a2z} - k_{tx2}l_{b2y}l_{b2z} + k_{ty2}l_{b2z}(l_{b2y} - l_{a3y})$$

$$k_{11,13} = -k_{tx2}l_{b2z}$$

$$k_{11,14} = 0$$

$$k_{11,15} = k_{tz2}l_{b2x}$$

$$k_{11,16} = k_{tz2}l_{b2x}l_{a3y}$$

$$k_{11,17} = -k_{ry2} - k_{tz2}l_{b2x}l_{a3x} - k_{tx2}l_{b2z}l_{a3z}$$

$$k_{11,18} = k_{tx2}l_{b2z}l_{a3y}$$

$$k_{12,12} = k_{ty1}{l_{a2x}}^2 + k_{tx1}(l_{b1x} - l_{a2x})l_{a2x} + k_{tx1}{l_{a2y}}^2 + k_{ty2}{l_{b2x}}^2 + k_{tx2}{l_{b2y}}^2 + k_{rz1} + k_{rz2} - k_{ty1}l_{a2y}(l_{a2y} - l_{b1y}) + k_{tx2}l_{b2x}(l_{a3x} - l_{b2x}) - k_{ty2}l_{b2y}(l_{b2y} - l_{a3y})$$

$$k_{12,13} = k_{tx2}l_{b2y}$$

$$k_{12,14} = -k_{ty2}l_{b2x}$$

$$k_{12,15} = 0$$

$$k_{12,16} = k_{ty2} l_{b2x} l_{a3z}$$

$$k_{12,17} = k_{tx2} l_{b2y} l_{a3z}$$

$$k_{12,18} = -k_{rz2} - k_{ty2} l_{b2x} l_{a3x} - k_{tx2} l_{b2y} l_{a3y}$$

$$k_{13,13} = k_{tx2} + k_{x3}$$

$$k_{13,14} = \cdots = k_{13,16} = 0$$

$$k_{13,17} = k_{tx2} l_{a3z}$$

$$k_{13,18} = -k_{tx2} l_{a3y}$$

$$k_{14,14} = k_{ty2} + k_{y3}$$

$$k_{14,15} = k_{14,17} = 0$$

$$k_{14,16} = -k_{ty2} l_{a3z}$$

$$k_{14,18} = k_{ty2} l_{a3x}$$

$$k_{15,15} = k_{tz2} + k_{z2}$$

$$k_{15,16} = k_{tz2} l_{a3y}$$

$$k_{15,17} = -k_{tz2} l_{a3x}$$

$$k_{15,18} = 0$$

$$k_{16,16} = k_{tz2} {l_{a3y}}^2 + k_{ty2}(l_{b2y} - l_{a3y}) l_{a3y} + k_{ty2} {l_{a3z}}^2 + k_{rx2} - k_{tz2} l_{a3z}(l_{a3z} - l_{b2z})$$

$$k_{16,17} = k_{ty2} l_{a3x}(l_{b2y} - l_{a3y}) - k_{tz2} l_{a3x} l_{a3y}$$

$$k_{16,18} = -k_{tx2}(l_{b2x} - l_{a3x}) l_{a3z} - k_{ty2} l_{a3x} l_{a3z}$$

$$k_{17,17} = k_{tz2} {l_{a3x}}^2 + k_{tx2}(l_{b2x} - l_{a3x}) l_{a3x} + k_{tx2} {l_{a3z}}^2 + k_{ry2} + k_{tz2}(l_{b2z} - l_{a3z}) l_{a3z}$$

$$k_{17,18} = k_{ty2}(l_{a3y} - l_{b2y}) l_{a3z} - k_{tx2} l_{a3y} l_{a3z}$$

$$k_{18,18} = k_{ty2} {l_{a3x}}^2 + k_{tx2}(l_{b2x} - l_{a3x}) l_{a3x} + k_{tx2} {l_{a3y}}^2 + k_{rz2} - k_{ty2} l_{a3y}(l_{a3y} - l_{b2y})$$

$$c_{1,1} = c_{tx1} + c_{x1}$$

$$c_{1,2} = \cdots = c_{1,4} = 0$$

$$c_{1,5} = c_{tx1} l_{b1z}$$

$$c_{1,6} = -c_{tx1} l_{b1y}$$

$$c_{1,7} = -c_{tx1}$$

$$c_{1,8} = \cdots = c_{1,10} = 0$$

$$c_{1,11} = -c_{tx1} l_{a2z}$$

$$c_{1,12} = c_{tx1} l_{a2y}$$

$$c_{1,13} = \cdots = c_{1,18} = 0$$

$$c_{2,2} = c_{ty1} + c_{y1}$$

$$c_{2,3} = c_{2,5} = c_{2,7} = c_{2,9} = c_{2,11} = 0$$

$$c_{2,4} = -c_{ty1} l_{b1z}$$

$$c_{2,6} = c_{ty1} l_{b1x}$$

$$c_{2,8} = -c_{ty1}$$

$$c_{2,10} = c_{ty1} l_{a2z}$$

$$c_{2,12} = -c_{ty1} l_{a2x}$$

$$c_{2,13} = \cdots = c_{2,18} = 0$$

$$c_{3,3} = c_{tz1} + c_{z1}$$

$$c_{3,4} = c_{tz1} l_{b1y}$$

$$c_{3,5} = -c_{tz1} l_{b1x}$$

$$c_{3,6} = \cdots = c_{3,8} = 0$$

$$c_{3,9} = -c_{tz1}$$

$$c_{3,10} = -c_{tz1} l_{a2y}$$

$$c_{3,11} = c_{tz1} l_{a2x}$$

$$c_{3,12} = \cdots = c_{3,18} = 0$$

$$c_{4,4} = c_{tz1}{l_{b1y}}^2 + c_{ty1}{l_{b1z}}^2 + c_{rx1}$$

$$c_{4,5} = -c_{tz1}l_{b1x}l_{b1y}$$

$$c_{4,6} = -c_{ty1}l_{b1x}l_{b1z}$$

$$c_{4,7} = 0$$

$$c_{4,8} = c_{ty1}l_{b1z}$$

$$c_{4,9} = -c_{tz1}l_{b1y}$$

$$c_{4,10} = -c_{rx1} - c_{tz1}l_{b1y}l_{a2y} - c_{ty1}l_{b1z}l_{a2z}$$

$$c_{4,11} = c_{tz1}l_{b1y}l_{a2x}$$

$$c_{4,12} = c_{ty1}ll_{b1z}l_{a2x}$$

$$c_{4,13} = \cdots = c_{4,18} = 0$$

$$c_{5,5} = c_{tz1}{l_{b1x}}^2 + c_{tx1}{l_{b1z}}^2 + c_{ry1}$$

$$c_{5,6} = -c_{tx1}l_{b1y}l_{b1z}$$

$$c_{5,7} = -c_{tx1}l_{b1z}$$

$$c_{5,8} = 0$$

$$c_{5,9} = c_{tz1}l_{b1x}$$

$$c_{5,10} = c_{tz1}l_{b1x}l_{a2y}$$

$$c_{5,11} = -c_{ry1} - c_{tz1}l_{b1x}l_{a2x} - c_{tx1}l_{b1z}l_{a2z}$$

$$c_{5,12} = c_{tx1}l_{b1z}l_{a2y}$$

$$c_{5,13} = \cdots = c_{5,18} = 0$$

$$c_{6,6} = c_{ty1}{l_{b1x}}^2 + c_{tx1}{l_{b1y}}^2 + c_{rz1}$$

$$c_{6,7} = c_{tx1}l_{b1y}$$

$$c_{6,8} = c_{ty1}l_{b1x}$$

$$c_{6,9} = 0$$

$$c_{6,10} = c_{ty1} l_{b1x} l_{a2z}$$

$$c_{6,11} = c_{tx1} l_{b1y} l_{a2z}$$

$$c_{6,12} = -c_{rz1} - c_{ty1} l_{b1x} l_{a2x} - c_{tx1} l_{b1y} l_{a2y}$$

$$c_{6,13} = \cdots = c_{6,18} = 0$$

$$c_{7,7} = c_{tx1} + c_{tx2} + c_{x2}$$

$$c_{7,8} = \cdots = c_{7,10} = 0$$

$$c_{7,11} = c_{tx1} l_{a2z} + c_{tx2} l_{b2z}$$

$$c_{7,12} = -c_{tx1} l_{a2y} - c_{tx2} l_{b2y}$$

$$c_{7,13} = \cdots = c_{7,18} = 0$$

$$c_{8,8} = c_{ty1} + c_{ty2} + c_{y2}$$

$$c_{8,9} = 0$$

$$c_{8,10} - c_{ty1} l_{a2z} - c_{ty2} l_{b2z}$$

$$c_{8,11} = c_{8,13} = c_{8,15} = c_{8,17} = 0$$

$$c_{8,12} = c_{ty1} l_{a2x} + c_{ty2} l_{b2x}$$

$$c_{8,13} = -c_{ty2}$$

$$c_{8,16} = c_{ty2} l_{a3z}$$

$$c_{8,18} = -c_{ty2} l_{a3x}$$

$$c_{9,9} = c_{tz1} + c_{tz2} + c_{z2}$$

$$c_{9,10} = c_{tz1} l_{a2y} + c_{tz2} l_{b2y}$$

$$c_{9,11} = -c_{tz1} l_{a2x} - c_{tz2} l_{b2x}$$

$$c_{9,12} = \cdots = c_{9,14} = 0$$

$$c_{9,15} = -c_{tz2}$$

$$c_{9,16} = -c_{tz2} l_{a3y}$$

$$c_{9,17} = c_{tz2} l_{a3x}$$

$$c_{9,18} = 0$$

$$c_{10,10} = c_{tz1} {l_{a2y}}^2 + c_{ty1} {l_{a2z}}^2 + c_{tz2} {l_{b2y}}^2 + c_{ty2} {l_{b2z}}^2 + c_{rx1} + c_{rx2}$$

$$c_{10,11} = -c_{tz1} l_{a2x} l_{a2y} - c_{tz2} l_{b2x} l_{b2y}$$

$$c_{10,12} = -c_{ty1} l_{a2x} l_{a2z} - c_{ty2} l_{b2x} l_{b2z}$$

$$c_{10,13} = 0$$

$$c_{10,14} = c_{ty2} l_{b2z}$$

$$c_{10,15} = -c_{tz2} l_{b2y}$$

$$c_{10,16} = -c_{rx2} - c_{tz2} l_{b2y} l_{a3y} - c_{ty2} l_{b2z} l_{a3z}$$

$$c_{10,17} = c_{tz2} l_{b2y} l_{a3x}$$

$$c_{10,18} = c_{ty2} l_{b2z} l_{a3x}$$

$$c_{11,11} = c_{tz1} {l_{a2x}}^2 + c_{tx1} {l_{a2z}}^2 + c_{tz2} {l_{b2x}}^2 + c_{tx2} {l_{b2z}}^2 + c_{ry1} + c_{ry2}$$

$$c_{11,12} = -c_{tx1} l_{a2y} l_{a2z} - c_{tx2} l_{b2y} l_{b2z}$$

$$c_{11,13} = -c_{tx2} l_{b2z}$$

$$c_{11,14} = 0$$

$$c_{11,15} = c_{tz2} l_{b2x}$$

$$c_{11,16} = c_{tz2} l_{b2x} l_{a3y}$$

$$c_{11,17} = -c_{ry2} - c_{tz2} l_{b2x} l_{a3x} - c_{tx2} l_{b2z} l_{a3z}$$

$$c_{11,18} = c_{tx2} l_{b2z} l_{a3y}$$

$$c_{12,12} = c_{rz1} + c_{rz2} + c_{ty1} {l_{a2x}}^2 + c_{tx1} {l_{b2y}}^2 + c_{ty2} {l_{b2x}}^2 + c_{tx2} {l_{b2y}}^2$$

$$c_{12,13} = c_{tx2} l_{b2y}$$

$$c_{12,14} = -c_{ty2} l_{b2x}$$

$$c_{12,15} = 0$$

$$c_{12,16} = c_{ty2} l_{b2x} l_{a3z}$$

$$c_{12,17} = c_{tx2} l_{b2y} l_{a3z}$$

$$c_{12,18} = -c_{rz2} - c_{ty2} l_{b2x} l_{a3x} - c_{tx2} l_{b2y} l_{a3y}$$

$$c_{13,13} = c_{tx2} + c_{x3}$$

$$c_{13,14} = \cdots = c_{13,16} = 0$$

$$c_{13,17} = c_{tx2} l_{a3z}$$

$$c_{13,18} = -c_{tx2} l_{a3y}$$

$$c_{14,14} = c_{ty2} + c_{y3}$$

$$c_{14,15} = 0$$

$$c_{14,16} = -c_{ty2} l_{a3z}$$

$$c_{14,17} = 0$$

$$c_{14,18} = c_{ty2} l_{a3x}$$

$$c_{15,15} = c_{tz2} + c_{z3}$$

$$c_{15,16} = c_{tz2} l_{a3y}$$

$$c_{15,17} = -c_{tz2} l_{a3x}$$

$$c_{15,18} = 0$$

$$c_{16,16} = c_{rx2} + c_{tz2} {l_{a3y}}^2 + c_{ty2} {l_{a3z}}^2$$

$$c_{16,17} = -c_{tz2} l_{a3x} l_{a3y}$$

$$c_{16,18} = -c_{ty2} l_{a3x} l_{a3z}$$

$$c_{17,17} = c_{ry2} + c_{tz2} {l_{a3x}}^2 + c_{tx2} {l_{a3z}}^2$$

$$c_{17,18} = -c_{tx2} l_{a3y} l_{a3z}$$

$$c_{18,18} = c_{rz2} + c_{ty2} {l_{a3x}}^2 + c_{tx2} {l_{a3y}}^2$$

$$\mathbf{R} = \begin{bmatrix} \mathbf{R}_1 & \boldsymbol{O}_{3\times6} & \boldsymbol{O}_{3\times6} \\ \boldsymbol{O}_{3\times6} & \mathbf{R}_2 & \boldsymbol{O}_{3\times6} \\ \boldsymbol{O}_{3\times6} & \boldsymbol{O}_{3\times6} & \mathbf{R}_3 \end{bmatrix} \tag{C.5}$$

where $\mathbf{R}_m = \begin{bmatrix} 1 & 0 & 0 & 0 & p^e_{mz} & p^e_{my} \\ 0 & 1 & 0 & -p^e_{mz} & 0 & p^e_{mx} \\ 0 & 0 & 1 & p^e_{my} & -p^e_{mx} & 0 \end{bmatrix} (m = 1,\ 2,\ 3)$

APPENDIX D: INFORMED CONSENT DOCUMENT

The following pages reflect an unsigned informed consent document:

FOR IRB USE ONLY
APPROVED BY: IRB-02
IRB ID #: 200811705
APPROVAL DATE: 08/06/11
EXPIRATION DATE: 08/05/12

INFORMED CONSENT DOCUMENT

Project Title: Comfort Weighting Curve for Seated Machine Operators

Principal Investigator: **Salam Rahmatalla**

Research Team Contact: **Salam Rahmatalla, 1 319 335-5614**

John Meusch
Jonathan DeShaw

This consent form describes the research study to help you decide if you want to participate. This form provides important information about what you will be asked to do during the study, about the risks and benefits of the study, and about your rights as a research subject.

- If you have any questions about or do not understand something in this form, you should ask the research team for more information.
- You should discuss your participation with anyone you choose such as family or friends.
- Do not agree to participate in this study unless the research team has answered your questions and you decide that you want to be part of this study.

WHAT IS THE PURPOSE OF THIS STUDY?

This is a research study. We are inviting you to participate in this research study because you are a healthy, adult who does not have a history of muscle or bone disease or injury.

The purpose of this research study is to determine a proper shape of the comfort weighting curve for seated machine operators. This comfort curve will serve seat manufacturer in understanding the impact of machine changes on human comfort in single and multiple directions and therefore, help them in designing better and safer seats.
The study may also investigate the motion of people in supine position during emergency transportation with the goal of achieving better litter designs.

HOW MANY PEOPLE WILL PARTICIPATE?

Approximately 100 people will take part in this study at the University of Iowa.

HOW LONG WILL I BE IN THIS STUDY?

If you agree to take part in this study, your involvement will last for 3-6 hours in a single visit with no follow-up. If there are technical problems, you may be scheduled for second visit to complete the study procedures.

WHAT WILL HAPPEN DURING THIS STUDY?

If you agree to participate, you will be scheduled to return to the Engineering Research Facility, 330 South Madison Street, Iowa City, Iowa the morning of the test day. Inside the facility, you will change in to shorts and a tank-top so that the motion measurements can be obtained. The clothing will be supplied to you at the test site.

Preparation and Set-Up

Marker placement and calibration: Your body motion will be monitored using infrared cameras (VICON). Up to 90 reflective markers will be attached to your body. Each marker is about a half inch sphere attached to a soft rubber base of about 1 ½ inch x 1 ½ inch. The rubber base will be attached to your body using non-allergenic, double-sided tape. The markers on your head will be attached to an adjustable head band which you will wear on your head. Markers will be attached to your skin over bony landmarks, such as the elbow, the knee, the collar bone, or back bone. If you have considerable body hair, we will shave the small area of skin under each marker to minimize pain with removal of the markers. Markers may also be attached using athletic pre-wrap instead of adhesive tape. In some parts of the experiment, you may be dressed in a motion capture suit (a black cloth suit to which markers will be attached); in this case, the markers will be directly stuck to the suit instead of your skin.

Inertial sensors: Inertial sensors are devices that can measure acceleration in three and six directions. Inertial sensors are small devices that can sense movement. Inertial sensors will also be attached to your body at the same time the above markers are attached. Inertial sensors will be placed on you on up to 8 locations. The Inertial sensors will be attached to your skin using medical-grade, double-sided adhesive tapes, after cleaning your skin with rubbing alcohol.

The placement of the markers and inertial sensors will take about one to two hours.

In addition to the recordings for motion tracking, we will videotape the study procedure.

Testing

After this preparation stage, you will be instructed to sit on a chair or lay on a litter similar to those used in patient's transportation that is attached to a table that vibrates, called a shaker table. During the experiments, you will experience the physical conditions of a heavy construction machinery operator who is performing tasks in the real world or a person on a litter in an emergency transport vehicle.

Motion Capture Calibration: The first step in the motion capture process is to calibrate the system and ensure that the cameras see only the reflected markers (no artifact). The second step involves calibrating you by having you stand still for 30 seconds. The motion capture system will use this information to obtain your measurements, such as the length of your legs and arms.

Task Simulation: In order for you to keep your attention focused, we may provide a task for you to work on. The task consists of a video-game like simulation of the operation of a piece of heavy equipment. You will control the piece of equipment using the arm-rest controls you will be holding during the testing.

Experimental Protocol:
You will be tested under one of the following conditions:

Condition A) You will be asked to sit in the shaker table chair. The experiments to be conducted will include using a shaker table to provide vibration typical of operation of common heavy equipment.

You may be tested under the following scenarios:

1. Back on seatback and hands on armrests
2. Back on seatback and hands on lap
3. Back on seatback and hands on steering wheel
4. Back off seatback and hands on lap, and looking back (twisted posture)
5. Back off seatback and hands on armrests, and looking back (twisted posture)
6. Back off seatback and hands on lap
7. Back off seatback and hands on steering wheel
8. Back off seatback and hands on armrests
9. In some of the above cases, you may be asked to sit on a seat with your trunk constrain to the seatback using a life-Vest jacket; however, your arms will be freely to move. The reason for these cases is to isolate your head-neck motion from your trunk motion. By doing this, we will be able to more accurately analyzing the contribution of your head-motion to your discomfort level.

In all above cases, your feet will remain on the ground/pedals.

Condition B) You will be asked to take a supine position on a litter with a backboard similar to those in patient's transportation.
The following procedure will be used as recommended by the Local EMS provider (Johnson County):

1. Apply an appropriate, effective and properly fitted/sized cervical collar.
2. Position participant on the long spine board and center.
3. Place straps in an x-pattern over the shoulders and under the armpits to secure the upper chest.
4. Additional straps are placed across the iliac crest and above the knees to prevent movement.
5. Normal Anatomical Alignment of the spine should be maintained.
6. Immobilize the head in the normal anatomical position. 1-1.5 inches of non-compressive occipital padding may be used.
7. Towel rolls or other bulky, lightweight material may be placed around the head to stabilize.
8. Place a wide strip of adhesive tape across the forehead to form an "X" securing the head.
9. Secure the feet with tape to prevent leg motion.

The following cases will be considered:

i. Using traditional backboard.
ii. Using traditional backboard with cushions.

We will conduct a series of tests to collect information about your body's responses to the movement of the shaker table seat and to test whether or not we are tracking the markers attached to you. You will experience up to 200 bouts of typical ride vibration on the shaker table each lasting up to 60 seconds with total of up to 100 minutes. The test will be repeated for each of the above twoconditions.. The

"rides" will consist of vibration in one or multiple directions. Normally, up to 100 minutes (for each of the two above mentioned conditions) of that time will consist of exposure to typical "ride" vibration. If up to half of the tests need to be repeated, you could be exposed to up to 150 minutes of "ride" vibration.

In the event a test is stopped before all the data are collected or data are lost due to computer failure, the test will be repeated, up to a maximum of half of the possible tests. It is unlikely that more than one or two tests will actually require repetition, but all estimates of total daily vibration and shock exposure have included these additional tests. In the event data recording systems fail to acquire data during a test, the test will be repeated. This may take an additional six hours during a separate visit.

As mentioned above, it is possible that some tests may need to be further repeated in the event results are not stored properly (data lost due to computer error, etc.). The duration of the testing procedures should require no longer than 6 hours (with breaks). The expected total duration of exposure to the vibration is 100 minutes, but could be as high as 150 minutes in the event half of the tests require repeating.

During the tests, you will be asked by the investigators to rate your discomfort level either using verbal forms or paper based forms.

You may be asked to complete more visits if additional testing is required.

Audio/Video Recording or Photographs

One aspect of this study involves taking some pictures and video movies during the testing procedures. The motion capture cameras can only "see" infrared light reflected from markers. In addition to the motion capture camera images, we will take photographs and video of you using traditional still and video cameras to know where the markers are located on your body. The pictures and video movies will help us in identifying the location of the markers on the body during the experiments; otherwise, it would be very difficult to recognize the real markers' locations on the body by just looking to the motion capture data. In the event these materials are used in reports or publications, the images will be altered so that no personally-identifiable information will appear.

These recordings and photographs will be used to document the test protocol. These recordings will not be erased or destroyed as they will provide valuable documentation of the study.

WHAT ARE THE RISKS OF THIS STUDY?

You may experience one or more of the risks indicated below from being in this study. In addition to these, there may be other unknown risks, or risks that we did not anticipate, associated with being in this study.

You may feel some irritation from the preparation for, the use of, and the removal of the reflective markers, and accelerometers. We will try to minimize this risk by using only medical-grade tape meant for use on human skin and shaving any areas that have substantial hair. We will try to make the time that the devices are attached as short as possible consistent with the data to be gathered. We will monitor you

carefully by sight and by asking questions about how you feel. We will ask you if you are allergic to adhesive tape before placing the markers and accelerometers on your skin.

You may be at risk for developing dizziness. You will have a switch that will immediately stop the ride in the event you feel you need to stop. You can also take breaks as needed throughout the test protocol. We will monitor you carefully by sight and by asking questions about how you feel. If you are prone to motion sickness, have a history of vestibular (inner ear) problems, or do not tolerate simulation rides at Amusement Parks, you should not enroll in this study.

The vibration involved in this study may pose a risk for muscle or back pain with extended exposures. However, one day of testing is unlikely to result in any chronic vibration or shock injuries. The front to back vibrations you will experience should be no worse than those felt while riding a tractor on a rough field or operating typical heavy construction equipment for a period of time. We have analyzed the vibration for the conditions you will experience using international standards to be sure that the total exposure is within acceptable levels. If you have a history of neck or back pain, you should tell the researchers before enrolling in the study.

There is a risk that you could faint during the test. Sitting for extended periods of time, coupled with the simulated ride, could result in feeling like you could faint. Before fainting, people have reported experiencing weakness, lightheadedness, nausea, sweating, hyperventilation, blurred vision and/or impaired hearing. Sitting or lying down can reverse the symptoms. To minimize the risk of fainting, regular rest intervals are planned, where you will be asked to get up out of the seat and stand and move your arms and legs. Further you will be monitored closely for any signs of intolerance listed above, by sight and by asking questions about how you feel throughout the test. If you have any history of fainting or have a cardiac condition you should not enroll in this study.

If you have a history of neck or back pain, heart problems, neurological problems, balance problems or dizziness, motion sickness, or are taking over-the-counter drugs, prescribed drugs, or have consumed alcohol or recreational drugs within 24 hours of the study, you should not enroll in this study.

There is a risk that you may experience a fear of falling or being unable to maintain your balance in the seat. We will minimize this situation by monitoring you carefully by sight and by asking questions about how you feel. If you have any history of fear, then you should not enroll in this study.

WHAT ARE THE BENEFITS OF THIS STUDY?

You will not benefit from being in this study. However, we hope that, in the future, other people might benefit from this study because the result of this study may help seat and machine designers to develop more comfortable seats for heavy machinery operators.

WILL IT COST ME ANYTHING TO BE IN THIS STUDY?

You will not have any cost for being in this research study.

WILL I BE PAID FOR PARTICIPATING?

You will be paid for being in this research study. You will need to provide your social security number (SSN) in order for us to pay you. You may choose to participate without being paid if you do not wish to provide your social security number (SSN) for this purpose. You may also need to provide your address if a check will be mailed to you. If your social security number is obtained for payment purposes only, it will not be retained for research purposes.
You will be paid at a rate of $12 per hour of a total of up to $72. The average amount per visit is $48.

DO THE RESEARCHERS HAVE PERSONAL FINANCIAL INTEREST IN THIS STUDY?

No.

WHO IS FUNDING THIS STUDY?
Departmental Funding from the University of Iowa, Center for computer aided design.

WHAT IF I AM INJURED AS A RESULT OF THIS STUDY?

- If you are injured or become ill from taking part in this study, medical treatment is available at the University of Iowa Hospitals and Clinics.
- No compensation for treatment of research-related illness or injury is available from the University of Iowa unless it is proven to be the direct result of negligence by a University employee.
- If you experience a research-related illness or injury, you and/or your medical or hospital insurance carrier will be responsible for the cost of treatment.

WHAT ABOUT CONFIDENTIALITY?

We will keep your participation in this research study confidential to the extent permitted by law. However, it is possible that other people such as those indicated below may become aware of your participation in this study and may inspect and copy records pertaining to this research. Some of these records could contain information that personally identifies you.

- federal government regulatory agencies,
- auditing departments of the University of Iowa, and
- the University of Iowa Institutional Review Board (a committee that reviews and approves research studies)

To help protect your confidentiality, we will assign you an identification number that does not include any personally identifiable information. All data will be stored on password-protected computer files using this number and not your name. Your name and personal information will be linked to your study identification number in a separate document and kept by the principal investigator in electronic and hard-copy formats separately from the rest of the data. All data will be kept in a locked lab or office or

in password protected computer files, with appropriate backup. The motion data will be available to other researchers for future model development; however no personal identification of any kind will be linked to the data sets.

If we write a report or article about this study or share the study data set with others, we will do so in such a way that you cannot be directly identified.

IS BEING IN THIS STUDY VOLUNTARY?

Taking part in this research study is completely voluntary. You may choose not to take part at all. If you decide to be in this study, you may stop participating at any time. If you decide not to be in this study, or if you stop participating at any time, you won't be penalized or lose any benefits for which you otherwise qualify.

Will I Receive New Information About the Study while Participating?
If we obtain any new information during this study that might affect your willingness to continue participating in the study, we'll promptly provide you with that information.

Can Someone Else End my Participation in this Study?
Under certain circumstances, the researchers might decide to end your participation in this research study earlier than planned. This might happen because in our judgment it would not be safe for you to continue or because the funding for the research study has ended.

WHAT IF I HAVE QUESTIONS?

We encourage you to ask questions. If you have any questions about the research study itself, please contact: Salam Rahmatalla at (319) 335-5614 or salam-rahmatalla@uiowa.edu If you experience a research-related injury, please contact Salam Rahmatalla at (319) 335-5614 or salam-rahmatalla@uiowa.edu
If you have questions, concerns, or complaints about your rights as a research subject or about research related injury, please contact the Human Subjects Office, 105 Hardin Library for the Health Sciences, 600 Newton Road, University of Iowa, Iowa City, IA 52242-1098, (319) 335-6564, or e-mail irb@uiowa.edu. General information about being a research subject can be found by clicking "Info for Public" on the Human Subjects Office web site,http://research.uiowa.edu/hso. To offer input about your experiences as a research subject or to speak to someone other than the research staff, call the Human Subjects Office at the number above.

This Informed Consent Document is not a contract. It is a written explanation of what will happen during the study if you decide to participate. You are not waiving any legal rights by signing this Informed Consent Document. Your signature indicates that this research study has been explained to you, that your questions have been answered, and that you agree to take part in this study. You will receive a copy of this form.

FOR IRB USE ONLY
APPROVED BY: IRB-02
IRB ID #: 200811705
APPROVAL DATE: 08/06/11
EXPIRATION DATE: 08/05/12

Subject's Name (printed): _____

Do not sign this form if today's date is on or after **EXPIRATION DATE: 08/05/12** .

_____ _____
(Signature of Subject) (Date)

Statement of Person Who Obtained Consent

I have discussed the above points with the subject or, where appropriate, with the subject's legally authorized representative. It is my opinion that the subject understands the risks, benefits, and procedures involved with participation in this research study.

_____ _____
(Signature of Person who Obtained Consent) (Date)

REFERENCES

Allen, G. (1978). A critical look a biomechanical modeling in relation to specification for human tolerance of vibration and shock. AGARD Conference Proceedings No.253, Paris, France.

Amirouche, F. M. L. (1987a). "Biodynamic Analysis of the Human Body Subjected to Vibration." Engineering in Medicine and Biology Magazine, IEEE 6(3): 22-26.

Amirouche, F. M. L. (1987b). "Modeling of Human Reactions to Whole-Body Vibration." Journal of Biomechanical Engineering 109(3): 210-217.

Amirouche, F. M. L. and Ider, S. K. (1988). "Simulation and analysis of a biodynamic human model subjected to low accelerationsâ: A correlation study." Journal of Sound and Vibration 123(2): 281-292.

Amirouche, F. M. L., Xie, M, et al. (1994). "Optimization of the Contact Damping and Stiffness Coefficients to Minimize Human Body Vibration." Journal of Biomechanical Engineering 116(4): 413-420.

Bazrgari, B., Nussbaum, M. A., et al. (2010). "Soft tissue wobbling affects trunk dynamic response in sudden perturbations." Journal of Biomechanics 44(3): 574-551.

Bazrgari, B., A. Shirazi-Adl, et al. (2008a). "Computation of trunk muscle forces, spinal loads and stability in whole-body vibration." Journal of Sound and Vibration 318(4–5): 1334-1347.

Bazrgari, A. Shirazi-Adl, A, Kasra, M. (2008b). "Seated whole body vibrations with high-magnitude accelerations—relative roles of inertia and muscle forces." Journal of Biomechanics 41: 2639– 2646

Bernhard, M., A. Gries, et al. (2005). "Spinal cord injury (SCI)--prehospital management." Resuscitation 66: 13.

Berthoz, A, Mazoyer, B, Petit, L, Orssaud, C, Raynaud, L, Tzourio, N. (1992) “Bilateral parietal involvement in the execution of a sequence of memorized saccades in man.” Soc Neurosci Abstr 18:214.

Boileau, P. A. and Rakheja, S. (1998). "Whole-body vertical biodynamic response characteristics of the seated vehicle driver: Measurement and model development." International Journal of Industrial Ergonomics 22(6): 449-472.

Bouchut, J.-C., E. Van Lancker, et al. (2011). "Physical Stressors during Neonatal Transport: Helicopter Compared with Ground Ambulance." Air Medical Journal 30(3): 134-139.

Buck, B, Wolfel, H.A. (1998). “Dynamic three-dimensional finite element model of a sitting man with a detailed representation of the lumbar spine and muscles.” Computer Methods in Biomechanics and Biomedical Engineering. 2: 379-386.

Callafon, R. A. d. and Hof, P. M. J. V. d. (1996). "FREQID-Frequency domain identification toolbox for use with Matlab." Selected Topics in Identification, Modelling and Control 9.

Chapman.A.E, Baildon, R.W. (1983). "A new approach to the human muscle model." Journal of Biomechanics 16(10): 803-809.

Cho, Y. and Yoon, Y. S. (2001). "Biomechanical model of human on seat with backrest for evaluating ride quality." International Journal of Industrial Ergonomics 27(5): 331-345.

Cobb, S., T. Russo, et al. (2012). "Medical flight crew perceived work-related muscllоskeltal symtomps and related characteristics." Air Medical Journal 31(1): 6.

Coermann, R.R., (1962). "The mechanical impedance of the human on seat with backrest for evaluating ride quality." International Journal of Industrial Ergonomic 27, 331-345.

Courtney, A. and Cahn, A. (1999). "Ergonomics of grab unloaders for bulk materials handling." International Journal of Industrial Ergonomics 23(1-2): 6.

de Leva, P. (1996). "Adjustments to Zatsiorsky-Seluyanov's segment inertia parameters." Journal of Biomechanics 29(9): 1223-1230.

Dempster, W. T. and Gaughran, G. R. L. (1967). "Properties of body segments based on size and weight." American Journal of Anatomy 120(1): 33-54.

Denavit, J. and Hartenberg, R. S. (1955). "A kinematic notation for lower-pair mechanisms based on matrices." Trans. of the ASME. Journal of Applied Mechanics 22: 215-221.

DeShaw, J. and Rahmatalla, S. (2012). "Comprehensive Measurement in Whole-Body Vibration." Journal of Low Frequency Noise, Vibration and Active Control.31(2): 63-74.

DeVivo, M. J. (1997). "Causes and costs of spinal cord injury in the United States." Spinal Cord 35(12): 809-813.

Eger, T., J. Stevenson, et al. (2008). "Predictions of health risks associated with the operation of load-haul-dump mining vehicles: Part 2--Evaluation of operator driving postures and associated postural loading." International Journal of Industrial Ergonomics 38(9-10): 801-815.

Fard, M. A., T. Ishihara, et al. (2003a). "Dynamics of the Head-Neck Complex in Response to the Trunk Horizontal Vibration: Modeling and Identification." Journal of Biomechanical Engineering 125(4): 533-539.

Fard, M. A., T. Ishihara, et al. (2003b). "Transmission of the Translational Trunk Vibration to the Head-Neck Complex." JSME International Journal Series C Mechanical Systems, Machine Elements and Manufacturing 46(1): 116-122.

Fard, M. A., T. Ishihara, et al. (2004). "Identification of the head-neck complex in response to trunk horizontal vibration." Biological Cybernetics 90(6): 418-426.

Fritz, M. (1998). "Three-dimensional biomechanical model for simulating the response of the human body to vibration stress." Medical and Biological Engineering and Computing 36(6): 686-692.

Fritz, M. (2000a). "Description of the relation between the forces acting in the lumbar spine and whole-body vibrations by means of transfer functions." Clinical biomechanics (Bristol, Avon) 15(4): 234-240.

Fritz, M. (2000b). "Simulating the response of a standing operator to vibration stress by means of a biomechanical model." Journal of biomechanics 33(7): 795-802.

Griffin, M. J. (1978). "The evaluation of vehicle vibration and seats." Applied Ergonomics 9(1): 15-21.

Griffin, M. J. (1990). Handbook of human vibration. London, Academic Press.

Griffin, M. J. (2001). "The validation of biodynamic models." Clinical Biomechanics 16(1): S81-S92.

Harris, C. M. and Piersol, A. G. (2002). Harris' shock and vibration handbook. McGRAW Hill.

Hill, A. V. (1938). "The Heat of Shortening and Dynamic Constants of Muscle." Proc. R. Soc. B 126: 60.

Hill, A. V. (1953). "Chemical Change and Mechanical Response inStimulated Muscle." Proc. R. Soc. B 141(904):314-320.

Himmetoglu, S., M. Acar, et al. (2007). "A multi-body head-and-neck model for simulation of rear impact in cars." Proc. Inst. Mech. Eng. Part D-J. Automob. Eng. 221(5): 527-541.

Hinz, B., G. Menzel, et al. (2010). "Seat-to-head Transfer Function of Seated Men -- Determination with Single and Three Axis Excitations at Different Magnitudes." Industrial Health 48(5): 565-583.

Hinz, B., H. Seidel, et al. (2002). “Effects related to random whole-body vibration and posture on a suspended seat without backrest." Journal of Sound and Vibration 253(1): 265-282.

Huang, Y. and Griffin, M. J. (2008). "Nonlinear dual-axis biodynamic response of the semi-supine human body during longitudinal horizontal whole-body vibration." Journal of Sound and Vibration 312(1-2): 273-295.

Huang, Y. and Griffin, M. J. (2009). "Nonlinearity in apparent mass and transmissibility of the supine human body during vertical whole-body vibration." Journal of Sound and Vibration 324(1-2): 429-452.

Johanning, E., P. Landsbergis, et al. (2006). "Whole-body vibration and ergonomic study of US railroad locomotives." Journal of Sound and Vibration 298(3): 594-600.

Joshi, M. C. and RSharma, R. M. (2010). "Aero-medical Considerations in Casualty Air Evacuation (CASAEVAC)." Medical Journal Armed Forces India 66: 63-65.

Kitazaki, S. and Griffin, M. J. (1997). "A model analysis of whole-body viertical vibration, using a finite element model of the human body.” Journal of Sound and Vibration 200(1): 83-103.

Kittusamy, N. and Buchholz, B. (2004). "Whole-body vibrationand postural stress among operators fo construction equipment: A literature review." Journal of Safety Research 35(3): 255-261.

Kollar, I. (2001). "Frequency domain system identification toolbox-user's guide." Natick, MA, Mathworks.

Liang, C. C. and Chiang, C.F. (2006). "A study on biodynamic models of seated human subjects exposed to vertical vibration." International Journal of Industrial Ergonomics 36(10): 869-890.

Liang, C.C. and Chiang, C.F. (2008). "Modeling of a Seated Human Body Exposed to Vertical Vibrations in Various Automotive Postures." Industrial Health 46(2): 125-137.

Liu, J. Z., M. Kubo, et al. (1995). "A study on the difference of human sensation evaluation to whole body vibration in sitting and lying postures." Journal of Physiological Anthropology 14(5): 219-226.

Luo, Z. and Goldsmith, W. (1991). "Reaction of a human head neck torso system to shock." Journal of Biomechanics 24(7):499-510.

Madakashira-Pranesh, A. (2011). "Experimental and analytical study of transmission of whole body vibration to segments of the seated human body." PhD thesis, Concordia University.

Mandapuram, S., Rakheja, S., et al. (2011). "Analyses of biodynamic responses of seated occupants to uncorrelated fore-aft and vertical whole-body vibration." Journal of Sound and Vibration 330(16): 4064-4079.

Mansfield, N. J. and Griffin, M. J (2000). "Non-linearities in apparent mass and transmissibility during exposure to whole-body vertical vibration." Journal of biomechanics 33(8): 933-941.

Mansfield, N. J. and Maeda, S. (2005). "Effect of Backrest and Torso Twist on the Apparent Mass of the Seated Body Exposed to Vertical Vibration." Industrial Health 43(3): 413-420.

Marras, W. S. and Mirka, G. A. (1990). "Muscle activities during asymmetric trunk angular accelerations." Journal of Orthopaedic Research 8(6): 824-832.

Martin, T. E. (2003). "Clinical aspects of aeromedical transport." Current Anaestesia & Critical Care 14(2): 131-140.

Mathworks (2010). Optimization's ToolBox User's guide. Mathworks, Inc.

Muksian, R., and Nash, C. D. (1976). "On frequency-dependent damping coefficients in lumped-parameter models of human beings." Journal of Biomechanics 9:339-342.

Muksian, R., Nash, .D. (1974). "A model for the response of seated humans to sinusoidal displacements of the seat." Journal of Biomechanics 7: 209-215.

Nawayseh, N. and Griffin, M. J. (2005a). "Effect of seat surface angle on forces at the seat surface during whole-body vertical vibration." Journal of Sound and Vibration 284(3–5): 613-634.

Nawayseh, N. and Griffin, M. J. (2005b). "Non-linear dual-axis biodynamic response to fore-and-aft whole-body vibration." Journal of Sound and Vibration 282(3–5): 831-862.

Newland, D. E. (1984). An Introduction to random vibrations and spectral analysis,. New York, Longman Inc.

Nikolova, G. S. and Toshev, Y. E. (2007). "Estimation of male and female body segment parameters of the Bulgarian population using a 16-segmental mathematical model." Journal of Biomechanics 40(16): 3700-3707.

Nikooyan, A. A. and Zadpoor, A. A. (2011). "Mass-spring-damper modelling of the human body to study running and hopping--an overview." Proc Inst Mech Eng H 225(12): 11121-1135.

Paddan, G. and Griffin, M. J. (1988). "The transmission of translational seat vibration to the head:: Π. Horizontal vibration." J Biomech. **21**(3): 199-206

Paddan, G. S. and Griffin, M. J. (1988a). "The transmission of translational seat vibration to the head: Vertical seat vibration." Journal of Biomechanics 21(3): 191-197.

Paddan, G. S. and Griffin, M. J. (1998b). "A review of the transmission of translational seat vibration to the head." Journal of Sound and Vibration 215(4): 863-882.

Panjabi, M. M., Brand, R. A. Jr, et al. (1976). "Three-dimensional flexibility and stiffness properties of the human thoracic spine." Journal of biomechanics 9(4): 185-192.

Pankoke, S., Hofmann, J., et al. (2001). "Determination of vibration-related spinal loads by numerical simulation." Clinical biomechanics (Bristol, Avon) 16: S45-S56.

Patil, M. K., Palanichamy, M. S., et al. (1977). "Dynamic Response of Human Body Seated on a Tractor and Effectiveness of Suspension Systems." SAEpaper 770932: 755-792.

Patil, M. K., Palanichamy, M. S., et al. (1978). "Man-tractor system dynamics: Towards a better suspension system for human ride comfort." Journal of biomechanics 11(8–9): 397-406.

Peng, B., Y. Yang, et al. (2009). "Modeling and Simulation on the Vibration Comfort of Railway Sleeper Carriages." International Conference on Transportation Engineering, ASCE: 3766-3771.

Peng, G. C., Hain, T. C., et al. (1996). " A dynamical model for reflex activated head movements in the horizontal plane." Biological Cybernetics 75: 309-319.

Qassem, W. (1996). "Model prediction of vibration effects on human subject seated on various cushions." Medical engineering & physics 18(5): 350-358.

Qassem, W., Othman, M. O., et al. (1994). "The effects of vertical and horizontal vibrations on the human body." Medical Engineering & Physics 16(2): 151-161.

Rahmatalla, S. and DeShaw, J. (2011a). "Effective seat-to-head transmissibility in whole-body vibration: Effects of posture and arm position." Journal of Sound and Vibration 330(25): 6277-6286.

Rahmatalla, S. and DeShaw, J. (2011b). "Predictive discomfort of non-neutral head-neck postures in fore-aft whole body vibration." Ergonomics 54(3): 263-272.

Rahmatalla, S. and Liu Y. (2012). "An active head–neck model in whole-body vibration: Vibration magnitude and softening." Journal of biomechanics 45(6):925-930.

Rahmatalla, S., Smith, R., et al. (2010). "A Quasi-static Discomfort Measure in Whole-body Vibration." Industrial Health 48(5): 645-653.

Rehn, B., T. Nilsson, et al. (2005). "Whole-Body Vibration Exposure and Non-neutral Neck Postures During Occupational Use of All-terrain Vehicles." Annals of Occupational Hygiene 49(3): 267-275.

Robertson, C. D. and Griffin, M. J. (1989). “Laboratory studies of the electromyographic response to whole-body vibration. Technical Report ISVR 184”. University of Southampton, Southampton, UK.

Schoukens, J. and Pintelon, R. (1990). " Measurement of frequency response functions in noisy environments." Instrumentation and Measurement, IEEE Transactions on 39(6): 905-909.

Seidel, H. and Griffin, M. J. (2001). "Modelling the response of the spinal system to whole-body vibration and repeated shock." Clinical biomechanics (Bristol, Avon) 16: S3-S7.

Sekhon, L. H. S. and Fehlings, M. G. (2001). "Epidemiology, demographics, and pathophysiology of acute spinal cord injury." Spine 26(S2).

Smith, S. D. (2000). "The effects of head orientation on head/helmet vibration response." SAFE Journal 30(1):114-125.

Standardization, (1998). Mechanical vibration and shock—guidance on safety aspects of tests and experiments with people. part 1: exposure to whole-body mechanical vibration and repeated shock, ISO 13090-1:1998.

Standardization, (2004). Mechanical vibration and shock—evaluation of human exposure to whole body vibration. part 5: method for evaluation of vibration containing multiple shocks, ISO 2631-5:2004.

Standardization, (2010). Mechanical vibration and shock—evaluation of human exposure to whole body vibration. part 1: general requirements, ISO 2631-1:2010.

Suggs, C. W., Abrams, C. F., et al. (1969). "Application of a Damped Spring-Mass Human Vibration Simulator in Vibration Testing of Vehicle Seats." Ergonomics 12(1): 79-90.

Thuresson, M., Ang, B., et al. (2005). "Mechanical load and EMG activity in the neck induced by different head-worn equipment and neck postures." International Journal of Industrial Ergonomics 35(1): 13-18.

Thurman, D., Burnett, C., et al. (1994). "Surveillance of spinal cord injuries in Utah, USA." Spinal Cord 32: 665-669.

Vogel, H., Kohlhaas, R., et al. (1982). "Dependence of motion sickness in automobiles on the direction of linear acceleration." European Journal of Applied Physiology and Occupational Physiology 48(3): 399-405.

Vogt, L. H., Krause, H. E., et al. (1973). “Mechanical Impedance of Supine Humans under Sustained Acceleration”.Aerosp. Med 44(2):123-128.

Vogt, L. H., Mertens, H., et al. (1978). "Model of the supine human body and its reactions to external forces " Aviation, Space, and Environmental Medicine 49(2): 270-278.

Wan, Y. and Schimmels, J. M. (1995). “A Simple Model that captures the essential dynamics of seated human exposed to whole body vibration”. Advances in Bioengineering, ASME. 31: 333-334.

Wang, W., Bazrgari, B., et al. (2010). "Biodynamic response and spinal load estimation of seated body in vibration using finite element modeling." Industrial Health 448(5): 557-566.

Wang, W., Rakheja, S., et al. (2006). "The role of seat geometry and posture on the mechanical energy absorption characteristics of seated occupants under vertical vibration." International Journal of Industrial Ergonomics 36(2): 171-184.

Wei, L. and Griffin, M. J. (1998). "Mathematical models for the apparent mass of the seated human body exposed to vertical vibration.” Journal of Sound and Vibration 212(5): 855-874.

Winter, D. A. (1979). Biomechanics of human movement. New York: Wiley.

Winter, D. A. (2005). "Biomechanics and motor control of human movement."

Yoganandan, N., Kumaresan, S., et al. (1997). "Finite Element Model of the Human Lower Cervical Spine: Parametric Analysis of the C4-C6 Unit." Journal of Biomechanical Engineering 119(1): 87-92.

Yue., Z. and Mester, J. (2002). "A model analysis of internal loads, energetics, and effects of wobbling mass duringthe whole-body vibration." Journal of Biomechanics 35: 639-650.

Zadpoor, A. A. and Nikooyan, A. A. (2010). "Modeling muscle activity to study the effects of footwear on the impact forces and vibrations of the human body during running." Journal of Biomechanics 43(2): 186-193.

Zheng, G., Qiu, Y., et al. (2011). "An analytical model of the in-line and cross-axis apparent mass of the seated human body exposed to vertical vibration with and without a backrest." Journal of Sound and Vibration 330(26): 5609-6525.